

## Characterizing Atmospheric Escape from Mars Today and Through Time, with MAVEN

R.J. Lillis<sup>1</sup> · D.A. Brain<sup>2</sup> · S.W. Bougher<sup>3</sup> · F. Leblanc<sup>4</sup> · J.G. Luhmann<sup>1</sup> · B.M. Jakosky<sup>2</sup> · R. Modolo<sup>4</sup> · J. Fox<sup>5</sup> · J. Deighan<sup>2</sup> · X. Fang<sup>2</sup> · Y.C. Wang<sup>1</sup> · Y. Lee<sup>3</sup> · C. Dong<sup>2</sup> · Y. Ma<sup>6</sup> · T. Cravens<sup>7</sup> · L. Andersson<sup>2</sup> · S.M. Curry<sup>1</sup> · N. Schneider<sup>2</sup> · M. Combi<sup>3</sup> · I. Stewart<sup>2</sup> · J. Clarke<sup>8</sup> · J. Grebowsky<sup>9</sup> · D.L. Mitchell<sup>1</sup> · R. Yelle<sup>10</sup> · A.F. Nagy<sup>3</sup> · D. Baker<sup>2</sup> · R.P. Lin<sup>1</sup>

Received: 4 February 2014 / Accepted: 15 May 2015  
© Springer Science+Business Media Dordrecht 2015

**Abstract** Two of the primary goals of the MAVEN mission are to determine how the rate of escape of Martian atmospheric gas to space at the current epoch depends upon solar influences and planetary parameters and to estimate the total mass of atmosphere lost to space over the history of the planet. Along with MAVEN's suite of nine science instruments, a collection of complementary models of the neutral and plasma environments of Mars' upper atmosphere and near-space environment are an indispensable part of the MAVEN toolkit, for three primary reasons. First, escaping neutrals will not be directly measured by MAVEN and so neutral escape rates must be derived, via models, from in situ measurements of plasma temperatures and neutral and plasma densities and by remote measurements of the extended exosphere. Second, although escaping ions will be directly measured, all MAVEN measurements are limited in spatial coverage, so global models are needed for intelligent interpolation over spherical surfaces to calculate global escape rates. Third, MAVEN measurements will lead to multidimensional parameterizations of global escape rates for a range of solar

---

✉ R.J. Lillis  
[rlillis@SSL.Berkeley.edu](mailto:rlillis@SSL.Berkeley.edu)

<sup>1</sup> Space Sciences Laboratory, University of California Berkeley, 7 Gauss Way, Berkeley, CA 94720, USA

<sup>2</sup> Laboratory for Atmospheric and Space Physics, University of Colorado, 3665 Discovery Drive, Boulder, CO 80309, USA

<sup>3</sup> Department of Atmospheric, Oceanic and Space Sciences, University of Michigan, Ann Arbor, MI, USA

<sup>4</sup> Laboratoire de Météorologie Dynamique, Jussieu, Paris, France

<sup>5</sup> Department of Physics, Wright State University, Dayton, OH 45435, USA

<sup>6</sup> Institute of Geophysics and Planetary Physics, University of California Los Angeles, Los Angeles, CA, USA

<sup>7</sup> Department of Physics and Astronomy, University of Kansas, Lawrence, KS, USA

<sup>8</sup> Astronomy Department, Boston University, Boston, MA, USA

<sup>9</sup> NASA Goddard Space Flight Ctr., Greenbelt, MD, USA

<sup>10</sup> Lunar and Planetary Laboratory, University of Arizona, Tucson, AZ, USA

and planetary parameters, but further global models informed by MAVEN data will be required to extend these parameterizations to the more extreme conditions that likely prevailed in the early solar system, which is essential for determining total integrated atmospheric loss. We describe these modeling tools and the strategies for using them in concert with MAVEN measurements to greater constrain the history of atmospheric loss on Mars.

**Keywords** Mars · Atmosphere · Escape · Maven · Models

## 1 Introduction

The Mars Atmosphere and Volatile Evolution (MAVEN) mission is a NASA Mars Scout mission, selected primarily to determine the importance of the role of escape of volatiles to space on the planet's climatic evolution, i.e. its transition from an environment with sufficient atmospheric pressure and temperatures that liquid water was at least episodically stable, to the low-pressure, cold, arid climate of today. The three primary scientific goals of MAVEN are to (1) determine the structure, composition and dynamics of the Martian upper atmosphere, (2) determine rates of atmospheric escape through various processes at the current epoch and with these answers, (3) determine the integrated loss to space that has occurred through Martian history.

Reviews of the MAVEN mission (Jakosky et al. 2015, [this issue](#)), and the complement of nine instruments may be found in the companion papers of the current special issue. Also in this issue, Bougher et al. (2014) focus on MAVEN science goal 1, providing a review of the current state of knowledge of Mars aeronomy (i.e. its upper atmosphere and near-space environment) and examining the ways in which it will be improved through the measurements MAVEN will make.

Here we will focus primarily on MAVEN science goal 2, i.e. how MAVEN data will be used to characterize neutral and ion escape rates from the Martian atmosphere at the current epoch and how they vary spatially, with solar and heliospheric influences (e.g. solar EUV, solar wind pressure) as well as planetary parameters (e.g. season, subsolar longitude). We also will examine, in somewhat less detail, MAVEN Science goal 3. In other words, with knowledge of how the controlling factors govern atmospheric loss processes today, how much total atmosphere Mars may have been lost since the earliest epochs of the solar system and how this will inform our view of Mars' climate evolution.

Mars atmospheric escape (and the history thereof) is a challenging problem to investigate, with multiple interconnected physical processes, nonlinear relationships with internal and external drivers and spatially and temporally inhomogeneous patterns of escape. Despite the tightly focused suite of integrated investigations onboard the MAVEN spacecraft, in situ coverage is limited to single points in time and space along MAVEN's precessing orbit, while remote-sensing data has greater coverage but requires more inversion and is not nearly as comprehensive in terms of derived quantities. Also, it is important to note that only escaping ions are directly measured. Neutral escape rates must be inferred from model calculations making use of MAVEN in-situ measurements of neutral densities and plasma densities and temperatures, through coronal scale heights and by measurements of processes known to produce energetic atoms. Lastly, MAVEN will likely not be fortunate enough to make escape measurements over the entire range of solar conditions thought to have been prevalent over solar system history.

In order to bridge these measurement 'gaps' (spatial, temporal and with respect to solar inputs and upper atmospheric processes and quantities), it is imperative to closely integrate

several types of physics-based models with multi-instrument analysis of MAVEN data. This paper will discuss the strategy for determining, to the best of our ability using data and models, rates of neutral and ion escape from the Martian atmosphere, how they are connected, how they vary with solar inputs and how they may have changed over the history of our solar system. Section 2 provides a brief overview of the Mars upper atmosphere and its interaction with the solar wind. Section 3 discusses the factors, both external (e.g. solar wind pressure) and internal (e.g. dust activity, subsolar longitude) that are expected to control atmospheric escape. Section 4 discusses the global thermosphere, ionosphere, exosphere and magnetosphere models that will be available, as well as the coupling between these models and the sets of parameters with which the models will be run to build a model ‘library’ that may be utilized for physical interpretation as well as interpolation between measurements. Section 5 discusses in detail the strategy for characterizing the ‘ground state’ and variability of each of the 6 primary escape processes, in terms of the necessary measurements, models, parameterizations and interpolation/extrapolation methods that will be used, including corrections for double counting and feedback among escape processes. Section 6 discusses a strategy for using the aforementioned knowledge, along with reasonable guesses for the evolution of solar drivers, to extrapolate back in time and hence estimate the total atmospheric loss over Martian history. Section 7 summarizes the paper and discusses some of the broad science questions expected to be answered and generated by the MAVEN mission.

Unlike many planetary orbiter or flyby missions with typically diverse sets of science goals and associated instrumentation, MAVEN is true to the NASA Mars Scout concept in that it is focused on understanding an as-yet insufficiently explored aspect of the Martian system: the structure and dynamics of the upper atmosphere and how escape of gases depends on solar and planetary drivers, both now and in the past. This paper discusses the integrated strategy necessary to achieve this understanding.

## 2 The Mars Upper Atmosphere and Its Interaction with the Solar Wind

The bulk atmosphere of Mars is primarily CO<sub>2</sub>, with small amounts of Ar, O<sub>2</sub>, O, N<sub>2</sub> and CO (Nier and McElroy 1977) and several other trace species (Fox and Hać 2009; Smith et al. 2014). The thermosphere is the collisional part of the upper atmosphere and is bounded below by the homopause (115–130 km altitude), above which turbulent mixing is weak enough that the constituent species have separate scale heights (Izakov and Krasicki 1977; Leovy 1982) and above by the exobase (160–200 km altitude), above which an escaping particle moving radially will undergo one collision on average (Vaille et al. 2009b). Thermospheric structure and dynamics are controlled primarily by solar UV and EUV heating, radiative and collisional cooling, gravity and planetary waves, thermal tides, dust activity and IR heating in the lower atmosphere, and charged particle precipitation (Bougher et al. 2014).

The region above the exobase, where neutral particles collide rarely and hence move mostly ballistically, is called the exosphere and is dominated by atomic hydrogen and oxygen, with trace amounts of helium and carbon. Embedded in the upper atmosphere is the Martian ionosphere, whose ion component is primarily O<sub>2</sub><sup>+</sup>. Here, CO<sub>2</sub><sup>+</sup>, the primary photoionization product, quickly reacts with neutral O to produce O<sub>2</sub><sup>+</sup>. The O<sub>2</sub><sup>+</sup> peak density occurs where the EUV optical depth of CO<sub>2</sub> is unity (~ 120–130 km at the subsolar point). O<sub>2</sub><sup>+</sup> dissociatively recombines with thermal electrons, producing hot O atoms that populate the exosphere. Bougher et al. (2014) provides a more detailed review of the upper atmosphere and ionosphere as a reservoir for atmospheric escape.

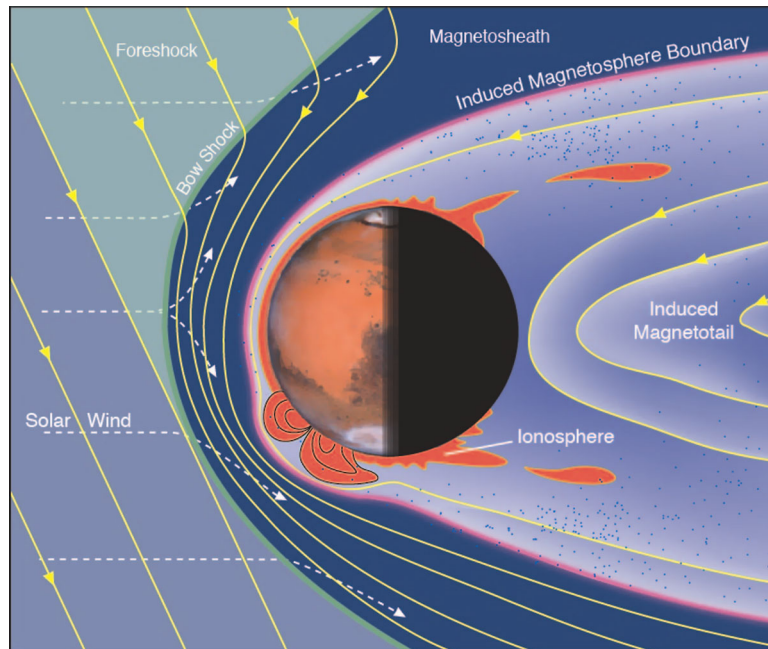


**Fig. 1** Illustration of the global plasma interaction between Mars and the solar wind. Various plasma boundaries and regions are described in Sect. 2. Image courtesy of S. Bartlett

Though the collisional region of the Mars upper atmosphere (below  $\sim 200$  km) is not directly exposed to the solar wind, the upper reaches of the atmosphere are unprotected by the kind of global scale magnetic fields present at Earth and the giant planets. The extended dayside ionosphere forms a conducting obstacle to the solar wind, which must slow down when it encounters the obstacle. The transition from supersonic to subsonic solar wind flow produces a bow shock and magnetosheath of shocked, turbulent solar wind plasma behind it. The interplanetary magnetic field (IMF), moving with the solar wind, induces currents in the upper ionosphere via Faraday's law. These currents generate magnetic fields approximately tangential to the surface, giving the global magnetic field configuration a 'piled-up and draped' character inside the magnetosheath, causing plasma to divert around the planet, as shown in Fig. 1. An induced magnetotail forms behind the planet with approximately sunward and anti-sunward-directed magnetic tail lobes. This situation is most similar to that found at Venus, also unmagnetized and with a substantial atmosphere. Crustal remanent magnetic fields (spatially inhomogeneous and strongest in  $\sim 1/3$  of the southern hemisphere between  $120$  and  $240^\circ$  east longitude) rotate with the planet and modify the global Venus-like interaction, standing off the solar wind to distances of up to  $1000$  km (Brain et al. 2003). The crustal fields and specifically the topology thereof, result in an inhomogeneous pattern of electron precipitation, particularly on the nightside, where the resulting ionosphere is patchy and highly irregular.

Mars' is a uniquely rich electrodynamic environment in which atmospheric escape occurs. The interplay between solar wind structures (e.g. sector boundaries, corotating interaction regions, coronal mass ejections, stream instabilities etc.), the induced magnetosphere and the rotating crustal fields, as well as energetic particle precipitation and solar EUV variability, result in a wide array of interconnected plasma processes which can drive at-

mospheric escape. MAVEN will not only determine atmospheric escape rates (the focus of this paper) but also elucidate this complex pattern of plasma processes so that we may gain a deeper understanding of the Martian-solar wind interaction as a whole.

### 3 The Drivers Controlling Atmospheric Escape

Several factors are thought to control rates of atmospheric escape from Mars. One of the principal goals of the MAVEN mission is to characterize the sensitivity of the different escape channels to these controlling factors. This is important both for the sake of characterizing the Martian upper atmospheric and near-space environment today and also to allow a confident extrapolation of these escape processes to conditions that existed over the last 4.5 Gyr. Some factors, such as solar wind pressure, MAVEN will hopefully sample over a range representative of that seen by Mars over solar system history. Others, such as planetary obliquity, will remain effectively fixed during the MAVEN mission despite having varied substantially over that same history.

These factors fall into 2 broad categories: solar and planetary. Our ability to accurately determine some of these factors will vary throughout the mission and will depend on the evolution of the MAVEN orbit and data from other spacecraft orbiting Mars. We will now discuss these controlling factors (listed in Table 1: Factors affecting atmospheric escape, the data that will be used to constrain those factors and relevant restrictions.) and MAVEN's ability to measure them over ranges representative of Mars history.

#### 3.1 Solar and Heliospheric Factors

##### 3.1.1 Solar EUV Flux

Solar extreme ultraviolet radiation originates in the hot solar atmosphere and has two main impacts that control atmospheric escape at Mars: heating and photoionization. It heats the Martian upper atmosphere, determining temperatures in the thermosphere and thermal exosphere, driving thermospheric winds and determining the location of the nominal exobase (Bougher et al. 1990). It ionizes neutrals, determining pickup ion loss rates in the exosphere, e.g. Luhmann and Brace (1991), sputtering rates from reimpacting pickup ions (Leblanc and Johnson 2001; Luhmann et al. 1992), photochemical loss rates from dissociative recombination in the thermosphere (e.g. Fox and Hać 2009; Valeille et al. 2009b) and lastly gross ionospheric structure (e.g. peak densities) and current systems, both of which are factors in ion outflow and bulk ion loss. Further, Mars Express observations have shown that solar flare activity can result in significant increases in ion escape fluxes from Mars (Futaana et al. 2008).

Solar EUV flux will be measured by the MAVEN EUV instrument (Eparvier et al. 2014) in the following bands: 0.1–7 nm, 17–22 nm and the 121.6 nm Lyman alpha line. Its measurements are continuous while MAVEN is in sunlight (eclipses vary from 0 to 75 minutes, averaging 34 minutes per 4.5 hour orbit). Several other spacecraft in the inner solar system (STEREO-A, STEREO-B, SDO, TIMED) ensure that it is unlikely a large flare will be missed, even when MAVEN is in shadow.

Solar EUV flux varies with the 11-year solar cycle, with the 27-day solar rotation period as solar active regions move in and out of view of Mars, and over timescales of minutes to hours when a solar flare occurs. In addition, the EUV flux seen at Mars varies over the Martian year by a factor of  $\sim 1.43$  as Mars' eccentric orbit ( $e = 0.093$ ) brings it 1.38 AU to 1.67 AU from the sun. The range of EUV fluxes observed by MAVEN during its prime

**Table 1** Factors affecting atmospheric escape, the data that will be used to constrain those factors and relevant restrictions

Solar & heliospheric factors	Atmospheric escape dependence	Data used to constrain	Restrictions
Solar EUV flux	Heats neutrals. Also, ionization of neutrals allows escape via solar wind pickup, sputtering and dissociative recombination	MAVEN EUV (SWEA photoelectron density as a backup)	Unavailable in shadow. Will not reach high early solar system values
Solar wind pressure	Determines plasma boundary locations, hence fraction of exosphere available for pickup ion loss and sputtering	MAVEN SWEA	Undisturbed SW will not be sampled for ~ 20 % of the primary mission
IMF direction and intensity	Determines global magnetic geometry and topology, hence: (1) pattern of impacting pickup ions for sputtering, (2) sizes/locations of escape channels for energized ions	MAVEN MAG	Undisturbed IMF will not be sampled for ~ 20 % of the primary mission
Solar energetic particle (SEP) flux	SEPs heat and ionize the atmosphere, allowing for greater escape	MAVEN SEP	Coarse angular resolution of SEP instrument
<b>Planetary factors</b>			
Subsolar longitude (i.e. Mars rotation phase) & subsolar latitude (determined by season and obliquity)	Longitude of the crustal fields w.r.t. the solar wind alters global plasma interaction	JPL ephemerides	Current obliquity = 25°. Average obliquity over solar history = 38°. Also, crustal field pattern may have been different on early Mars
Heliocentric distance and eccentricity	Due to inverse square law, distance from the sun affects solar wind pressure and EUV flux	JPL ephemerides	Current eccentricity = 0.09. Average eccentricity = 0.07
Dust activity	Dust storms heat the lower atmosphere, increasing scale heights and neutral winds in the thermosphere	IUVS apoapse scans of dust opacity, MRO MARCI daily weather reports. MRO MCS & Odyssey Themis dust profiles	

mission should be a factor of  $\sim 2$ . Thus MAVEN measurements will enable understanding of how atmospheric escape rates vary with EUV at the present epoch. Then, with the help of models (themselves informed/improved by MAVEN measurements of escape), we can extrapolate escape rates over the full range of EUV likely to have prevailed over solar system history (a factor of  $\sim 6$  (Zahnle and Walker 1982)).

### 3.1.2 Solar Wind Pressure

Solar wind (SW) pressure affects atmospheric escape rates in 3 interconnected ways. First, exospheric neutrals are ionized through charge exchanging with solar wind pro-

tons, picked up by the solar wind convection electric field and either lost to space or cause sputtering when they precipitate into the atmosphere (Nagy et al. 2004). Second, solar wind pressure determines the locations and shapes of the important plasma boundaries in the Mars-solar wind interaction: the bow shock, magnetic pileup boundary (MPB, inside of which SW protons do not easily penetrate) (Connerney et al. 2000; Verigin et al. 1993) and photoelectron boundary (Mitchell et al. 2001). Higher pressures move these boundaries closer to the planet, leaving a larger fraction of the exosphere exposed to solar wind pickup. Third, higher solar wind pressures compress the crustal magnetic fields, altering the sizes and locations of regions of open magnetic field lines (Lillis and Brain 2013), along which electrons can precipitate (i.e. the primary source of ionization on the nightside) and ion outflow can occur.

SW pressure at Mars typically varies on timescales of days as faster and slower regions of solar wind move past Mars and on timescales of hours if solar wind disturbances such as interplanetary coronal mass ejections (ICMEs) or corotating interaction regions (CIRs) are propagating past.

The Solar Wind Ion Analyzer (SWIA) (Halekas et al. 2013) and Solar Wind Electron Analyzer (SWEA) (Mitchell et al. 2014) will measure SW pressure directly when MAVEN is in the solar wind by measuring the density and velocity of the flowing solar wind. The precession of the MAVEN orbit allows for sampling of the undisturbed SW at least once per orbit during  $\sim 85\%$  of the primary mission. During other times, proxies may be used, such as magnetic field magnitude from MAG in the magnetic pileup region (e.g. Crider et al. 2003). Complementary measurements of SW pressure from the Ion Mass Analyzer (IMA) and Electron Spectrometer (ELS) (Barabash et al. 2007b) on the Mars Express spacecraft (which spends 80% of its time in the solar wind, encountering it on every orbit) will be very useful in this regard.

On the declining phase of the solar cycle, typically a wide range of solar wind speeds and densities is observed (Gosling et al. 1995). Thus it is expected that MAVEN will measure atmospheric escape rates over a range of solar wind pressures as was observed by Mars global surveyor (Brain 2006; Crider et al. 2003), from quiet conditions (say 0.25 to 1.5 nPa) to the kinds of very active conditions (say, over 10 nPa) that were likely more common in the early solar system (Newkirk et al. 1981).

### 3.1.3 IMF Direction and Intensity

The orientation and intensity of the interplanetary magnetic field (IMF) affects atmospheric escape rates in two primary ways. First, as the solar wind in which it is embedded mass-loads and slows down, the resulting global pattern of piled-up, draped magnetic field (as the field lines are dragged through the Mars ionosphere) determines the Lorentz motion of pickup ions created in the exosphere (Fang et al. 2010; Curry et al. 2013b); some of these ions escape the planet and some impact the atmosphere, causing sputtering escape. Second, the IMF affects magnetic topology in near-Mars space; as the planet rotates, the crustal remanent magnetic fields connect and re-connect with the draped IMF to create a dynamic pattern of open and closed field lines in near-Mars space (which allow and retard precipitation of solar wind electrons and outflow of planetary ions respectively). In other words, IMF conditions affect the conduits in the upper atmosphere through which (a) energy is deposited and (b) ion escape occurs, as has been studied using observations from Mars Express (Lundin et al. 2011; Nilsson et al. 2006)

The IMF at Mars varies on timescales of days (as solar wind sector boundaries move past the planet), hours (during the passage of solar wind disturbances such as coronal mass ejections e.g. Webb 2000) and minutes (e.g. solar wind turbulence Bruno and Carbone 2013).

MAVEN should observe long IMF ‘quiet’ periods when the ‘ground state’ of the Mars-SW interaction can be characterized, as well as more disturbed conditions when a more dynamic interaction occurs.

As mentioned in the previous subsection, MAVEN will spend at least part of its  $\sim$  4.5 hour orbit in the undisturbed solar wind for most of the primary mission, allowing the IMF to be measured directly by the two magnetometers located on small ‘diving boards’ at the end of each solar panel (Connerney et al. 2015). When the orbit does not permit direct sampling, well-calibrated IMF proxies such as the direction of the dayside draped magnetic field away from crustal field regions (Brain et al. 2006) can be used instead.

### 3.1.4 Solar Energetic Particle Flux

Solar energetic particles (SEPs) precipitating into the Martian atmosphere are expected to have a substantial impact on rates of escape. SEP ions of up to  $\sim$  200 keV deposit their energy above the homopause (Leblanc et al. 2002) and can therefore have a substantial effect on the thermosphere, i.e. the main reservoir from which escape occurs. Calculations (Leblanc et al. 2002) suggest large SEP events deposit energy in the upper atmosphere that can rival or exceed that deposited by solar EUV, at least in some altitude ranges. Fluxes of escaping planetary ions in the magnetotail have been shown to increase by an order of magnitude during SEP events (Futaana et al. 2008). SEPs have also been shown to cause substantial ionization (Espley et al. 2006; Lillis et al. 2012; Morgan et al. 2006; Nemeč et al. 2014) and are expected to cause neutral heating (Leblanc and Johnson 2002) and changes in chemistry (e.g. Sheel et al. 2012).

At present, SEPs have typically very low fluxes as the high-energy ‘superhalo’ component of the solar wind. Their fluxes can increase by several orders of magnitude within tens of minutes to a few hours (Tylka 2001; Delory et al. 2012), before decreasing to background level over a period of hours to (up to) several days during times of intense solar and heliospheric activity. They are accelerated at the sun as well at interplanetary shock fronts as those fronts expand out into the heliosphere. Because they are much faster than the solar wind, they do not travel radially from the sun but along the heliospheric Parker spiral magnetic field from their source region, whose angle to the Mars-sun line is typically 56 degrees at Mars. SEP events are thought to have been more intense and more frequent in the early solar system (Walker 1975) and as such it is imperative to understand the response of Mars atmospheric escape rates to such events.

Spectra of SEP protons and electrons will be measured in 4 orthogonal look directions by the SEP instrument, located on the main spacecraft deck (Larson et al. 2015, [this issue](#)).

## 3.2 Planetary Factors

### 3.2.1 Planetary Subsolar Location

The planetary latitude and longitude of Mars’ subsolar point also affect atmospheric escape rates. This is because the crustal magnetic fields, with their sources in ferromagnetic minerals within the crust (e.g. Dunlop and Arkani-Hamed 2005), are inhomogeneously distributed and are fixed to the planet, continuously changing their orientation with respect to the solar wind and piled-up, draped IMF. Two major timescales are relevant here: diurnal and seasonal. The crustal fields rotate with the planet every Martian sol (24 hours, 37 minutes) and, due to Mars’ 25.2° obliquity, ‘nod’ up and down with a total amplitude of 50.4° over the Martian year. This orientation affects the location of the bow shock and magnetic pileup

boundary (Verigin et al. 1993) (therefore affecting patterns/trajectories of escaping and impacting pickup ions), as well as the global pattern of open versus closed magnetic field lines which in turn determine the patterns of ion outflow and electron impact ionization.

With no resonances between the slowly-precessing MAVEN orbit period and Martian rotation period, MAVEN will sample all subsolar longitudes. In addition, over the course of the prime mission the subsolar latitude will span its entire range from  $-25.2$  to  $+25.2^\circ$  (southern summer to northern summer), providing the full range of relative orientations between the crustal fields and IMF for characterizing escape rates at the present epoch.

An unavoidable shortcoming for extrapolating escape rates back in time is that Mars' obliquity has, due to gravitational perturbations primarily from Jupiter, likely ranged from  $0^\circ$  to  $82^\circ$  over solar system history with a mean of  $\sim 38^\circ$  (Laskar et al. 2004). Nonetheless, global models of escape, having been improved/informed by MAVEN data over the accessible range, will allow us to extrapolate to larger subsolar latitudes and enable a calculation of integrated escape over solar system history.

### 3.2.2 Dust Activity

Suspended dust in the Martian lower atmosphere (up to 60 km) absorbs solar infrared radiation and heats the surrounding gases, thereby increasing neutral temperatures (and hence scale heights). Dust activity (as measured by dust opacity) thus causes the entire atmosphere to expand, including the thermal component of the exosphere (e.g. Bougher et al. 1999; Smith 2002). Since the exosphere is the source for pickup ions, both pickup ion escape and sputtering escape rates will depend on dust activity.

Martian dust opacity on a global scale will be measured as part of the apoapsis disk maps made by the MAVEN Imaging Ultraviolet Spectrograph (IUVS) (McClintock et al. 2014). Dust opacity measurements and profiles are made daily by the Mars Climate Sounder (MCS) (Heavens et al. 2011; McCleese et al. 2007) on the Mars Reconnaissance Orbiter (MRO) spacecraft and the Thermal Emission Imaging System (ThEmIS) (Christensen et al. 2004) on Mars Odyssey, while day-by-day weather reports (including dust storm activity) are provided by the MRO Mars Color Imager (MarCI) camera. As of writing, all three instruments are healthy and are expected to provide this important input for MAVEN to determine the effect of dust on atmospheric escape rates.

## 4 The Role of Global Models in Constraining Mars Atmospheric Escape

### 4.1 Global Models of the Mars Upper Atmosphere and Near-Space Environment

As mentioned earlier, the upper atmosphere and near space environment of Mars is a vastly complex system involving a wide variety of physical processes and a wide range (many orders of magnitude) of particle densities. Computer simulations can improve understanding of such complex systems by helping to constrain which process or processes, and to what relative degree, may be responsible for features observed in measurements of the system, as well as providing a representation of aspects or regions of the system that may be inaccessible to measurements. While 1-dimensional representations (with altitude as the spatial dimension) of the upper atmosphere system have been useful in elucidating some of the physics (atomic processes and particle transport are the broadest categories), most if not all characteristics of the system are not only spherically asymmetric but display strong horizontal gradients and flows. Therefore the system cannot be understood without considering it

as a heterogeneous 3-dimensional spherical shell around the planet, extending out to several Martian radii.

Over the last 2 decades (with heritage going back even further), a suite of models have been developed to simulate subsets of this global system. Since no single model can accurately represent the motions of charged and neutral particles over 10 or more orders of magnitude in density, multiple separate models must be coupled together, as will be discussed in this section.

First, from the ground to just above the exobase, so-called global circulation models (GCMs) simulate the atmosphere (including the thermosphere and ionosphere) in the fluid regime as it responds to topography, planetary rotation and solar heating and ionization. Second, so-called Direct Simulation Monte Carlo (DSMC) models simulate the neutral atmosphere with macro-particles from a few scale heights below the exobase out to several Mars radii in order to capture the physics of the transition from the collisional regime (where fluid treatments are valid) to the collisionless regime (where kinetic treatments are required). DSMC models take inputs from GCMs near their lower boundary and are not time-dependent. Last, global plasma models, as their name suggests, simulate the plasma physics of the interaction between the solar wind and the Martian ionosphere and exosphere, using either a magnetohydrodynamic (MHD) fluid approach or a so-called hybrid approach where ions are treated kinetically and electrons are simulated as a massless charge-balancing fluid. Global plasma models take exospheric inputs from DSMC models and thermospheric inputs from GCMs. These one-way couplings represent the current state-of-the-art; the models are not currently capable of simulating feedbacks between the space environment and ionosphere/thermosphere, although 2-way coupling is planned in the near future.

For each of these three types of models there exist several active modeling efforts as of the time of writing, from just three for the DSMC models to at least eight for the global plasma models (Brain et al. 2010a). For reasons of simplicity and because the MAVEN team membership is limited in number, we will take advantage of two separate coupled model frameworks: one from the University of Michigan and one from the HeliosAres effort in France. Outputs from these parallel model frameworks will be archived for use by the team and wider community in a ‘model library’ covering combinations of subsolar longitudes, seasons, solar EUV fluxes, solar wind pressures and IMF directions, to aid in interpreting MAVEN data and enabling estimates of global atmospheric escape. These models will also be available for simulation of specific interesting conditions (i.e. specific events) as they are observed during the mission. The altitude ranges of these models are shown schematically in Fig. 2.

## 4.2 Using Global Models to Characterize Atmospheric Escape and Its Variation

As mentioned in the introduction, global models of the Mars upper atmosphere and near space environment are useful not only in the physical interpretation of MAVEN data, but form an essential part of our strategy for determining global atmospheric escape rates at the current epoch and through time. In situ coverage is limited to single points in time and space along MAVEN’s precessing orbit, while remote-sensing data has greater coverage but requires more inversion and is not as comprehensive in terms of derived quantities. Also, even if MAVEN is fortunate enough to measure atmospheric escape rates over a wide range of solar activity, certain controlling parameters (such as planetary obliquity and EUV flux) will not span the full range of values expected to have prevailed over solar system history. Global models are therefore necessary to bridge these measurement ‘gaps’, both spatially and with respect to the controlling drivers.

Given that the orbital coverage below 250 km in sun-state coordinates over the primary mission (see companion paper by Jakosky et al. 2015, [this issue](#)) amounts to 31 % of the planet and that escape will be measured over different combinations of external drivers (e.g. solar wind pressure, EUV flux etc.), significant spatial interpolation of local measurements will be necessary to characterize global escape rates and their variability. This interpolation will be performed using standard methods of interpolation across a spherical surface. However, given the size of the gaps in coverage, more reliable escape estimates may be possible by scaling the modeled escape fluxes to match data-derived escape fluxes where measurements exist, interpolating the resulting ‘scaling function’ over the spherical surface and calculating global escape rates from that model which has been scaled to fit the data. This technique can be applied separately to different escape channels (e.g. sputtering, pickup ion escape).

As well as utilizing global models for spatial interpolation, we can also make use of them to estimate escape rates during some of the more extreme conditions that are believed to have prevailed over the history of the solar system (Zahnle and Walker 1982). We expect to determine the variability of atmospheric escape rates with the controlling solar and planetary drivers over a limited range of those drivers. This variability can be represented as a multidimensional function, where the dimensions are the different drivers (e.g. solar wind pressure, EUV flux). Similarly to the spatial case, we will perform a straightforward multidimensional extrapolation to estimate escape rates for higher values of these drivers. However, we shall also utilize global models for more extreme solar conditions or different planetary obliquities, using the same technique of scaling up or down model results to match escape estimates, in order to ‘intelligently’ extrapolate escape rates to conditions prevalent in the early solar system. These “extreme case” global models may also differ from “present-day” models in terms of their atmospheric density or composition if, during the course of the MAVEN mission, we come to believe that a more realistic representation of Mars atmospheric escape 3 billion years ago requires a thicker atmosphere. In this way, global models give us greater confidence in our atmospheric escape estimates over solar system history.

### 4.3 Global Model Descriptions

We now describe the two modeling frameworks to be used and their component models. The 3 categories are ground-to-exosphere global circulation models, thermosphere-exosphere Monte Carlo models and MHD/Hybrid global ionosphere-magnetosphere plasma models. In each case we discuss the framework of the Michigan models before the HeliosAres models. Figure 2 shows the altitude ranges covered by each family of models.

#### 4.3.1 Ground-to-Exosphere Global Circulation Models

There exist a number of models of the Mars lower and middle atmosphere, which simulate physical processes on a range of scales, from microscale (Spiga and Forget 2009) to mesoscale (Tyler et al. 2002) and global scales (Hartogh et al. 2005; Kahre et al. 2006). However, only two models currently account for the coupled nature of the neutral and plasma structure, composition, chemistry and dynamics in the thermosphere. The MAVEN team will make use of both, to compare with data to elucidate physical processes and to fill in gaps between measurements. They are described below.

**Mars Global Ionosphere-Thermosphere Model (M-GITM)** M-GITM was recently developed and initially validated at the University of Michigan (Bougher et al. 2015; Pawlowski et al. 2012). The M-GITM model framework combines the terrestrial GITM

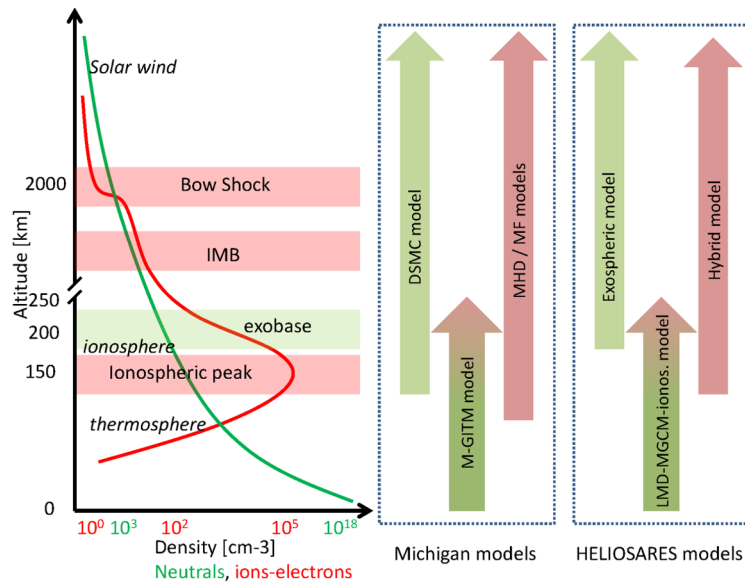


**Fig. 2** Altitude ranges of global models used by MAVEN. The *left panel* shows schematic altitude profiles of neutrals and plasma in the Mars environment. The *right panels* show, on the same vertical scale, the ranges of altitudes covered by of the 3 global models in each of the two model frameworks, with *green* representing neutrals and *purple* representing plasma. In *each* of the *right panels*, the order from left to right is: neutral exosphere model, lower atmosphere-ionosphere model, global plasma interaction model

framework (e.g. Ridley et al. 2006) with Mars fundamental physical parameters, ion-neutral chemistry, and key radiative processes in order to capture the basic observed features of the thermal, compositional, and dynamical structure of the Mars atmosphere from the ground to  $\sim 250$  km. The M-GITM code is a 3-D spherical model that uses an altitude-based vertical coordinate (Deng et al. 2008; Pawlowski and Ridley 2008, 2009a, 2009b; Ridley et al. 2006). This allows for the relaxation of the assumption of hydrostatic equilibrium and enables the model to resolve potentially large vertical velocities resulting from transient events (e.g. CMEs). Unlike the previous Mars Thermosphere General Circulation Model (MTGCM) (see Bougher et al. 2008 and references therein), M-GITM now simulates the conditions of the Martian atmosphere all the way to the surface. Currently, M-GITM assumes photochemical equilibrium when solving for the ionosphere (above  $\sim 80$  km). In the future, ion transport will be included during the process of implementing 2-way coupling of the M-GITM code with the MHD model.

The existing MAVEN library of M-GITM simulations captures the basic observed temperatures and expected wind structures throughout the Mars atmosphere (Bougher et al. 2008; Bougher et al. 2014). Simulated thermosphere-ionosphere fields include: (a) neutral temperatures and densities ( $\text{CO}_2$ ,  $\text{CO}$ ,  $\text{N}_2$ ,  $\text{O}$ ,  $\text{O}_2$ ,  $\text{Ar}$ ), (b) electron and ion densities ( $\text{O}_2^+$ ,  $\text{CO}_2^+$ ,  $\text{O}^+$ ,  $\text{N}_2^+$ ,  $\text{NO}^+$ ), and (c) 3-component neutral winds. Extreme solar cycle plus seasonal conditions for the Mars upper atmosphere provide a good test for any Mars 3-D model to simulate; i.e. for perihelion/solar maximum to aphelion/solar minimum conditions. For these conditions, the MGITM dayside mean exospheric temperature variation is calculated to be  $\sim 200^\circ$  to  $360^\circ$  K, in good agreement with observations and values formerly computed using the MTGCM (Bougher et al. 2008). Figure 3, panels (a) and (c) show simulated temperatures and  $\text{CO}_2$  densities respectively at 180 km.

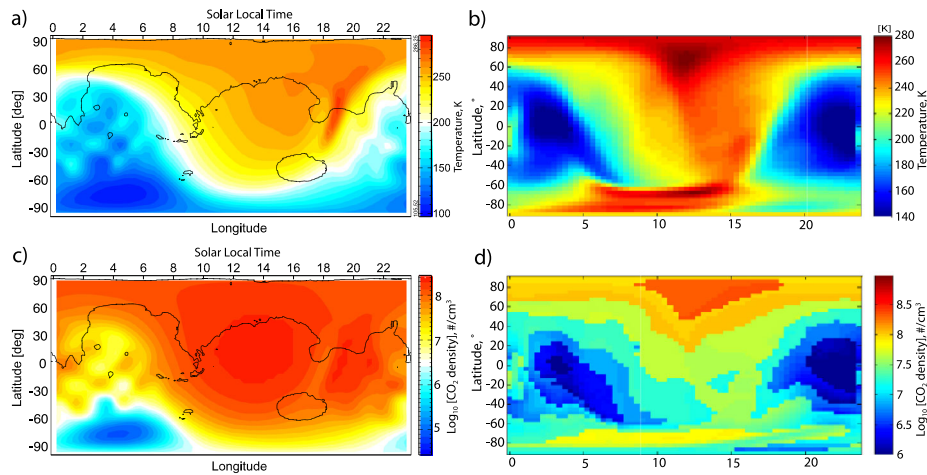


**Fig. 3** Thermosphere-ionosphere model simulations are conducted for Aphelion, solar moderate conditions ( $L_S = 90$ ;  $F_{10.7} = 120\text{--}130$ ). Dust opacities are also prescribed to be globally uniform (integrated vertical opacity = 0.5), appropriate to non-dusty periods. Panels are illustrated for temperatures and  $\text{CO}_2$  densities at 180 km (on a latitude and local time grid) in units of K and  $\#/\text{cm}^3$ , respectively. This altitude is close to the “traditionally defined” exobase. Panels include: (a) M-GITM temperatures, (b) LMD temperatures, (c) M-GITM  $\text{CO}_2$  densities, and (d) LMD  $\text{CO}_2$  densities. Peak dayside (low SZA) temperatures for both models approach  $\sim 250\text{--}260$  K. However, nightside temperatures drop to  $\sim 106$  K (M-GITM) and  $\sim 140$  K (LMD). Strong winter polar warming signatures are present ( $60\text{--}85^\circ\text{S}$ ) in the LMD temperatures that do not appear at the corresponding polar winter latitudes in the M-GITM (the reasons are not precisely known, although it is likely combination of the fact that M-GITM (a) does not have topography turned on and (b) calculates vertical wind velocities using a more accurate method). The associated  $\text{CO}_2$  densities in both models follow the trend of the temperatures, as expected; i.e. maximum  $\text{CO}_2$  densities appear on the dayside where temperatures peak; minimum values are located on the nightside where temperatures are the coldest. The day-night variation is about a factor of  $\sim 1000$  in both models

**LMD Mars General Circulation Model (LMD-MGCM)** A Martian General Circulation Model has been developed at Laboratoire de Météorologie Dynamique (LMD) in Paris and is referred to as the LMD-MGCM. This model is composed of a dynamical core solving the continuity, momentum and energy equations in the Martian atmosphere and a physical core solving the source and loss terms (Forget et al. 1999). In the lower atmosphere it includes radiative heating due to dust and  $\text{CO}_2$  as well as the cooling in the  $15\ \mu\text{m}$  thermal IR of  $\text{CO}_2$ . This model has been enhanced by including various physical processes such as the water cycle (Montmessin 2004), dust and cloud effects on the radiative transfer (Madeleine et al. 2011), photochemical reactions allowing characterization of ozone in the mesosphere (Lefèvre 2004) or by coupling the GCM to a meso-scale model to describe atmosphere-surface interactions (Spiga and Forget 2009). It has also been extended up to approximately 240 km, becoming a three-dimensional ground-to-exosphere model, by adding processes relevant at these altitudes: UV heating, thermal conduction, molecular diffusion and a photochemical model appropriate for the upper atmosphere (Angelats i Coll 2005; González-Galindo et al. 2009). In this model all layers from the surface to the thermosphere are solved self-consistently and feedbacks between layers are naturally taken into account. A new non-Local Thermodynamic Equilibrium as well as a new molecular diffusion scheme have been included to describe the thermosphere. Recently, this model has been improved with an extended chemical scheme including 92 reactions between 25 chemical species. It takes into account photoionization, secondary ionization by X-rays and photo-

electron impact and well describes the lower ionosphere where transport can be neglected (González-Galindo et al. 2013). The study of ionospheric plasma transport on Mars has been newly investigated by including a 3D multifluid dynamical core for several ions species into the LMD-MGCM code. It includes ambipolar diffusion in the ionosphere but crustal and ionospheric magnetic fields are not yet taken into account. Figure 3 panels (b) and (d) show simulated temperatures and CO<sub>2</sub> densities respectively at 180 km.

#### 4.3.2 Monte Carlo Models of the Neutral Thermosphere-Exosphere

Simulation models have been developed to describe the non-collisional region of the upper atmosphere known as the exosphere, extending from the “traditional” exobase (about 200 km) out to interplanetary space. Mars’ neutral exosphere is generally described as consisting of two components: a thermal component which describes the extension of the thermosphere and a suprathermal or ‘hot’ component. Only two published models of this kind exist as of the time of writing and both will be utilized by the MAVEN team. They endeavor to model both of these populations and are described below. A comparison between hot oxygen density simulated by both models is shown in Fig. 4.

**Michigan Adaptive Mesh Particle Simulation (AMPS) Exosphere Model** The exosphere of Mars is modeled at Michigan using a code called AMPS that uses a numerical technique called Direct Simulation Monte Carlo (DSMC) originally developed by Bird (1994). The core of the current AMPS code was constructed for a whole class of generalized rarefied gas flow problems and tested against standard CFD calculations (Tenishev and Combi 2003). As well as other planetary bodies, the DSMC code has recently been applied to Mars’ exosphere (Vaille et al. 2009a, 2009b, 2010).

Basically, the AMPS code is a 3-D Monte Carlo simulator that solves for the coupled Mars thermosphere/ionosphere and exosphere system using an altitude-based coordinate system. Instead of assuming a strict separation between collisional and collisionless domains, the AMPS model considers a collision transitional domain (135 to 600 km altitude). With the DSMC method, a gas flow is represented by a set of (typically millions of) model particles moving in phase space. A probabilistic technique is used to sample the state of collision partners after a momentum exchange event, to simulate scattering and chemical reactions. The approach is based on solving the Boltzmann equation and, hence, is valid for all gas flow regimes presented in the domain of study. Ultimately, DSMC macroscopic properties (density, velocity and temperatures) are computed by appropriately averaging particle masses, locations, velocities, and internal energies using standard gas kinetic theory definitions. For our purposes, the DSMC code provides a complete set of the exospheric macroscopic parameters for the hot atom density, its escape flux, and its return flux to the thermosphere.

For the MAVEN model library, the AMPS model will take advantage of a series of recent improvements. First, it will use inputs from the 3-D MGITM to describe both the sources of hot O and C atoms as well as the collisional environment (which now includes the important minor species N<sub>2</sub> and CO as well the dominant O and CO<sub>2</sub>) for quenching the original hot O and C velocity distributions and regulating both the amount and distribution of atoms in the exosphere as well as their escape rates. In addition, instead of isotropic scattering, the more appropriate forward-peaked angular scattering scheme of Kharchenko et al. (2000) is now used, in conjunction with improved integrated cross sections from Fox and Hać (2014). Global hot O and C distributions in 3D will be provided from these DSMC simulations to the MAVEN team and wider community and as input to the MHD code (see Sect. 4.3.3). Based

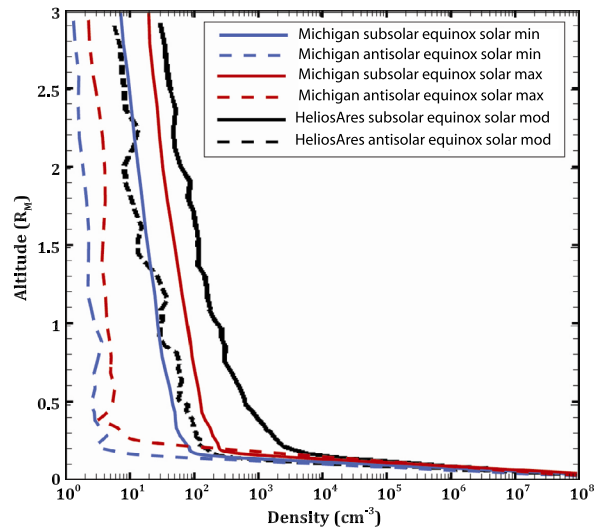


**Fig. 4** Exosphere model simulations are conducted for equinox solar moderate (HeliosAres) and equinox solar maximum plus minimum (DSMC) conditions. These different solar flux conditions can be used to bracket the expected variability of the real Mars upper atmosphere. Both cold (thermal) and hot (non-thermal) profiles of atomic oxygen are plotted (in  $\#/cm^3$  units) over the vertical domain of interest (0–3.0  $R_m$ ) at the subsolar point (local noon) and the anti-solar point (local midnight). In both models, a complete transition from a cold to hot dominated O profile has taken place by about  $\sim 0.20 R_m$ . Both models illustrate dayside hot O profiles that approach similar values at  $\sim 3.0 R_m$ . At lower altitudes (approaching 0.5  $R_m$ ), Michigan hot O densities are somewhat smaller than values from the HeliosAres model. Also, it is noteworthy that the nightside hot O densities are significantly smaller for the Michigan simulation than the HeliosAres simulation. Overall, these comparisons are consistent with global hot oxygen escape rates that are similar for the two models for Equinox solar moderate conditions (Vaille et al. 2009b; Yagi et al. 2012)

on past simulations, these distributions are expected to vary greatly with Mars seasonal and solar cycle conditions (Vaille et al. 2009a, 2009b, 2010). Figure 4 shows DSMC simulated exospheric densities for subsolar and anti-solar equinox solar minimum and solar maximum conditions.

**HeliosAres Exosphere Simulation** The 3D exospheric simulation model developed by Yagi et al. (2012) describes the thermal components of O, CO, CO<sub>2</sub> and O<sub>2</sub>, adopting a Chamberlain approach (Chamberlain 1963) extended to three dimensions with rotation. The non-thermal modeling of oxygen atoms uses a Monte Carlo approach (Leblanc and Johnson 2001). The two main sources at the origin of the non-thermal oxygen corona are dissociative recombination of O<sub>2</sub><sup>+</sup> (Nier and McElroy 1977) and sputtering by reimpacting planetary pickup ions (Chassefière and Leblanc 2004). For the thermal component model, density maps of neutral exospheric species extracted from LMD-MGCM results provide the natural lower boundary condition. The hot oxygen population is described by a Monte-Carlo test-particle approach. Test-particles are followed under the effect of gravity and collisions until they escape or they are thermalized. The Monte-Carlo test-particle model uses the LMD-MGCM density distribution of O and CO<sub>2</sub> to describe the background atmosphere as well as the density distribution of O<sub>2</sub><sup>+</sup> required for the dissociative recombination and represent the source of the test-particles. A similar approach has been used by Vaille et al. (2009b). A detailed discussion on the exospheric model is presented in Yagi et al. (2012) and Kallio

et al. (2011). Figure 4 shows HeliosAres simulated exospheric densities for subsolar and anti-solar equinox solar moderate conditions.

#### 4.3.3 MHD and Hybrid Ionosphere-Magnetosphere Models

Global interaction of the Martian neutral and ionized environment with the solar wind can be modeled with different approaches. Ma and Nagy (2007), Ma et al. (2004), Ledvina et al. (2008) and Kallio et al. (2011) provide comprehensive reviews addressing the different methods, assumptions and limitations of MHD and hybrid approaches. A direct “apples-to-apples” comparison between seven of these models was conducted by Brain et al. (2012), to which the interested reader is directed. To ensure a balance between the two approaches, the MAVEN team will utilize one multi-fluid MHD model and one hybrid model, as described below. Figure 5 compares magnetic fields and flow velocities from the 2 models at  $y = 0$  in the XZ-plane in Mars-Solar-Orbital<sup>1</sup> (MSO) coordinates.

**Michigan Multi-Fluid MHD Model** The multi-fluid global MHD model for Mars is a modified version of the BATS-R-US (Block Adaptive-Tree Solar-wind Roe-type Upwind Scheme) code (Powell et al. 1999; Tóth et al. 2005), which has been under development at the University of Michigan for more than 20 years. The BATS-R-US code uses block-based architecture and an adaptive-mesh-refinement algorithm, which is highly scalable. After years of development, the BATS-R-US code can accommodate not only ideal MHD conditions, but also multi-species, resistive and Hall MHD, and multi-fluid conditions. The multi-fluid MHD code is chosen for use in the MAVEN model library; i.e. this code was recently validated for production simulations and analysis of spacecraft datasets (Najib et al. 2011). For this multi-fluid formulation, separate mass, momentum, and energy equations are solved for the densities of the solar wind protons ( $H^+$ ) and three major ion species ( $O^+$ ,  $O_2^+$ , and  $CO_2^+$ ) in the extended Martian ionosphere. Separate temperatures and velocities are now calculated for each ion. The Mars-solar wind interaction is self-consistently calculated in the MHD model by including the effects of the crustal magnetic fields, ion-neutral and ion-ion collisions, and major chemical reactions. At the upper boundary, upstream solar wind parameters can be specified to accommodate different conditions; e.g. SW density, SW speed, IMF component magnitudes. The MHD model enables the detailed study of Mars ionospheric responses (including the escape fluxes of ions) to these changing SW conditions from the fluid point of view (most appropriate at lower altitudes). Description of the model, as it evolved from a single-fluid to multi-fluid formulation, can be found in Ma and Nagy (2007), Ma et al. (2002, 2004) and Najib et al. (2011).

Three-dimensional neutral thermosphere and exosphere densities plus temperatures are now utilized by the multi-fluid MHD code. The source of these datasets has evolved over the past few years. Previously, the MHD model incorporated the effects of 3-D neutral densities resulting from simulations of the MTGCM (Bougher et al. 2004, 2006, 2008; Bougher and Shinagawa 1998). This model predicts significant variations of the thermospheric density and temperature with solar zenith angle, season, as well as solar cycle. For the MAVEN model library, we now utilize 3-D neutral outputs from M-GITM simulations conducted over the Mars seasons and throughout the solar cycle (see M-GITM description above).

<sup>1</sup>MSO coordinates have the +x axis directed toward the Sun, the +z-axis directed perpendicular to the Mars orbital plane (generally northward), and the +y axis completing the right-hand system (approximately opposite to the instantaneous velocity vector of the planet). Cylindrical coordinates utilize the x-axis, and the distance from the x-axis.

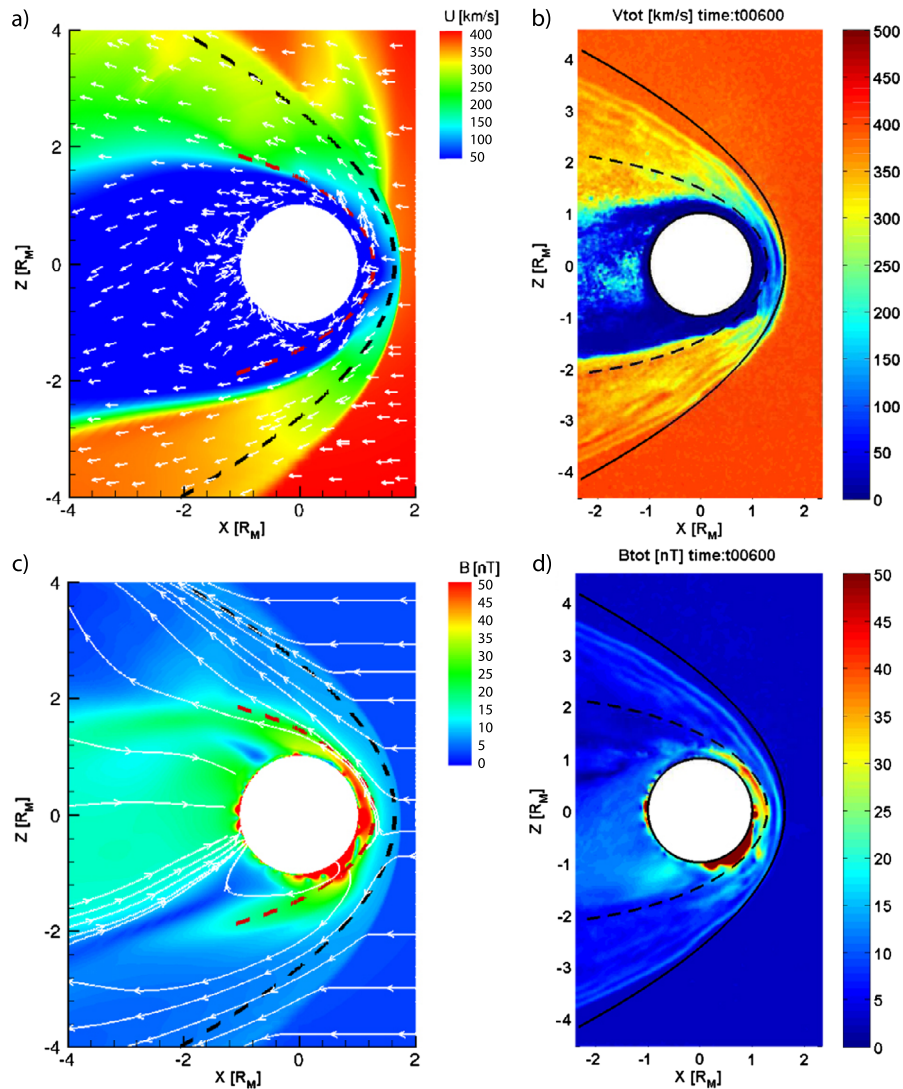


**Fig. 5** Plasma model simulations are conducted for Equinox, solar maximum conditions ( $L_s = 180$ ;  $F_{10.7} = 200$ ). In addition, standard solar wind parameters at Mars are assumed ( $N = 4.0 \text{ cm}^{-3}$ ,  $V = 400 \text{ km/s}$ , the IMF is a Parker spiral in the X-Y plane with an angle of  $56^\circ$  and a magnitude of  $3.0 \text{ nT}$ ). For these simulations, the subsolar position is specified at  $180^\circ\text{W}$  and  $0^\circ\text{N}$  (near the peak crustal field location). Both total bulk ion velocity ( $V_{tot}$ ) and total B-field ( $B_{tot}$ ) are plotted in  $\text{km/s}$  and  $\text{nT}$  units, respectively. Lastly, the Bow Shock (BS) and Magnetosphere Pileup Boundary (MPB) locations (Connerney et al. 2000) are over-plotted. Panels are illustrated in the X-Z plane and include: (a) MHD ( $V_{tot}$ ), (b) Hybrid ( $V_{tot}$ ), (c) MHD ( $B_{tot}$ ), and (d) Hybrid ( $B_{tot}$ ). Both models capture the bulk ion flow and the associated B-field configuration that is consistent with a draped magnetic field and solar wind flow around the planet.  $V_{tot}$  asymmetries in the +Z-direction are apparent for the multi-fluid MHD code

Previously, hot O atom densities were taken from 1-D calculations of Kim et al. (1998), and were assumed to be spherically symmetric. Now, for the MAVEN model library, 3-D hot O distributions from the DSMC code are now being used instead.

**3D Multi-Species Hybrid Model** Modolo et al. (2005) and Modolo et al. (2006) have developed a three-dimensional multi-species hybrid model to characterize the Martian global plasma environment. This approach, based on a kinetic description for ions and a fluid description for electrons, allows characterizing the dynamics of several ion species. It takes into account self-consistently the Hall term and allows ambipolar fields due to electron pressure gradients to exist and break the symmetry of the system. Hall multi-fluid models retain this effect (Najib et al. 2011) in contrast to pseudo-multi-fluid models (Ma et al. 2004). In addition, the hybrid approach includes Larmor radii effects which are expected to become important at high altitudes and therefore describes the oxygen plume along the motional electric field direction ( $E = -v \times B$ ). On the other hand, the computational resources are much larger for the hybrid approach and usually constrain the simulation grid size. In the ionosphere, the plasma dynamic is more fluid-like and an MHD approach, with its refined grid cells, present very detailed structures. The neutral environment, which can be determined from an analytical model or results from a thermosphere-exosphere model, is partly ionized by solar photons, electron impacts and charge exchange with solar wind protons. In the ionosphere a limited set of chemical reactions describing the neutral-ion collisions are introduced (Brain et al. 2010a). More recently, the hybrid model has been parallelized using the Message Passing Interface protocol (MPI), acceding to uniform Cartesian grid cell size of 80 to 50 km resolution (Modolo et al. 2012). Reaching such relatively accurate spatial resolution makes possible the implementation and the description of crustal fields in the hybrid model. The hybrid model, coupled with a test-particle model, allows tackling a variety of physical phenomena occurring in the Martian environment such as X-ray emission (Koutroumpa et al. 2012), characterizing the properties of solar wind protons reflected by the bow shock (Richer et al. 2012), the capture of alpha particle by the Martian atmosphere (Chanteur et al. 2009) or investigating the response of the IMF change on the induced magnetosphere (Modolo et al. 2012).

#### 4.3.4 Model Coupling

**The HeliosAres Approach to Coupling** The different regions (thermosphere-exosphere-ionosphere-magnetosphere) are coupled to each other by the means of energy and matter exchange and transfer of momentum between the different layers, as shown in Fig. 6. None of the simulation models can globally describe all physical processes required to characterize each of these regions simultaneously because although the regions are connected, they are governed by physical processes which have vastly different spatial and time scales. As example, the time step of the LMD-MGCM is of the order of the total simulation time that the hybrid model uses. Therefore a direct coupling, although desirable, is not possible globally. A first order approach is to adapt each model to the other to provide a generic description of the entire interaction. For instance, density distributions of several neutral and ion species computed from the LMD-MGCM model (González-Galindo et al. 2009) are used to fix the lower boundary condition for the exospheric model (Yagi et al. 2012). The three-dimensional thermospheric and exospheric distribution is later used in the hybrid model to provide a realistic description of the Martian neutral reservoir. The hybrid model gives access to precipitated ion fluxes mapped onto the topside atmosphere which can be used after to compute the sputtering contribution to the hot oxygen population (Chaufray et al. 2007). More generally, outputs of each simulation model are used as inputs for the other models. The HELIOSARES project (2009–2014) makes use of the extended LMD-MGCM-ionospheric model (González-Galindo et al. 2013), the multi-species exospheric

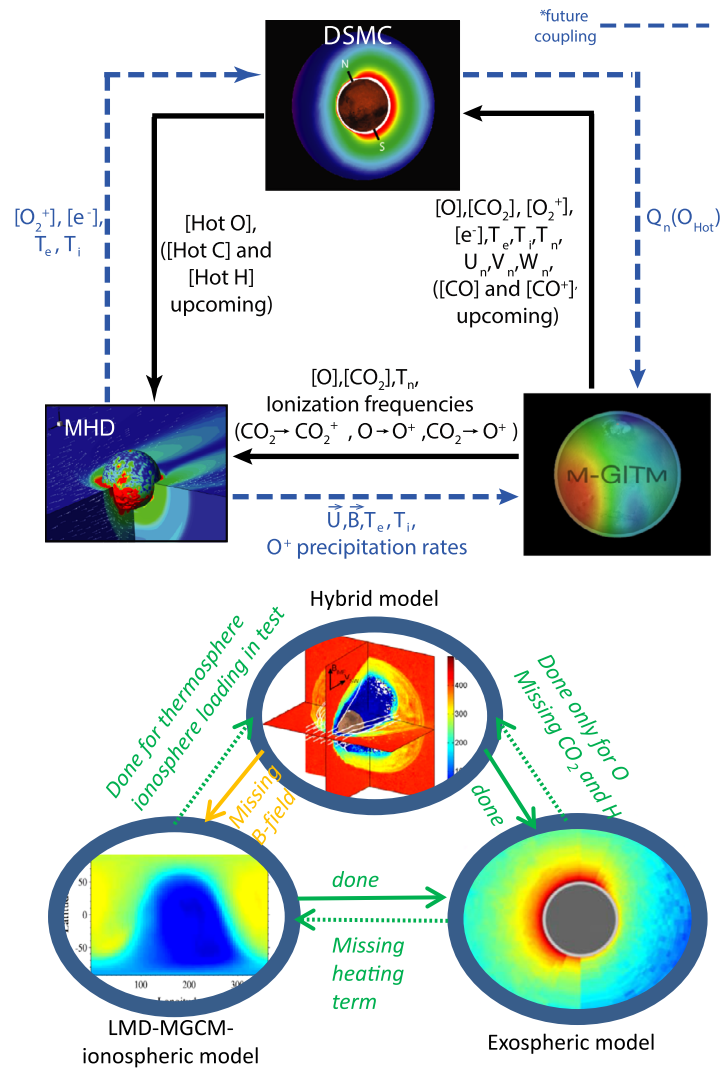


**Fig. 6** Schematic diagram showing the coupling state between the different components of the University of Michigan Space Weather Model Framework (top) and HeliosAres framework (bottom). In the top panel, black solid lines represent completed coupling, via the variables colored black. The dashed blue lines represent future coupling via the variables colored blue. In the bottom panel, green arrows indicate that the coupling is operational while the orange arrow emphasizes that the coupling is not effective yet. Full lines express a completed coupling while dashed lines reveal a partial coupling with some missing inputs

model (Yagi et al. 2012) and Hybrid model (Modolo et al. 2012) to achieve this coupling effort.

**University of Michigan Approach to Coupling** The Michigan strategy for coupling of the thermosphere-ionosphere (M-GITM), exosphere (DSMC) and plasma (MHD) codes involves a phased implementation that takes advantage of what is learned along the path to full coupling of all three codes. These three phases are known as: (a) one way coupling

(upward), (b) one way coupling (downward), and (c) full two-way coupling (up and down). Figure 6 illustrates the current concept of exchange of fields between the separate models. The specific fields for exchange between separate 3-D models will be modified as the Michigan effort proceeds. For the purpose of the construction of the MAVEN model library, one way coupling (upward) is being implemented (solely) to link the outputs from these separate codes: (a) M-GITM thermosphere-ionosphere fields are passed to both the DSMC and MHD codes, and (b) DMSC exosphere fields are passed to the MHD code. Two way coupling is premature at this stage, since we must quantify the relative impacts from one way coupling first.

*The one way (upward) approach* captures the static impact of the mean thermosphere-ionosphere structure (and its periodic variability) upon the exosphere: (a) creation of hot atoms as well as their collisional quenching, (b) regulation of both the amount and global distribution of atoms in the exosphere, and (c) regulation of hot atom escape rates. This one way coupling will help to quantify the role of seasonal and solar cycle variations of the thermosphere-ionosphere structure upon the resulting hot atom distributions and the corresponding escape rates. This one way technique will not permit effects of heating from precipitation of hot particles upon the thermosphere-ionosphere structure to be quantified. In order to address these effects, one way coupling (downward) will be required involving the M-GITM and DSMC codes.

*Likewise, the one way coupling (upward)* captures the static impact of the mean thermosphere-ionosphere-exosphere structure (and its periodic variability) upon the solar wind interaction region: (a) creation of ions from ionization of cold and hot neutral species, (b) regulation of both the amount and global distribution of ions available for escape, and (c) regulation of planetary ion escape rates. This one way coupling will help to quantify the role of seasonal and solar cycle variations of the thermosphere-ionosphere-exosphere system upon the resulting ions distributions in the extended ionosphere and out into the solar wind, and the corresponding escape rates. This one way technique will not permit solar wind impacts upon the thermosphere-ionosphere-exosphere structure to be addressed. These effects include: (a)  $O^+$  (pickup ion) precipitation and the resulting heating and sputtering of the neutral thermosphere, (b) solar wind electron precipitation and the impacts on ionospheric enhancements and neutral heating (both regulated by crustal field topology), and (c) the impacts of ion winds upon the thermosphere-ionosphere structure. Each of these solar wind impacts is currently being examined (or will soon be addressed) using one way coupling (downward) simulations utilizing plasma and thermosphere-ionosphere codes.

*Finally, two way (fully self-consistent) coupling* requires a different framework for the exchange of fields among M-GITM, DSMC, and MHD codes. The Michigan Space Weather Modeling Framework (SWMF) is a flexible computational framework developed to enable the integration of a number of numerical models of the entire sun-solar wind-earth system for space weather modeling (Tóth et al. 2005). The earth GITM model of Ridley et al. (2006) and the BATS-R-US codes have been part of the SWMF for some time. The enhancements needed to enable M-GITM and the DSMC codes to be operational within the SWMF are currently underway.

#### 4.4 The MAVEN Model Library and Its Uses

A 'library' of global simulations of the Mars environment is accessible for use by the MAVEN team and wider community and is expected to cover a wide range of solar, seasonal and plasma conditions. It covers a basic set of combinations and will grow as more simulations are conducted to respond to interesting observations made by MAVEN. These

**Table 2** Initial MAVEN global model library runs planned for University of Michigan coupled model framework. *CR* stands for Conrath parameter. The *columns* describe conditions for each of the 3 models

Parameters	M-GITM (10)	DSMC (10)	Multi-fluid MHD (37)
$L_s$ (season)	0, 90, 270	0, 90, 270	0, 90, 270
F10.7-cm (solar cycle)	70, 130, 200	70, 130, 200	70, 130, 200
Tau (CR) for dust	0.5 (0.003)	0.5 (0.003)	
Solar wind			Nominal
$N$ (#/cm <sup>3</sup> )			4.0
$V$ (km/s)			400
$B$ (nT)			3.0
IMF orientation			57° to Mars-Sun line in the ecliptic plane
Sub-solar B-crustal orientation (180 W is maximum field location)			180 W, 0 W (midnight), 90 W (dawn), 270 W (dusk)
Ancient Mars parameters (2.5 Gyr ago)	F10.7 = 3 × Modern, $L_s = 0$ , Tau (CR) = 0.5 (0.003)	F10.7 = 3 × Modern, $L_s = 0$ , Tau (CR) = 0.5 (0.003)	F10.7 = 3 × Modern, $L_s = 0$ , $N = 4$ , $V = 400$ , $B = 3$ , 180 W, IMF (Nominal)

simulations are particularly suitable to studying separate phenomena relevant to spatial or temporal processes which are difficult to examine with single-point spacecraft measurements alone. In addition it provides three-dimensional context for the in situ observations. Since the model library is finite, interpolation between model runs (e.g. across seasons) may be required for direct comparison with a given MAVEN observation.

The Michigan model library covers the following conditions, as shown in Table 2:

- (1) M-GITM has been run for the three cardinal seasons that correspond to the MAVEN primary mission ( $L_s = 0, 90$  and 270) and for solar minimum, moderate and maximum conditions (F10.7 = 70, 130, 200), totaling 9 simulations, with an integrated vertical dust opacity = 0.5 (global average) with a Conrath parameter = 0.03.
- (2) The Michigan DSMC model has been run for the same 9 conditions using M-GITM as its lower boundary input conditions.
- (3) The multi-fluid MHD model has been run for the same  $L_s$  and F10.7 cases above, plus permutations for Mars crustal field orientations (with respect to 180E longitude position) of 0, 90, 180, and 270 degrees, totaling 36 simulations.
- (4) All 3 models have been run to probe ion and neutral escape for an additional case with an EUV flux of 3 times current solar moderate conditions, i.e. F10.7 = 390, corresponding to ~ 2.5 billion years ago (Zahnle and Walker 1982).

The ‘nominal’ set of model runs described above mostly probes the effects of season, solar EUV and crustal field location. In addition, we have run the multi-fluid MHD model for further 8 cases to probe the effects of different solar wind and IMF conditions, as shown in Table 3.

Table 4 summarizes the different simulations performed by the HELIOSARES project which are available in the MAVEN simulation catalog. The extended LMD-MGCM ionosphere and Monte Carlo exosphere models have been run for the three solar activities corre-

**Table 3** Additional multi-fluid MHD simulation runs completed at the University of Michigan to explore different solar wind and IMF conditions

Case name	SW (density): #/cm <sup>3</sup>	SW (velocity): km/s	<i>B</i> (IMF): nT	Sub-solar <i>B</i> (crystal) orient. wrt
High speed stream	4.0	1000.0	3.0 nT (nominal sign)	0 W (midnight)
SW compression	20.0	400.0	3.0 nT (nominal sign)	0 W (midnight)
High SW dynamic pressure	20.0	1000.0	3.0 nT (nominal sign)	0 W (midnight)
Fast ICME sheath	20.0	1000.0	<i>B</i> (IMF) increased (nominal sign), <i>T</i> <sub>ion</sub> (increased)	0 W (midnight)
ICME driver	4.0	1000.0	<i>B</i> (IMF) increased (nominal sign), <i>T</i> <sub>ion</sub> (nominal)	0 W (midnight)
Rarefaction	0.5	400.0	<i>B</i> (IMF) nominal, 3 nT magn & sign but more radial	0 W (midnight)
IMF Opposite-1 ( <i>L</i> <sub>s</sub> = 90; F10.7 = 70)	4.0	400.0	3.0 nT IMF (opposite sign)	180 W (noontime)
IMF Opposite-2 ( <i>L</i> <sub>s</sub> = 270; F10.7 = 200)	4.0	400.0	3.0 nT IMF (opposite sign)	0 W (midnight)

**Table 4** Global simulation runs completed for the MAVEN model library from the HeliosAres coupled model framework

Parameters	LMD-MGCM (9)	Exosphere (9)	Hybrid global plasma model (6)
<i>L</i> <sub>s</sub> (season)	0, 90, 270	0, 90, 270	0, 90, 270
F10.7-cm (solar cycle)	74, 120, 224	74, 120, 224	120
Tau (CR) for dust	0.5 (0.003)	0.5 (0.003)	
Solar wind			Nominal
<i>N</i> (#/cm <sup>3</sup> )			4.0
<i>V</i> (km/s)			400
<i>B</i> (nT)			3.0
IMF orientation			Normal, Cone angle 90°, near 0°
Sub-solar <i>B</i> -crystal orientation (180 W is maximum field location)			180 W, 90 W

sponding to minimum, mean and maximum solar conditions and for three Martian seasons, leading to 9 runs. These results were used to complete exospheric simulations for the same conditions. Hybrid simulations, using the thermosphere-exosphere-ionosphere description provided by the LMD-MGCM-ionosphere and exospheric models, run with a spatial resolution of about 50 km and are very computationally expensive due to the kinetic treatment of the ions, limiting the number of full runs for the MAVEN model library to six. Our strategy is to have three runs corresponding to one solar activity (F10.7 ~ 120), a nominal solar wind condition and with a crustal field position at 180° W (main crustal field on the dayside) for three different seasons (*L*<sub>s</sub> = 90, 180, 270). Two more runs were performed for the same

solar activity ( $F_{10.7} \sim 120$ ), a given season ( $L_s = 90$ ) but with different IMF directions (IMF cone angles of  $0^\circ$  and  $90^\circ$  in the ecliptic plane). It is therefore possible to determine the influence of the IMF on the Martian ionized environment and plasma escape. Finally the last fully coupled simulation was performed for the same given season ( $L_s = 90$ ), the same solar activity ( $F_{10.7} \sim 120$ ) and nominal solar wind conditions but with crustal fields positioned at  $270^\circ$  W. These runs provide significant inputs to address the seasonal, the IMF orientation and crustal field position influence on the Martian environment and atmospheric escape.

## 5 How MAVEN Will Characterize Atmospheric Escape Processes

As mentioned earlier, two of the primary MAVEN science goals are to (a) determine global atmospheric escape rates from Mars today and (b) estimate the total escape over time. In order to fulfill these goals, we must utilize a combination of in situ data, remotely-sensed data and a variety of models (thermospheric, exospheric, ionospheric and magnetospheric as described in Sect. 4) to guide intelligent multidimensional interpolation and extrapolation of escape rates, both spatially and across the parameter space of inputs described in Sect. 3.

Escape processes at Mars fall naturally into two broad categories, according to the charge state a given atom or molecule occupies when it achieves escape energy on a path that will not intersect the collisional atmosphere. These categories are *neutral escape* and *ion escape*. The categories are unequal in terms of MAVEN's measurement capabilities: the latter will be directly measured while the former must be inferred. Nor are these categories entirely distinct: a neutral particle with sufficient energy to escape can be ionized and recorded as an escaping ion. Each has several subcategories, according to the process which initially provided the particle with sufficient energy to escape the gravitational attraction of Mars. In this section we discuss how atmospheric escape through these two broad categories and 6 distinct energization processes (3 for each category) will be characterized by the MAVEN mission.

### 5.1 How MAVEN Will Characterize Neutral Escape

The neutral particles that populate Mars' exosphere can be classified in 3 ways. The first is by species, where atomic hydrogen, oxygen, nitrogen, helium, argon and carbon are the primary constituents (in decreasing order of density Chaufray et al. 2007; Valeille et al. 2009b). The second is by the process which brought them to the exosphere from the thermosphere: Jeans, photochemical and sputtering processes are the 3 main avenues by which exospheric particles are initially produced. The third is by their velocity and as a result, whether they are gravitationally bound to Mars or unbound (i.e. escaping). The 2nd and 3rd classifications are linked, in that exospheric particle velocities are mostly determined by physical processes in the thermosphere below. Although all exospheric particles are important for understanding escape (since the exosphere is also the source for pickup ion escape), the next 3 subsections will focus on how MAVEN data will enable characterization of fluxes of neutral particles which reach the collisionless exosphere with sufficient energy to escape Mars, and how those fluxes vary with solar and planetary drivers.

Though the exobase is not a distinct boundary and significant atmospheric escape can originate from a few scale heights below it (Fox and Hać 2010), it remains a convenient altitude to represent the transition from the collisional to collisionless regimes. The exobase altitude at Mars is typically near 200 km but varies with Martian season and solar cycle

**Table 5** Escape energies (eV) at 200 km altitude of 12 species found in the Martian atmosphere

Species	H	H <sub>2</sub>	He	C	N	O	CO	N <sub>2</sub>	NO	O <sub>2</sub>	Ar	CO <sub>2</sub>
a.m.u.	1	2	4	12	14	16	28	28	30	32	40	44
Escape energy (eV)	0.124	0.248	0.496	1.49	1.73	1.98	3.47	3.47	3.72	3.97	4.95	5.45

(Vaille et al. 2009a, 2009b). The escape velocity at 200 km is 4.87 km/s or an equivalent kinetic energy of 0.124 eV per a.m.u. (see Table 5 for escape energies for gases present in the Mars atmosphere). There are 3 primary ways a neutral atom or molecule can obtain sufficient energy to escape. First, it can be a thermal particle whose position in the Maxwellian distribution of energies places it above the escape velocity, a process called Jeans escape. Second, an exothermic reaction in the atmosphere can provide the atom or molecule with sufficient energy to escape (i.e., photochemical escape). Lastly, a precipitating ion or neutral can, through elastic collisions, transfer sufficient energy to background neutrals, a process called sputtered (or sputtering) escape.

The MAVEN strategy for constraining neutral escape will utilize both in situ and remote measurements. The direct energy inputs driving neutral escape will be measured as follows: the EUV monitor measures the solar EUV radiation which drives Jeans and photochemical escape, the STATIC (Suprathermal and Thermal Ion Composition) instrument (McFadden et al. 2014, this issue) measures the re-impacting pickup oxygen ions which drive sputtering, the SEP instrument measures the energetic particles which cause ionization and sputtering. Altitude profiles of thermosphere and ionosphere quantities relevant for escape will be measured: the LPW (Langmuir Probe and Waves) instrument (Andersson et al. 2014) measures electron density and temperature, the NGIMS (Neutral Gas and Ion Mass Spectrometer) measures thermal neutral and ion densities, STATIC measures thermal ion temperatures and densities and IUVS measures thermal neutral and CO<sub>2</sub><sup>+</sup> densities. Finally, exospheric densities and temperatures will be measured through IUVS coronal scans, though typically on the opposite side of the planet to the immediately-preceding in situ thermosphere/ionosphere measurements (see companion overview paper by Jakosky et al. 2015, this issue). Hence analysis of coronal scans will proceed separately in parallel with periapsis data.

## 5.2 How MAVEN Will Characterize Jeans' Escape

In this subsection, we focus only on thermal escape of neutrals from the Mars atmosphere, leaving discussion of nonthermal neutral escape mechanisms (i.e. photochemical and sputtered escape) to the following sections. We will describe Jean's escape, discuss what factors may control it, the effect it may have had on Mars climate evolution and discuss how MAVEN data will constrain it.

### 5.2.1 Background

To the extent that a Maxwell-Boltzmann velocity distribution is applicable to the particles in an atmosphere in thermal equilibrium, the fraction of the atoms and molecules that exceed the escape speed from the planet's gravity can be calculated. The process of Jean's escape refers to those particles, generally light atoms, in the high velocity tail of the distribution that are moving upward with greater than escape velocity and which do not suffer further collisions with other particles. The trajectories of upward moving atoms in a planetary exosphere

are often described in a statistical sense by a Chamberlain model (Chamberlain 1977), which is based on the consideration of the phase space density and the application of Liouville's theorem. The atoms are divided into three classes with escaping, ballistic, and orbital motions, and the outputs of the model are the densities of these atoms above the atmosphere. If one knows the temperature of the atmosphere and the planet's mass, one can estimate the Jean's escape flux for each species. In practice, the escape flux decreases rapidly with increasing atomic mass, such that we expect Jean's escape at Mars to be significant only for atomic and molecular hydrogen.

There are two main ways that the actual Jean's escape flux can differ from the Chamberlain model, in which the atoms are assumed to escape from the exobase (which is treated, inappropriately, as a sharp boundary). In practice, one must take into account (1) deviations from the Maxwellian velocity distribution and (2) the true nature of the collisions of H atoms with other neutrals both above and a few scale heights below the exobase to accurately describe the number and velocity of upward-moving atoms that escape further collisions. Ironically it is the exobase region, where collisions are few and far between, where the Chamberlain model approximation assumes thermodynamic equilibrium.

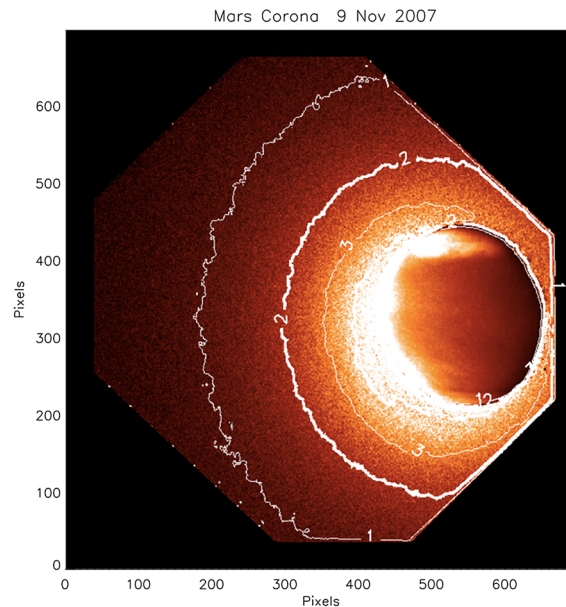
The Jean's escape rate depends only on the density and temperature of thermal hydrogen atoms and molecules in the Mars upper thermosphere. These densities are expected to be highly variable both geographically and with season, depending on dynamics in the lower atmosphere. Temperatures will depend on heating from below (and therefore also on lower atmosphere dynamics) and heating from above (and therefore on solar EUV flux at Mars, i.e. heliocentric distance and solar activity).

In the case of the Martian atmosphere, there is great interest in the escape of water, which can be broken down into consideration of the escape of H and O atoms into space. Water is the main reservoir of hydrogen in the atmosphere, and H atoms originate in water molecules from the surface. Water sublimates into the atmosphere, with a large variation in number density with location and season. The thin atmosphere cannot hold much water, so it is close to saturated in the atmosphere at many times and locations, implying vapor pressure equilibrium with water frozen into the surface. It is possible for near-UV solar photons with sufficient energy to penetrate into the lower Martian atmosphere and photodissociate water into H and OH. The H atoms then recombine into H<sub>2</sub> molecules, which then slowly diffuse into the upper atmosphere. It is estimated that the diffusion time to 110 km altitude is of the order of months, although it is so slow that the models are not able to accurately predict this number (González-Galindo et al. 2009; Forget et al. 1999). In the upper atmosphere H<sub>2</sub> molecules can be photodissociated into H atoms by far-UV solar photons, and the collision rate is insufficient to convert them quickly back into H<sub>2</sub>. The H atoms that then diffuse upward to the exobase level near 200 km altitude can escape by the Jeans' process. In this scenario, the escape rate is controlled both by their temperatures and the resupply of atoms from the lower atmosphere. The measurement of H<sub>2</sub> in the middle and upper atmosphere is a key parameter to understanding the upward diffusion of hydrogen (Krasnopolsky 2002).

### 5.2.2 *The Hydrogen Corona of Mars*

Escaping H atoms are difficult to measure. The "thermal" hydrogen corona extends many planetary radii in altitude, and it can easily be observed through reflected solar H Ly  $\alpha$  emission. The emitted photons are multiply scattered at all altitudes at which MAVEN regularly observes them (up to  $\sim 1$  Mars radius), and therefore a radiative transfer model must be applied to derive H density from the measured emission brightness. The models indicate that the best-fit H temperature is considerably higher than the background CO<sub>2</sub> atmosphere,

**Fig. 7** UV image of the H Ly  $\alpha$  emission from Mars on 9 Nov. 2007, obtained with the ACS/SBC camera on the Hubble Space Telescope. *Contours* of constant brightness in kilo-Rayleighs are overplotted. The disc emission has been replaced by a far-UV image of Mars owing to a low signal to noise resulting from a strong signal of solar continuum radiation reflected from the disc that must be subtracted (Clarke et al. 2014). The large extent of the Martian hydrogen corona can be clearly seen in this image



yet they have difficulty distinguishing between a single thermal component and a somewhat cooler thermal component with a small fraction of superthermal atoms. The extended hydrogen corona was first observed by Mariner missions in the early 1970's (Anderson 1974). Recent observations have shown that the profiles of intensity with altitude can vary considerably over time, apparently in phase with seasonal changes in the lower atmosphere (Chaffin et al. 2014; Chaufray et al. 2008; Clarke et al. 2014). A campaign of observations of the hydrogen corona by the Hubble Space Telescope and the SPICAM instrument on Mars Express in Fall 2007 found the exospheric H emission (see Fig. 7) to be decreasing on a time scale of weeks, consistent with a seasonal decrease in the number density of H atoms at the exobase and potentially some change in the exospheric temperature. In contrast to the long-standing picture of a slow diffusion rate from the lower atmosphere, the present data require a more rapid source of new H atoms to the upper atmosphere, potentially related to a major dust storm just preceding the campaign observations (Smith 2009). The dust storm increased the temperature and raised the level of water vapor high into the middle atmosphere, providing a source of H atoms not normally present (Maltagliati et al. 2011). Estimates of the Jeans' escape flux of H based on models of the coronal emission provide lower limits to the actual escape flux, given the uncertainty about a superthermal component of H and other nonthermal processes. If it is confirmed that lower atmospheric conditions strongly affect the loss rate of H into space, this will greatly alter the means of extrapolating the loss rate of water back in time over the history of Mars.

### 5.2.3 MAVEN Strategy for Determining Jeans Escape

While, as has been noted, MAVEN will not directly measure the escaping atoms, there are several methods that can constrain the population of atoms that are escaping by the Jeans' process and other means. Unfortunately, NGIMS will not reliably measure the H atom density in situ (its mass range goes down to  $\sim 1.5$  amu), so the primary measurement of the altitude and spatial distribution of H will come from the IUVS (see companion paper

by McClintock et al. 2014). H densities and temperatures will be measured in the upper thermosphere quasi-locally through limb scans from 100 to 220 km altitude, covering that key region of the atmosphere between 110 and 140 km where much of the far-UV sunlight is absorbed and photo- and ion-chemical reactions take place. These properties will also be measured above the exobase over close to an entire hemisphere through IUVS coronal scans. Comparing these microscopic and macroscopic measurements will have great value in updating our knowledge of the structure of Martian hydrogen exosphere.

This vertical structure of hydrogen contains the information we need in order to constrain the Jeans escape flux. The actual escape takes place from the exobase region, above which the atmosphere is collisionless. Ironically, while the H atoms are the easiest to detect through the bright 121.6 nm scattered solar Lyman alpha emission, because the H emission is quite extended (due to the low H mass and relatively weak Martian gravity), it is difficult in practice to separate any nonthermal component of H atoms from the bulk population. The Jeans (i.e. thermal) and non-thermal escape fluxes of H will be constrained by fitting the vertical H structure to forward models that include radiative transfer and vary the temperature and density of thermal atoms as well as the temperature and fraction of “hot” H atoms (i.e. those produced by nonthermal processes, for example dissociative recombination of  $\text{HCO}^+$ ). It is possible that altitude profiles of the optically thin D Ly alpha emission will provide complementary information about the population of hot hydrogen species.

This vertical structure of the Mars hydrogen Corona will be measured on the ‘flanks’ of the MAVEN orbit as it precesses around Mars in MSO coordinates. In this way, MAVEN will probe the three-dimensional structure of both the thermal and nonthermal components of the corona.

### 5.3 How MAVEN Will Characterize Photochemical Escape

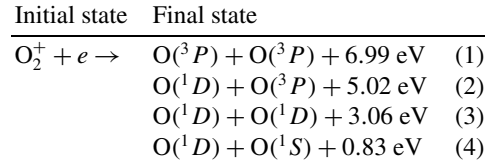
#### 5.3.1 Background

Photochemical escape is broadly defined as a process by which (a) an exothermic reaction results in an upward-traveling neutral particle whose velocity exceeds the escape velocity and (b) the particle is not prevented from escaping through any subsequent collisions with thermal neutrals. It is something of a misnomer because it includes processes (such as electron impact) not initiated by photons. At Mars, the photochemical escape of H, O, N and C atoms is the result of photodissociation, photodissociative ionization and electron-impact dissociative ionization of the primary neutral constituents  $\text{CO}_2$ , CO,  $\text{N}_2$ , CO and  $\text{O}_2$ , as well as dissociative recombination (DR) of  $\text{N}_2^+$ ,  $\text{CO}^+$ ,  $\text{NO}^+$  and  $\text{O}_2^+$  (Fox and Hać 2009). By approximately 2 orders of magnitude the dominant escaping atom is O, mostly the result of DR of  $\text{O}_2^+$  (the dominant ion in the Mars ionosphere Hanson et al. 1976), the pathway upon which we will focus here. The atom production rate for this process depends on the  $\text{O}_2^+$  and electron densities and on the DR rate coefficient,  $\alpha$ . The DR cross section depends on electron velocity, and thus the rate coefficient depends on electron temperature, with a dependence which is best fit by the following expressions determined by Alge et al. (1983) and Chatterjee and Johnsen (1987):

$$\alpha = 1.95 \times 10^{-7} n_e n_{\text{O}_2^+} \left( \frac{300}{T_e} \right)^{0.70} \text{ cm}^{-3} \text{ s}^{-1} \quad T_e < 1200 \text{ K}$$

$$\alpha = 7.39 \times 10^{-8} n_e n_{\text{O}_2^+} \left( \frac{1200}{T_e} \right)^{0.56} \text{ cm}^{-3} \text{ s}^{-1} \quad T_e > 1200 \text{ K}$$
(1)

DR occurs via 4 main channels with the 2 resulting O atoms each leaving with half of the exothermic energy in the center of mass frame of the electron-ion collision as shown below:



The relative likelihoods of these 4 reactions depend on the vibrational and rotational state of  $O_2^+$  (whose distribution is determined by chemical reactions involving  $CO_2$ , O,  $O_2$ ,  $O^+$ ,  $CO_2^+$  and  $CO^+$  and hence varies as their concentrations vary with altitude (Fox and Hać 2009)). In addition, the final energies of the resulting O atoms in the atmospheric rest frame depend on the relative velocities of the electrons and  $O_2^+$  ions and hence on electron and ion temperature. Therefore, the energy distribution of nascent hot oxygen atoms (and the fraction of those with escape energy or greater) varies with altitude, from close to 4 delta functions (with the energies shown in Table 1) at lower thermospheric altitudes to a broad distribution above the exobase (where plasma temperatures are higher). Once created, the statistical likelihood of a hot O atom escaping is dependent on the column of neutrals above it and its collision cross-sections with those neutrals (escape probabilities become significant a couple of scale heights below the exobase Fox and Hać 2009). Therefore, the escape flux of hot O atoms produced by DR of  $O_2^+$  is a complex product of altitude profiles of the density and temperature of electrons, all neutrals and most ions. The same is true for the escape fluxes of hot C and N produced via the dozens of other (less important) photochemical channels in the Martian upper atmosphere.

While all external factors which affect neutral and plasma densities and temperatures will therefore have some effect on photochemical escape, the most important is expected to be EUV flux because electron and  $O_2^+$  production results primarily from photoionization of  $CO_2$  and O (Schunk and Nagy 2000).

### 5.3.2 MAVEN Strategy for Determining Photochemical Escape

As mentioned above, even though photochemical escape will not be directly measured by MAVEN, all the relevant quantities upon which it depends will be measured. LPW will measure electron density and temperature, NGIMS will measure neutral and ion density and STATIC will measure ion density and temperature. For every periapsis pass, we will have an inbound and outbound altitude profile of these quantities. Models of the processes described above must then be applied to this data in order to calculate photochemical escape fluxes. Four separate calculations must be made for every altitude profile:

1. Profiles of  $O_2^+$  DR rates will be calculated from electron temperature, electron density and  $O_2^+$  density. This is straightforward using Eq. (1).
2. Profiles of rotational and vibrational distributions of  $O_2^+$  ions will be calculated from profiles of  $CO_2$ , O,  $O_2$ ,  $O^+$ ,  $CO_2^+$  and  $CO^+$  via a lookup table from an empirical model based on the framework of Fox and Hać (2009).
3. Profiles of energy distributions of hot O atoms will be calculated from the results of step 2 and from profiles of electron and ion temperatures.
4. Profiles of all neutral densities will be input into models of hot O transport in order to calculate photochemical escape fluxes from DR of  $O_2^+$ .

Thus for every orbit we will have 2 calculations of photochemical escape flux: inbound and outbound. As the mission progresses we expect to characterize the photochemical escape as a function of all relevant factors, in particular solar zenith angle and EUV flux. The latter will change with solar activity, solar rotation and Mars heliocentric distance, while MAVEN will sample the former from 0 to 150 degrees as the periapsis location precesses over the primary mission.

### 5.3.3 Models of Hot Oxygen Transport

We intend to employ different models of hot oxygen transport for use in step 4 above. At least 2 will be used operationally (i.e. on every orbit) in order to ensure consistency. Each has its advantages and disadvantages. Below we explain the main features of each model of hot O transport and briefly how they will be used.

**Verlet Monte Carlo Model** This Monte Carlo model is driven by a standard Velocity Verlet algorithm to calculate the 3D trajectory of hot O particles in Mars' gravitational field, although it assumes a spherically symmetric background atmosphere. The time step size is chosen to be 5 % of the local mean free time between collisions. At each time step particles are randomly selected to undergo a collision with the background atmosphere. The collision deflection angle is selected by sampling from a cumulative distribution function constructed from the phase functions of Kharchenko et al. (2000). Hot O particles are tracked until their velocity falls below the escape velocity of Mars, at which point they are re-spawned as a new particle. If a hot O particle achieves an altitude above  $\sim 600$  km with a velocity greater than the escape velocity it is counted as having escaped, otherwise it is reflected back down toward the planet. It runs quickly enough that it will be used operationally to calculate escape fluxes from each individual MAVEN inbound and outbound set of altitude profiles.

**Fox and Hać (2009) Monte Carlo Model** The Monte Carlo hot atom transport model of Fox and Hać (2009) uses a background atmosphere of 12 neutral species on 1 km grid from 80 to 700 km. Energetic O atoms are produced at 1 km altitude resolution on a 0.03 eV energy grid (0–10 eV possible). An initial isotropic angular distribution is assumed. Each particle is followed from production altitude ( $\sim 130$  to 350 km) until it reaches 700 km with  $>$  escape energy or its energy falls below 1.8 eV. Energies and angles of the projectile after collision are based on the theory of the kinematics of two-particle collisions and the phase functions of Kharchenko et al. (2000). The step size is 1/5 of a mean free path or 1 km, whichever is smaller. Although model is 1D, the atmosphere is assumed to be spherical and the particle velocities have x, y and z components, i.e. they can escape sideways. Outputs are escape probabilities as a fn. of altitude and energy of production. The model is explained in detail in the Appendix of Fox and Hać (2009).

**2-Stream Model** The two-stream hot oxygen method was originally designed to simulate the hot oxygen corona of Venus. Both the  $O_2^+$  dissociative recombination and charge exchange sources of hot O can be included.

The hot O angular distribution is represented by two average directions (upward and downward) with the assumption of an average angle with respect to the radial. Isotropic upward and downward distributions are adopted giving cosines of the direction angles of  $\pm 0.5$ . Forward and backward scattering probabilities (for collisions with background gas molecules), and the associated energy losses, are calculated assuming isotropic up and down distributions. These energies/probabilities are inputs into the code, which solves 2 coupled

differential equations for the up and down O fluxes versus altitude and energy. The code uses the collision cross-sections of Kharchenko et al. (2000). The energy spectrum at the top of the model is used to determine the escape flux and can also be put into a “Liouville solver” to provide density altitude profiles.

**3-D DSMC Global Model** The 3-D Mars exosphere DSMC model has been completely described in a series of papers (Vaille et al. 2009a, 2009b, 2010) and also summarized in Sect. 4.3.2. As already mentioned, it is a 3-D global model that requires 3-D global inputs. Hence, regardless of run time, it cannot be used operationally to calculate local photochemical escape fluxes given inputs of neutral and plasma temperatures and densities from single periapsis passes, as is the case for the 1-D models. However, the DSMC code can and will be run with inputs in the form of 3-D densities from empirical models of the Martian thermosphere and ionosphere built up from many MAVEN periapsis passes. The photochemical escape rates of O, C and N thus calculated have the advantage of being truly global and will be compared to ensemble averages calculated from 1-D models from individual periapsis passes. This will help us to identify patterns of photochemical escape that result from heterogeneities in the source regions and hence are best-examined using a 3D code.

#### 5.3.4 Example Calculation of Photochemical Escape from Model Data

To illustrate how we will determine photochemical escape rates from each periapsis pass, we use ‘mock data’ produced by flying through the Michigan Mars Thermosphere Global Circulation Model (MTGCM, the precursor to the M-GITM code described in Sect. 4.3.1) with a predicted MAVEN orbit from November 4, 2014. This particular MTGCM run is for solar maximum equinox conditions. Figure 8 shows the process of turning measured profiles into escape rate estimates. The top row shows the profiles of quantities that will be directly measured by MAVEN: (a) neutral density, (b) ion density and (c) electron and ion temperatures. The colored lines show the primary constituents (from the MTGCM) with trace constituents shown with black dotted and dashed lines as calculated by the model of Fox and Hać (2009). The bottom row shows profiles of derived quantities: (d) the escape probability for a (representative) 3 eV O atom in this environment, (e) the energy distribution of produced hot O atoms (mostly a function of ion temperature) and the dissociative recombination rate of  $O_2^+$  and the production rate of hot O atoms via this mechanism which escape. The derived photochemical escape fluxes from dissociative recombination in this particular case would be  $5 \times 10^7 \text{ cm}^{-2} \text{ s}^{-1}$ . We then multiply by the total surface area of Mars at, say, 300 km altitude to get a global photochemical escape rate for O atoms via DR of  $O_2^+$  of  $8.6 \times 10^{25} \text{ s}^{-1}$  or 74000 tonnes of atomic oxygen per year. After an intensive comparison and development effort in 2012 and 2013, all four of the hot oxygen transport models give the same answer to better than a factor of two for identical mock data inputs.

The MAVEN periapsis will generally be at  $\sim 150$  km, an altitude below which escape probabilities for hot O atoms are typically  $< 10^{-4}$  (Fox and Hać 2009). Therefore we are confident that any downward-extrapolation of model inputs below the periapsis altitude will have a negligible effect on derived photochemical escape rates.

#### 5.3.5 Radial vs. Along-Track Escape Estimates

One-dimensional models of photochemical escape necessarily take vertical (i.e. radial) profiles as input. In reality, the in situ profiles will typically cover  $\sim 12\text{--}14^\circ$  of latitude between altitudes of 170 km and 270 km during periapsis, i.e. the altitude range important for hot

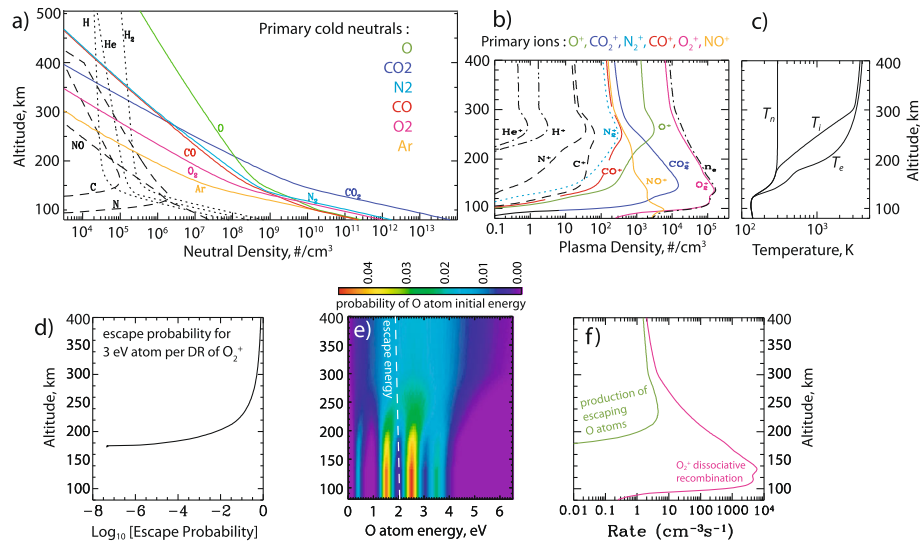


**Fig. 8** Example of how photochemical escape will be derived. “Mock data” altitude profiles of quantities from a predicted MAVEN trajectory for November 4, 2014, are shown in the *top row* and quantities relating to the resulting photochemical escape derived are shown in the *bottom row*. Panel (a) shows cold neutral densities with major species in color, panel (b) shows electron and ion densities with major species in color. Panel (c) shows neutral, ion and electron temperatures. Panel (d) shows the escape probability for a 3eV atom produced as part of isotropic distribution. Panel (e) shows the calculated energy distribution of hot O atoms created by DR of  $O_2^+$ . Panel (f) shows the  $O_2^+$  DR rate and the production rate of O atoms which escape

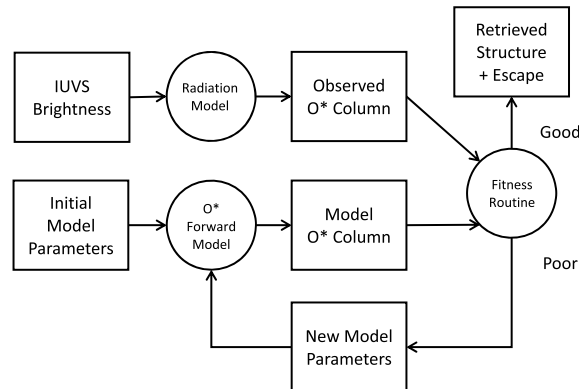
O escape. Sensitivity tests compared calculated escape fluxes from predicted MAVEN trajectories through an MTGCM model run and radial profiles through the same model (both for dayside conditions) at the point where the trajectory crossed the periapsis altitude and found  $< \sim 10\%$  differences in predicted escape fluxes. Therefore, although we will make sure to track the heterogeneity of along-trajectory-derived profiles and estimate the effect on derived escape rates, we are confident that outputs from the aforementioned 1-D models of photochemical escape will be robust.

### 5.3.6 How IUVS Coronal Scans Will Be Used to Constrain Photochemical Escape

Despite all the MAVEN in situ data (neutral densities and plasma densities and temperatures) that will be used to determine photochemical escape rates via the models for described in Sect. 5.3.3, the only direct measurement we will have of hot oxygen (gravitationally bound and escaping) will be IUVS coronal scans.

As MAVEN leaves periapse and moves out toward apoapse on each orbit, the IUVS instrument obtains a coronal scan of the extended atmosphere over the hemisphere of Mars opposite to periapse. This observation probes up to an altitude of  $\sim 3600$  km and one of its primary goals is to provide information on the production and escape of photochemically produced hot O. Unfortunately, simple geometry necessitates that comparison of IUVS coronal observations with periapse in-situ observations of the underlying thermosphere for similar conditions (i.e. SZA, solar hour) will be delayed for the first few months of the mission while waiting for MAVEN’s orbit to precess. However, IUVS also obtains a single limb scan along the line of apsides immediately before beginning its high altitude coronal ob-

**Fig. 9** Flowchart showing algorithm for inverting IUVS coronal scans to obtain exospheric structure and escape rates



servation. This provides valuable information about the atmosphere underlying the coronal scan volume on every orbit.

The retrieval of coronal O densities and hot O escape rates from the observed brightness of the 1304 Å atomic O emission feature requires both a radiation model and hot O transport forward model (see Fig. 9). Once hot O column densities have been derived using the radiation model, the transport model is run iteratively in order to fit the simulated coronal column densities to the observed values. Input parameters to the forward model include the  $O_2^+$  dissociative recombination rate profile and neutral density profiles for the background atmosphere (predominately thermal O,  $CO_2$ ,  $N_2$ , and CO). Initial values for these parameters which will come from the aforementioned line-of-apsides limb scan. Escape rates will thus be derived from coronal scans. As mentioned earlier, the IUVS-derived and in situ-derived escape rates will be on the opposite side of the planet and so will not be directly comparable in real time, nor even statistically (for similar external conditions) until many months into the mission when global coverage of these 2 methods overlaps in Mars-solar coordinates.

Although the hot oxygen corona is expected to be dominated by atoms produced by dissociative recombination of  $O_2^+$ , sputtering (covered in the following section) will also contribute, likely in a highly asymmetric manner. We will need to determine and subtract the sputtering component to use the O 1304 radiance profiles to determine photochemical escape rates.

## 5.4 How MAVEN Will Determine Sputtered Escape Rates

### 5.4.1 Sputtering of the Mars Atmosphere

**Background** Solar wind ions, newly formed planetary ions in Mars' environment and energetic neutral particles regularly precipitate into Mars' atmosphere (Diéval et al. 2013; Luhmann and Kozyra 1991). When such precipitating particles impact the upper atmosphere, they collide with Martian atmospheric particles, inducing momentum transfer, heating and ionization that can lead to atmospheric escape, a process usually called sputtering (Johnson 1994). When a particle impacts an atmosphere, depending on its mass, energy and incident angle, it will lose its energy by elastic nuclear collision or/and by inelastic electronic interaction (Johnson 1994). At energies below a few keV/amu, such particles will lose a significant part of their energy by elastic collisions, leading to 2 types of outcomes.

The first is a single collision ejection, where the incident particle collides with one particle and exchanges most of its momentum with it. As an example, for incident species such as solar wind  $H^+$  and  $He^{++}$ , which are light in comparison to the mass of the target species (at Mars  $CO_2$ , O, CO,  $N_2$ , Ar), the sputtering efficiency or yield (i.e. the ratio between the numbers of ejected particle and of incident ones) is typically much less than one. The 2nd is cascade collisions, for which an incident particle leads to a set of collisions producing several recoils and ejected atoms or molecules. In such a case, typically for particles with mass similar to the impacting particles and with energies above few 10 s of eV/amu, sputtering efficiencies larger than one can be reached. In such cases the incident particles erode the atmosphere by net loss of constituents to space and add a sputtered non-thermal component to the exosphere. Heavier incident ions are most effective in producing these outcomes.

At energies much larger than a few keV/amu, most of the incident energy is lost through electronic collisions with much larger penetration depth of the incident particles and as a consequence relatively low sputtering yield in comparison to collisional regimes induced by keV/amu incident particles (Johnson 1994). When discussing atmospheric escape related to sputtering, theoretical treatments thus usually consider only the 10 eV to few keVs energy range and incident particles with mass larger than He. As an example, Johnson et al. (2000) highlighted that the main driver of Mars' atmospheric escape induced by sputtering should be  $O^+$  ions with energy around 1 keV.

**Dependence of Sputtering on Solar EUV Flux** Chaufray et al. (2007) showed that under typical present-day conditions the contribution to atmospheric escape due to sputtering should be negligible at both solar minimum and maximum compared to photochemical escape rates described in Sect. 5.3, which is confirmed by a recent study by Fang et al. (2013). Based on a coupled magnetospheric and exospheric model, with finite ion gyroradius effects included, these authors concluded that an increase in solar EUV activity should lead to an increase in sputtering rate but to a much smaller degree than predicted by the model of Luhmann and Kozyra (1991) which is based on a gas-dynamic description of Mars' interaction with the solar wind. According to Chaufray et al. (2007), the increases in thermospheric temperature and ionization rate that come with high solar activity increase the solar wind mass loading further from Mars' exobase, slowing it down in the region of most atmospheric ion pickup. Thus they found that even if more pick-up ions are produced because of the higher solar activity, the acceleration close to the exobase is less intense, and the pick-up energy flux reimpacting Mars is lower than suggested by Luhmann et al. (1992). Establishing the variation of the impacting pickup ion flux with solar activity is therefore one of the key pieces of information needed to reconstruct the past evolution of Mars' sputtering.

**Dependence of Sputtering on Solar Wind Conditions** Fang et al. (2013) and Wang et al. (2014) recently studied the role of the solar wind pressure and Interplanetary Magnetic Field (IMF) magnitude on the sputtering efficiency, using pickup ion distributions from a test particle model using electromagnetic fields from an MHD model of the Mars-solar wind interaction (Fang et al. 2013). According to these authors, the increase of the upstream solar wind pressure leads to a more energetic flux of pick-up ions reimpacting the Martian atmosphere and therefore to a more intense ejected flux. It is found that the importance of sputtering loss, in comparison with pickup ion loss, is considerably enhanced when the solar wind is extremely disturbed.

Johnson and Luhmann (1998) suggested that a significant portion of the incident energy should lead to the production of ballistic (i.e. gravitationally bound, non-escaping) particles. These particles can be ionized and in turn re-impact the atmosphere, i.e. a feedback

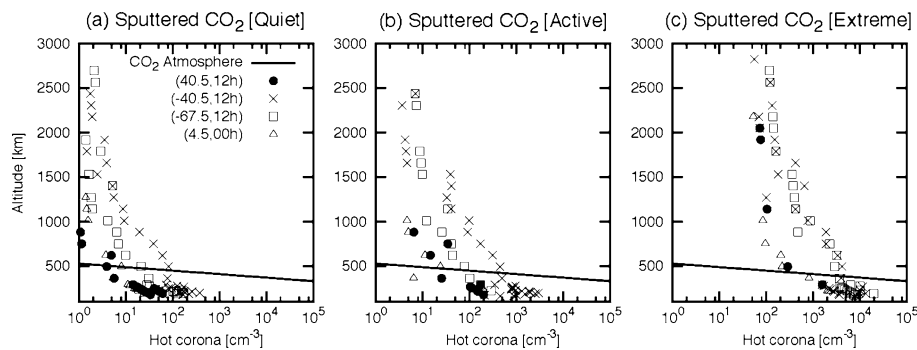


**Fig. 10** Exospheric CO<sub>2</sub> densities as calculated by Wang et al. (2014) for various solar wind conditions from left to right (quiet, active and extreme conditions). The different symbols correspond to different latitudes and local times. The solid line is for the thermal component of the exosphere. Quiet is for a solar wind density of 4 cm<sup>-3</sup>, a solar wind of 400 km/s and a Parker Spiral oriented B field of 3 nT. Active is for a solar wind density of 4 cm<sup>-3</sup>, a solar wind of 1200 km/s and a B field of 3 nT with  $B_y$  only. Extreme case is for a solar wind density of 20 cm<sup>-3</sup>, a solar wind of 1000 km/s and a Parker Spiral oriented B field of 20 nT ( $B_y$  only)

process may increase the sputtering. Cipriani et al. (2007) used 1D coupled Monte-Carlo test-particles and Molecular Dynamic approaches to reconstruct numerically the exospheric profiles generated by sputtering. According to Cipriani et al. (2007), the sputtered contribution to the exosphere is negligible with respect to the dissociative recombination component for most of the exospheric species. At 1000 km altitude, the CO<sub>2</sub> density produced by the normal thermal expansion of the atmosphere is negligible whereas dissociative recombination would produce around 100 CO<sub>2</sub>/cm<sup>3</sup> at 1000 km altitude close to the subsolar region (Cipriani et al. 2007). Wang et al. (2014) found that the density of the sputtered CO<sub>2</sub> should vary from 10 to 1000 CO<sub>2</sub>/cm<sup>3</sup> at 1000 km above the surface from quiet to extreme solar wind conditions (Fig. 10). Therefore, contrary to EUV/UV sputtering dependence, an increase of the solar wind pressure might induce a significant increase of the sputtered exospheric component, of the mass load of the solar wind, of the pick-up ions flux and therefore of the reimpacting component leading to a potentially significant feedback process on the sputtering escape rate (Johnson and Luhmann 1998).

Wang et al. (2014) and Fang et al. (2013) also estimated the heating rate due to the precipitating particles and suggested that for extreme solar wind conditions (e.g. CME encounter), the heating rate close to the exobase due to the precipitating particles could be significant compared to the EUV/UV solar flux.

#### 5.4.2 MAVEN Strategy for Determining Sputtered Escape Rates

As mentioned earlier, MAVEN will not directly measure escaping neutrals and their energies. However, we plan to constrain sputtering escape rates using two complementary techniques which are indirect and will require a substantial modeling component. The first technique uses in situ measurements of precipitating pickup ions and atmospheric neutral density profiles as inputs to models whose outputs will be sputtered escape rates. The second technique uses remote UV measurements of the hot oxygen corona to try to isolate sputtered contribution to the Martian corona.

**Sputtered Escape Rates from in situ Measurements** MAVEN's most important measurement with respect to sputtering will be the impacting ion flux at and just above the

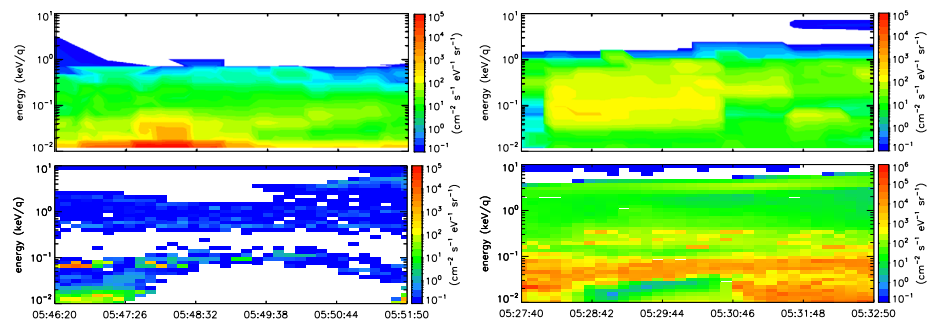


**Fig. 11** Example of energy spectrograms of the precipitating  $O^+$  ions as it may be measured by the STATIC instrument for two portions of orbit of MAVEN. *Left panels*: Outbound part of 2014/10/10 orbit (Northern MSO/MSE hemisphere for altitude between 245 and 487 km). *Right panels*: Outbound part of 2015/9/8 orbit (Southern MSO/MSE hemisphere for altitude between 245 and 487 km). *Top panels*: as obtained by the coupling between hybrid magnetospheric/exospheric model. *Bottom panels*: as obtained by the coupling between MHD magnetospheric/exospheric model. Slightly different scale bars have been used. The Case 1 of Ma et al. (2004) was considered (see legend of Fig. 13)

exobase. STATIC will measure the angular distribution, composition and energy spectrum of these precipitating ions. Long term observations will allow us to determine the dependence of the precipitating flux with respect to external drivers (solar EUV, solar wind velocity and density, IMF direction and strength, the crustal field orientation and seasonal changes in the densities and temperatures in the Martian atmosphere, which is the reservoir for the exosphere).

Such interpretations will be possible thanks to several theoretical tools. As discussed in Sect. 4, two completely independent coupled 3D simulations of the Martian lower atmosphere, thermosphere, ionosphere, exosphere and magnetosphere have been developed separately at the University of Michigan and LATMOS (Paris, France), using MHD and hybrid approaches, respectively. These model frameworks will be at MAVEN's disposal and will be used in conjunction with test-particle models of Chaufray et al. (2007) and Fang et al. (2013) to derive the incident fluxes that should be measured by the STATIC instrument along MAVEN orbits (see examples shown in Fig. 11). This effort based on two different approaches provides alternative options for data comparisons and for determining how well the physics in the models describes what is observed.

As displayed in Fig. 11, significant differences appear between the two simulations. In particular, the hybrid test-particle simulation suggests more energetic (by a few tens of eV) reimpacting pick-up ions at the Mars' exobase than the MHD test-particle simulation. The MHD simulated electric field is generally less intense (by 10 % or more) close to the strong crustal field region in the southern hemisphere than the one simulated with the hybrid code, a difference large enough to explain the differences displayed in Fig. 11 right panels. In contrast, the MHD simulated electric field is more intense in the northern hemisphere. This could lead to a larger acceleration towards the MSE (Mars-Solar-Electric field coordinates) North direction, that is, less impact into the exobase than in the hybrid simulation as suggested by the left panels of Fig. 11 (see also Brain et al. 2010a, for a detailed discussion of the differences between hybrid and MHD approaches). The most important point of Fig. 11 is that both simulations suggest a similar hemispheric asymmetry between the two portions of an orbit with more energetic particles on 2015/8/9 than on 2014/10/10, and obtain a similar range of reimpacting ion energy (typically between few eVs to 1 keV).

We are building a set of representative simulations to describe the variability of the impacting fluxes with respect to solar wind solar EUV flux, Mars' season and the position of the crustal field. This effort to fill up the whole space of potential conditions is needed for our future interpretation of the inherently limited coverage of MAVEN into a global 3D time dependent frame. Starting from the model library of Mars' interaction with the solar wind for various solar and seasonal conditions (see Sect. 4), we plan to reconstruct 3D maps of the reimpacting flux (as partially displayed in Fig. 11) and of the associated sputtered products. The role of solar activity will be analyzed by calculating the reimpacting flux at solar minimum and solar maximum conditions for the same solar wind conditions, season and subsolar longitude. The role of the crustal field will be explored by doing the same calculation with the strongest crustal fields at noon and at the terminator. The role of solar wind pressure will be studied through the comparison of a simulation done for nominal solar wind conditions (few ions per  $\text{cm}^{-3}$  and around 400 km/s) and for extreme ones (ten times larger solar wind density and few times larger solar wind velocity). Lastly, the seasonal effect on the reimpacting flux will be analyzed by comparing two simulations of Mars' environment (coupling thermosphere, ionosphere and magnetosphere models) at  $L_s = 90^\circ$  and  $180^\circ$ . These runs will provide the needed inputs to extrapolate STATIC measurements into global maps of the precipitating flux at Mars' exobase for different external conditions. This will be feasible though the MAVEN periapsis will remain in the northern MSO (Mars Solar Orbital) hemisphere during the first 6 months because, as MGS magnetometer measurements showed (see Sect. 5.5.2), the most probable orientation of the solar wind convection electric field is essentially and equally distributed between the North and South ecliptic directions. In other words, MAVEN periapsis during the first 6 months should cover most of the planet in the MSE coordinate frame which is the most relevant frame to reconstruct the precipitating ions.

In the mean-time, we have developed other tools to derive the two main products of the sputtering of the Martian atmosphere, namely, the escape rate and the exospheric population. From a given local incident flux and energy spectrum of impacting pickup ions, we are able to estimate the escape due to sputtering and the altitude profile of the sputtered component of the exosphere (e.g. based on an approach partially described in Wang et al. 2014), which we can then use to place into context the IUVS-derived exospheric profiles. A 1D multi-species model using realistic thermospheric density profiles has been used to estimate the associated sputtered products (escape flux and exospheric density profiles) for a large set of reimpacting flux (representative of different solar wind conditions, seasons, longitude, latitude and local time). This parametric tool allows us to cover the expected range of solar and planetary conditions and will be used to provide a first estimate of the escaping sputtered flux from any MAVEN measurements of the reimpacting flux (Fig. 12). Theoretically, it will be possible to derive such an estimate for each portion of STATIC measurements covering altitude below 500 km.

After a few months of measurements, STATIC should be able to provide a first global view of the reimpacting flux in the MSE frame for a given position of the strongest crustal field anomaly. 3-D modeling of Mars' exosphere and of the sputtered escape as induced by this 2-D map of reimpacting ions will be then possible using the 3D model developed by Leblanc and Johnson (2001). This dual approach (1D and full 3D) to reconstruct the sputtering contribution to Mars' escape atmospheric rate and exospheric density will allow us to reduce the uncertainty in our estimates of escape and to derive a first 3D complete model of Mars' exosphere by taking into account all possible sources of Mars' exosphere (thermal component and non-thermal components due to sputtering and dissociative recombination as previously done in Yagi et al. (2012)).

This 3D map will be then used to reconstruct the observations of IUVS (see next section) during these first months of MAVEN operation, using tools that have been developed in the

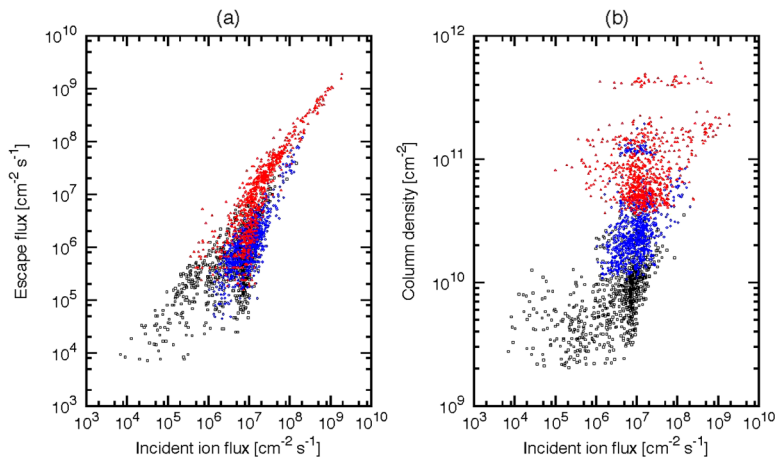


**Fig. 12** Sputtered outputs for various solar wind conditions (*dark circles*: quiet case, *blue circles*: average conditions, *red circles*: extreme conditions; same as in Fig. 10). Each *circle* corresponds to a local reimpacting flux. Escaping fluxes and exospheric column densities are calculated using this reimpacting flux (Wang et al. 2014). *Left panel*: escaping flux for the O atmospheric particles with respect to the total ion flux reimpacting Mars' exobase. *Right panel*: O exospheric column density above the exobase with respect to the total ion flux reimpacting Mars' exobase

frame of the UV spectrometer SPICAM on board Mars Express (Chaufray et al. 2008). The comparisons between IUVS observations and our model outputs will provide a consistent view and set of constraints for our understanding of Mars' sputtering.

**Sputtered Escape Rates from Measurements of Mars' Hot Oxygen Corona** One of the difficulties in identifying clear signatures of sputtering at Mars in the present epoch is that sputtering is not the only process that can produce exospheric particles. In Mars' exosphere, H and O atoms are the dominant species at high altitudes with typical densities of  $10^5 \text{ cm}^{-3}$  at 400 km and of  $10^4$  and  $10^3 \text{ cm}^{-3}$  at 1000 km respectively (Chaufray et al. 2008; Feldman et al. 2011). Other components of Mars' thermosphere, like  $\text{CO}_2$  (Fig. 10), CO and C are also present with much lower densities. The atmosphere of Mars extends above the exobase following to first order the classical Chamberlain profiles leading to the thermal thermospheric and exospheric component (Chamberlain 1963). Sputtering produces suprathermal or 'hot' particles (classically defined as particles with kinetic energy more than three times larger than the local thermal energy) with energies up to  $\sim 10$  eV (Cipriani et al. 2007). As discussed in detail Sect. 5.3.2, dissociative recombination also produces suprathermal particles but with energy below a few eVs (Fox and Hać 1997). As a consequence, whereas thermal particles will preferentially populate the low altitudes, suprathermal particles will be able to reach much higher altitudes and even escape Mars' gravity (escape velocity is  $\sim 5$  km/s which means escape energies are 0.124 eV/amu at the exobase). Chaufray et al. (2007) calculated that the thermal component for the O atoms should dominate the density up to an altitude of  $\sim 500$ –600 km, a result also confirmed by Valeille et al. (2009b) and Yagi et al. (2012). The existence of such a thermal/suprathermal dichotomy in Mars' exospheric profile has been recently confirmed by ALICE/ROSETTA (Feldman et al. 2011). A similar identification for the H component remains ambiguous (Chaufray et al. 2008).

Fortunately, dissociative recombination and sputtering are not driven by the same solar forcing: the solar photon flux controls dissociative recombination while both the photon flux

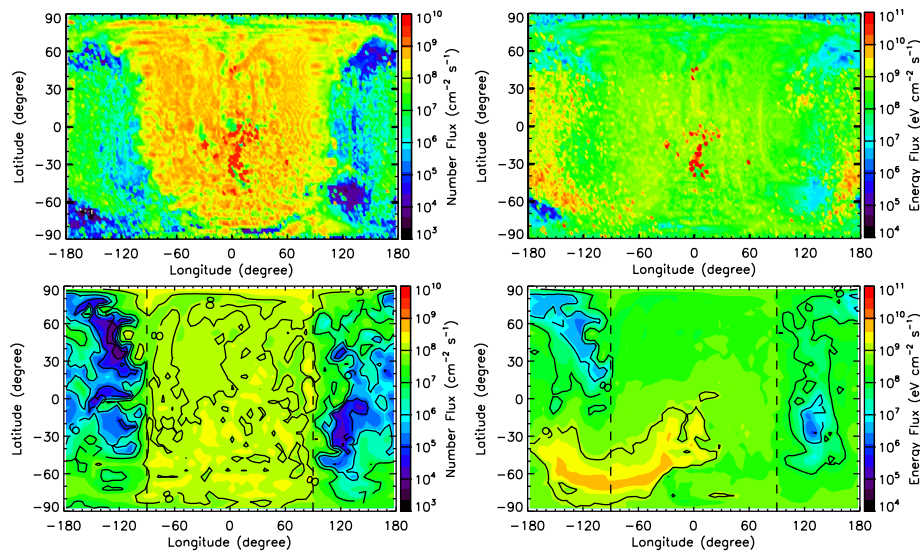


**Fig. 13** Calculated flux of particles impacting Mars' exobase in the Case 1 (Ma 2004) simulation (maximum solar activity, solar wind speed of 400 km/s and solar wind density of  $4 \text{ cm}^{-3}$  with the crustal field placed at noon). *Left panels*: flux in number of  $\text{O}^+/\text{cm}^2/\text{s}$ . *Right panels*: energy flux in  $\text{eV}/\text{cm}^2/\text{s}$ . *Top panel*: as simulated using the hybrid test-particle model. *Bottom panel*: as simulated using the MHD test-particle model. The center of each panel corresponds to the subsolar point. North pole is at the top of each panel. In this simulation, the electric field of convection is pointing towards the North

and the solar wind control sputtering. The solar wind electric field, the density and structure of the neutral exosphere, the position of the crustal fields and EUV-driven photoionization rates, all affect the sputtering process. There must also be some dependence on Martian seasons (Valeille et al. 2009b; Yagi et al. 2012) due to Mars' elliptical orbit and obliquity, and on any feedback process between sputtering and the exosphere (Johnson and Luhmann 1998).

As a first approximation, the acceleration of the ions by the solar wind convection electric field defines the spatial distribution and intensity of the flux of pickup ions impacting Mars' atmosphere. For one of the two most probable orientations of this field, northward or southward depending on whether the interplanetary field component in the ecliptic is eastward or westward, the reimpacting flux is expected to be hemispherically asymmetric. As an example, for a north oriented solar wind convection electric field, accelerated pick-up ions will move in the anti-sunward direction and also towards the North. Following a hybrid test-particle simulation for that configuration (in that case the strongest crustal magnetic field anomalies are placed at midnight), low energy particles (below 10 eV) will impact almost uniformly the dayside exobase (with a slight shift towards the North), whereas the most energetic particles will impact Mars' exobase in the Southern hemisphere (with more than few keV) and the nightside will be impacted by a flux dominated by 100 eV particles.

In the case of the strongest crustal anomalies at noon, this distribution of the reimpacting particles is significantly different. In Fig. 13, we show particle (left panels) and energy (right panels) fluxes as simulated by the hybrid (top panels) and the MHD (bottom panels) test-particle approaches for the strongest crustal field anomalies placed at noon. A good agreement is found for the particle flux in terms of spatial distribution and intensity (left panels). In both simulations, most of the particles reimpact the dayside and similar contrasts

with the nightside are suggested. The main difference between the two simulations concerns the spatial distribution of the energy flux (right panels). We found roughly the same range of intensity and distribution for the energy flux with the exception of the maxima, which are neither placed at the same position nor with the same magnitude. Such differences are difficult to fully explain but are most probably due to differences in the electric and magnetic field intensity and distribution (see discussions above in this section and Brain et al. 2010a, 2010b). These regions of maximum energy flux are influenced by the crustal fields leading to a complex topology of both electric and magnetic field lines. Depending on their orientation with respect to the IMF, the crustal fields may act as cusp-like structures (Leblanc et al. 2002) and locally enhance or reduce the precipitating flux. There are only few measurements by ASPERA-3 on Mars Express that provide information on the precipitation of heavy ions into Mars' atmosphere. Hara et al. (Hara et al. 2011) published one of the only observation of such precipitation and reported fluxes of the order of  $10^5$  to  $10^6 \text{O}^+ \text{cm}^{-2} \text{s}^{-1}$  above 500 eV in energy. This is in good agreement with Fig. 4 simulation, as well as with Chaufray et al. (2007) since Fig. 13 displays the total precipitating heavy ion flux which is largely dominated by low energy range (below 10 eV).

According to Fig. 13, an energy flux of larger than  $10^{10} \text{eV/cm}^2/\text{s}$  might induce a significant local heating of the atmosphere. Fang et al. (2013) also suggested that in the case of enhanced solar activity, sputtering might lead to a significant additional heating of the Martian atmosphere, with as yet undetermined consequences.

Enhanced EUV/UV flux (during solar flares and at active times as an example) will actually increase both sputtering and dissociative recombination processes but on different time scales. In the same way, enhanced solar wind conditions (as an example during a coronal mass ejection encounter with Mars) should lead to specific changes of both processes that are still being explored (Fang et al. 2013; Wang et al. 2014). Perhaps the clearest distinctions between the upper atmospheric/exospheric effects of the two processes however may occur in their spatial distributions. The solar photon flux that creates the ionospheric source of dissociative recombination is symmetric with respect to the subsolar point (although the ionosphere that recombines may have some asymmetries), while the impacting pickup ions that produce the major sputtering effects have hemispheric asymmetries closely tied to the interplanetary magnetic field sector polarity (dawnward or duskward cross-flow component) and to the positions of the crustal fields (Fig. 13).

IUVS observations complement the MAVEN in-situ instruments by determining the sputtered component of atmospheric loss from Mars. During each periapse, 12 limbs scans are obtained from regions of Mars at a distance of typically several hundred km from the spacecraft, each producing species profiles similar those retrieved by NGIMS. On the outbound leg of each orbit IUVS coronal scans sample the extended atmosphere over the hemisphere of Mars opposite the location of periapse. This means that comparison of IUVS coronal observations with in-situ observations under similar conditions (i.e. SZA, solar hour) will be delayed for the first few months of the mission while waiting for MAVEN's orbit to precess. However, IUVS also obtains a single limb scan along the line of apsides immediately before beginning its coronal observation. This provides valuable information about the atmosphere underlying the coronal scan volume on every orbit.

It is expected to be difficult to distinguish sputtering from other non-thermal mechanisms using the individual coronal altitude profiles produced by IUVS. Instead, ensembles of profiles collected under varying conditions will have to be analyzed. For example, coronal profiles gathered on the hemisphere normal to the convection electric field could be statistically compared to those from the opposite hemisphere to isolate the signature of atmospheric sputtering.

A more direct method of detecting global asymmetries is possible using IUVS images taken from apoapse. In this mode IUVS scans across the disk of Mars multiple times, building up a quasi-hemispherical image of the planet and the region off-limb. The off-limb portions of the apoapse images are valuable in providing a global scale measurement of coronal distributions for every MAVEN orbit. By looking for coronal asymmetries in conjunction with solar wind conditions, insight into the magnitude and extent of the sputtering source may be gained.

Each IUVS coronal scan and apoapse imaging segment occurs at the 4.5 hour period of MAVEN's orbit. In addition, each coronal scan is taken over the course of about 30 minutes, while the apoapse imaging takes almost 90 minutes to complete. These operational characteristics set a hard limit on the ability to resolve the time variability of the Martian corona. Investigations of time dependent forcing will therefore be restricted to studying processes which vary on the order of a day or longer.

**A Holistic Approach to Determining Sputtering Rates** MAVEN's objective to observe and reconstruct the effect of sputtering on Mars' atmosphere can be summarized into two main tasks: (1) to identify one or more signatures of sputtering in Mars' exosphere and/or atmosphere and (2) to reconstruct the dependence of those signatures on solar wind conditions (solar dynamical pressure and IMF), solar activity (EUV/UV fluxes) and Mars' seasons.

For task 1, our first target will be the O exosphere that will be observed remotely by IUVS. Here the main challenge will be to distinguish sputtering contribution to the O exospheric density from dissociative recombination and thermal contributions as explained in above. IUVS will observe the exosphere of Mars from apoapsis each orbit over 90 minutes. MAG, SWEA and SWIA will provide the average solar wind conditions (IMF direction and strength and solar wind density and velocity or proxies). A steady period of solar conditions would allow us to associate STATIC reimpacting flux measurement and solar conditions. A few orbits for similar solar conditions placed at various positions in the MSE frame (simulation suggests that less than 10 orbits should be enough) should allow us to reconstruct the average flux reimpacting Mars for such solar conditions. A similar number of orbits should allow us to reconstruct the 3D structure of Mars' exosphere from IUVS measurements. Moreover, the typical time scale for the sputtered O exosphere below 1000 km in altitude to be formed should be less than one hour (because particles with few tenths of eV should need less than one hour to reach 1 Mars radius in altitude), therefore several IUVS observations will probably need to be averaged to get rid of any short term solar variability. However, thanks to our model, we should be able to reconstruct the expected O exosphere due to sputtering for a given average reimpacting flux, to reconstruct the expected signal and to compare those results to IUVS observations.

Task 2 means being able to reconstruct the O sputtered exosphere for a given set of conditions as described previously and ideally to repeat that effort for different solar conditions. It is therefore a long term target that will benefit from both the solar cycle evolution during MAVEN operations, and from active solar periods that represent excellent opportunities to achieve both tasks.

If our comparisons of the models with (1) observations of the IMF-related spatial asymmetries in downward-going pickup ion fluxes, and (2) exospheric density profiles both provide a consistent picture, we will be able to establish a case for the existence and magnitude of sputtering at Mars today. And if our inferred sputtering related escape rates moreover agree with the (weak) values indicated by the models for the present conditions, we will have a benchmark for both assessing solar activity related responses as well as historical consequences of this still most poorly observed but potentially key atmospheric loss process.

## 5.5 How MAVEN Will Characterize Ion Escape

### 5.5.1 Relevant MAVEN Measurements

To determine the rate at which atmospheric particles have escaped Mars, MAVEN must evaluate both neutral particle loss processes, described above, and the loss of charged particles. While neutral loss rates will be inferred from MAVEN measurements, escaping charged particles will be measured directly by the MAVEN instruments. There are, nevertheless, significant challenges to determining contemporary ion loss rates, as well as ion loss rates over Martian history.

The instrument primarily responsible for measuring escaping ions is the SuperThermal And Thermal Ion Composition (STATIC) instrument, described in detail by McFadden et al. (2014, [this issue](#)). STATIC can measure both cold escaping ions and ions that have been accelerated to high energy through their interaction with the Martian plasma environment. It has sufficient mass resolution to detect the primary escaping species  $O^+$ ,  $O_2^+$ ,  $CO_2^+$ , and  $H^+$ . STATIC has the energy range (0.1 eV up to 20 keV), field-of-view ( $360^\circ$  by  $90^\circ$ ), and angular resolution ( $22.5^\circ$  by  $6^\circ$ ) to measure ion velocity distributions, allowing determination of ion flow velocities and pitch angles. These properties are relevant for understanding how ion populations evolve from the location at which they were initially accelerated to the location at which they were measured, and are therefore relevant for determination of the mechanisms that drive ion escape.

Each of STATIC's four data collection modes is designed to emphasize detailed measurements of a different ion population. For example, 'pickup' mode is focused on rapid (16s) measurements of ions in two different mass categories ( $H^+/He^{++}$  and heavy ions) as a function of energy and as a function of direction when the spacecraft is at high altitudes, while 'ram' mode is focused on rapid (4s) measurements of the ion energy spectrum in two mass bins and the ion mass spectrum in four energy bins while the spacecraft is at low altitudes. Each mode will regularly return several other data products at lower cadence, allowing the MAVEN scientists to probe the full distribution of ions in each environment. Second, other high resolution data products for each mode can be downloaded as 'archived' data after the normally-returned ('survey') data products are examined on the ground. Thus, the STATIC observing modes are designed to maximize the information that can be gleaned from in situ measurements of ions at different locations around the planet, within the allowed data rate for the instrument, while still capturing unanticipated ion signatures.

All of the other MAVEN instruments will provide important supporting observations necessary to understand ion escape processes and rates. Vector magnetic field measurements by the Magnetometer (MAG) are required to determine ion pitch angles. The Neutral Gas and Ion Mass Spectrometer (NGIMS) will measure the densities of several key planetary ion species at low altitudes (Mahaffy et al. 2014). Some measured species ( $O^+$ ,  $O_2^+$ ,  $CO_2^+$ ) can be compared directly with STATIC measurements, while others ( $NO^+$ ,  $CO^+$ ,  $N^+$ , and others) will complement STATIC data. The Langmuir Probe with Waves (LPW) will measure electron density and temperature in the low altitude regions where ion outflow is expected to initiate, the spacecraft potential necessary to correct STATIC ion measurements (especially at low energy), and electric field wave power that may accelerate escaping ions (Anderson et al. 2014). The Solar Wind Electron Analyzer (SWEA) will measure the local electron energy distribution, including photoelectron energy distributions that indicate that the spacecraft is on magnetic field lines connected to the ionosphere, and angular distributions that indicate the magnetic topology surrounding the spacecraft (Mitchell et al. 2014). Both indicators are relevant for understanding how and where ions are accelerated away from Mars.

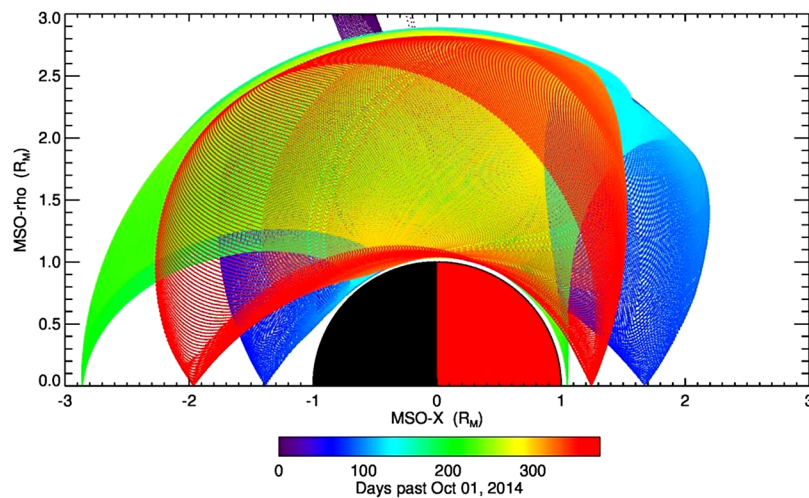


**Fig. 14** Approximate orbital coverage of MAVEN during its nominal mission, in MSO cylindrical coordinates, with the Sun at *right*. MAVEN's planned orbit trajectory is resampled at a 60 second cadence and colored according to time

A number of instruments will provide the global context for measurements of escaping ions. The Imaging UltraViolet Spectrometer (IUVS), which will make remote measurements of ionospheric ion species in the ionospheric reservoir for escape (McClintock et al. 2014). The Solar Wind Ion Analyzer (SWIA) will measure the solar wind ion density, velocity, and temperature—each of which are thought to influence atmospheric ion escape rates (Halekas et al. 2013). MAG will measure the Interplanetary Magnetic Field (IMF) strength and direction (Connerney et al. 2015). The Extreme UltraViolet sensor in LPW will measure the solar photon flux relevant for the production of ions in the upper atmosphere (Eparvier et al. 2014). The Solar Energetic Particle instrument (SEP) will measure the energetic ion input during solar storm periods (flares and coronal mass ejections) (Larson et al. 2015, [this issue](#)).

Thus measurements from all of the MAVEN instruments are necessary to understand ion escape from Mars, from initial production in the upper atmosphere to acceleration and escape from the planet. Making these measurements under different conditions will provide the lever arm necessary for understanding how ion escape rates have evolved over Martian history.

### 5.5.2 Assessing the Contemporary Total Ion Escape Rate

The top-level science goals of the MAVEN mission include a determination of the rate of escape of atmospheric gases today, and a determination of the integrated loss to space through time. The first goal can be achieved by measuring the flux of ions passing through a surface downstream from Mars, and comparing the measurements with models in order to account for locations not visited by the MAVEN spacecraft. Previous missions to Mars have measured escaping ions, and estimated the net escape of atmospheric particles to space (Barabash et al. 2007a; Lundin et al. 1990; Nilsson et al. 2011) For reviews of past work on atmospheric escape from Mars, please refer to Dubinin et al. (2011) or Brain et al. (2015).

The evolution of the MAVEN orbit during the nominal mission is shown in Fig. 14. The figure shows the location of MAVEN over time in MSO cylindrical coordinates, which

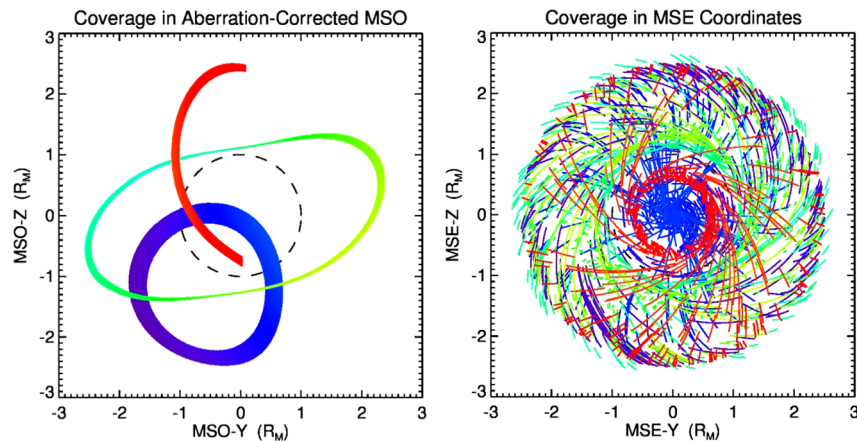
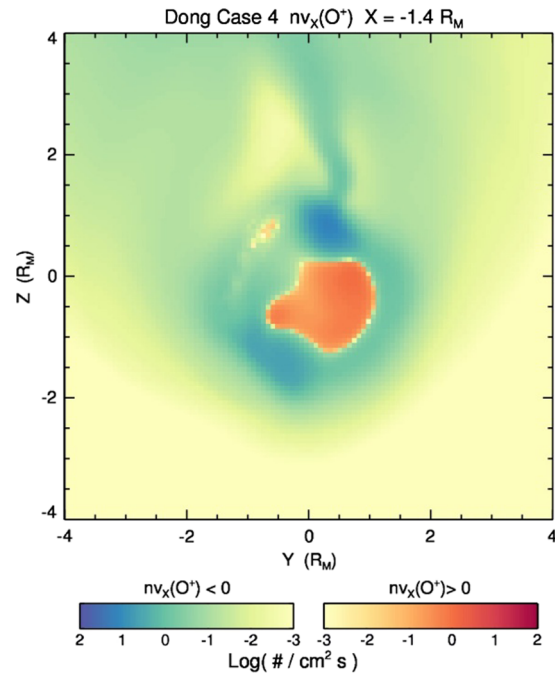


**Fig. 15** MAVEN's coverage in the interval  $-1.41 R_M < \text{MSO-X} < -1.39 R_M$ , colored according to time as in Fig. 14. (Left) coverage is shown in MSO coordinates, corrected for an average solar wind aberration of  $3.5^\circ$ . The dashed line shows the Martian eclipse boundary. (Right) coverage is shown in MSE coordinates, assuming each orbit segment occurred during a steady IMF clock angle direction drawn from the distribution of clock angle directions recorded during the Mars Global Surveyor mission and presented in Brain et al. (2003)

are useful for understanding the spacecraft location with respect to the incident solar wind flow. The figure assumes a nominal ephemeris for MAVEN assuming orbit insertion on approximately October 1, 2014. After an initial commissioning phase, science operations will commence on approximately November 1. The figure demonstrates that MAVEN will measure ions downstream from Mars in a variety of locations, but that the coverage is not complete. To assess ion loss from unmagnetized planets, past missions have examined the flux of ions passing through a planar surface downstream from the planet (e.g. Barabash et al. 2007a, 2007b). If MAVEN adopts a similar approach, then such a surface should be situated near the location where the MAVEN orbit approaches the vicinity of the Mars-sun line in order to obtain the most complete coverage. Thus, ion measurements near  $x = -1.4 R_M$  or near  $x = -1.95 R_M$  are of particular interest. The latter distance will not be well covered until near the end of the MAVEN nominal mission, so we focus here on the plane located  $-1.4 R_M$  downstream from the planet.

The MAVEN coverage in this plane (width of  $0.2 R_M$ , centered at  $-1.4 R_M$ ) is shown in Fig. 15, using two different coordinate systems. The left panel shows the coverage in MSO coordinates, corrected for the few degree aberration introduced by the orbital motion of Mars with respect to the incident solar wind flow. Very little of the MSO y-z plane is covered at this downstream distance. However, we expect escaping ion motion to be strongly influenced by the direction of the upstream solar wind convection electric field (see for example Barabash et al. 2007a). This field direction is determined by the orientation of the IMF, which will be measured by MAG when MAVEN is in the solar wind, and inferred from MAG measurements closer to Mars at other times. Thus we can rotate each of the MAVEN observations into a Mars-Solar-Electric field (MSE) coordinate system, where the z-axis is oriented along the direction of the electric field. We can convolve the MAVEN orbit with the distribution of IMF clock angles at Mars to estimate the orbital coverage of MAVEN in this plane in MSE coordinates. In other words, we randomly select an upstream IMF direction for each MAVEN orbit from the distribution of IMF directions measured by MGS (Brain et al. 2003, #550), and assume this IMF direction is steady over the entire orbit.

**Fig. 16** Flux of atomic oxygen ions 1.4  $R_M$  downstream from Mars, as predicted by a multi-fluid MHD model for nominal solar wind conditions (Dong et al. 2014)

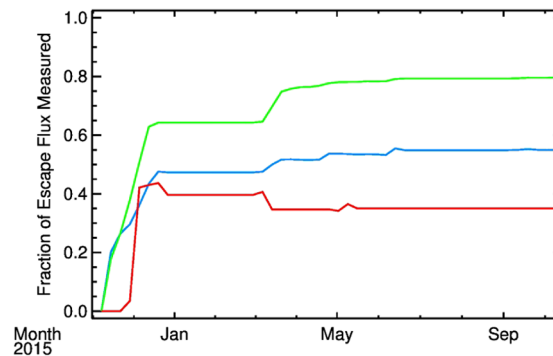


This IMF direction is used to rotate the aberration-corrected MAVEN locations from MSO coordinates into MSE in Fig. 15. We see that the coverage is much more complete in this coordinate system.

Figure 15 (right) shows that MAVEN will not cover the region outside of  $\sim 2.5 R_M$  in this plane. If significant fluxes of escaping ions pass through this unvisited region, then MAVEN will not measure them (at this location—see later discussion). One approach for accounting for this ‘missing’ flux is to appeal to global simulations. As a preliminary exercise we have taken a few representative global simulations and compared them with the MAVEN orbit. These include a single-fluid MHD simulation (Ma and Nagy 2007), a multi-fluid MHD simulation (from Dong et al. 2014, using an improved version of Najib et al. 2011), a hybrid simulation (using a version of the model presented in (Modolo et al. 2006), and a test particle simulation (Fang et al. 2008)). Figure 16 shows  $O^+$  ion fluxes through our test plane as modeled by the multi-fluid model for nominal ( $400 \text{ km/s}$ ;  $4 \text{ cm}^{-3}$ ) solar wind conditions at solar minimum. Non-negligible ion fluxes are observed well outside of  $2.5 R_M$  distances for this model, indicating that some correction will need to be applied to the MAVEN ion loss estimates if the procedure described here is followed. The central region of the Martian tail is dominated in this model by ions returning toward the planet. This feature is common to all four simulation methods, and indicates that special care should be taken with MAVEN measurements to account for such ‘return flux’. Once recognized, it is straightforward to correct the estimate of escape: the net planet-ward flux should simply be subtracted from the net tailward flux to account for the fact that some of the tailward ions in this plane must have reversed direction.

Using the models, one can also estimate how long it will take MAVEN to obtain a reliable estimate of the net escape from the planet. Figure 17 shows the fraction of modeled ion loss that will be observed by MAVEN as a function of time during the mission. To obtain this figure the MAVEN orbit was flown through the simulation results in MSE coordinates (e.g.

**Fig. 17** Fraction of modeled ion loss that MAVEN will observe as a function of time during the nominal mission for three different models (*green*—ideal MHD; *blue*—multi-fluid MHD; *red*—hybrid). Nominal solar wind conditions are assumed throughout



the coverage shown in Fig. 15(right)), and the modeled ion flux (plus or minus up to 50 % noise) was recorded whenever MAVEN was located at  $-1.5 R_M < x < -1.3 R_M$ . Noise is added to the model fluxes to simulate uncertainties in the measurements, and to approximate some statistical spreading. We believe that 50 % error is an overestimate of the measurement uncertainties, but may reasonably approximate the spread in measured fluxes for a given set of upstream conditions. The ion fluxes at all locations were combined to obtain a net loss rate measured by MAVEN, which was compared to the ‘true’ modeled net loss rate passing through our test plane. We see that 50 %–95 % of the net ion loss will be measured by the end of the MAVEN mission, depending upon which model is most accurate. Assuming that a complete dataset is obtained, an initial estimate of ion loss can be obtained from observations recorded in the first 6–8 weeks of the mission, and a more accurate estimate should be possible using data recorded over the first  $\sim 6$  months. An important caveat, discussed further below, is that we have assumed a single set of upstream conditions for our analysis—that there is essentially no variability in the Martian system.

As described above, the STATIC instrument on MAVEN has a limited field-of-view FOV, like all space-borne plasma instruments. The  $360^\circ$  by  $90^\circ$  FOV will leave two ‘holes’ at angles of  $45^\circ$  or more in either direction away from the instrument aperture (McFadden et al. 2014, this issue). STATIC is mounted on the Articulated Payload Platform (APP) of MAVEN, and its orientation at most times will be chosen to maximize measurement of expected particle fluxes. For example, downstream from Mars, STATIC should usually be oriented so that particles flowing parallel to the Mars-Sun line (in either direction) will always be measured. Still, for any given measurement, STATIC may not measure important components of the escaping flux. To our knowledge, analysis of the importance of FOV has not been made for previous measurements of escaping plasma at Mars, nor have they been corrected for this effect. The results of Fig. 17 assume a complete  $4\pi$  steradian FOV, so overestimates the fraction of escaping flux that will actually be measured by STATIC. Figure 18 shows that it may be possible to provide at least a rough correction to the measurements to account for FOV effects. We assumed that the actual ion fluxes through our test plane are perfectly described by different combinations of temperature and global plasma simulation, and determined the fraction of escaping flux that would be measured by STATIC. Figure 18 shows that if the Mars-Sun line is not in STATIC’s FOV then 35–80 % of the escaping flux will not be measured, with the exact value depending upon our assumptions. If the Mars-Sun line is in STATIC’s FOV, then 10–20 % of the escaping flux is not measured. This result suggests (a) that STATIC should always be oriented so that the Mars-Sun line is in the FOV, and (b) that escaping fluxes can at least be coarsely corrected to account for limited FOV effects. Additionally, MAVEN’s SWIA instrument will provide independent measurements

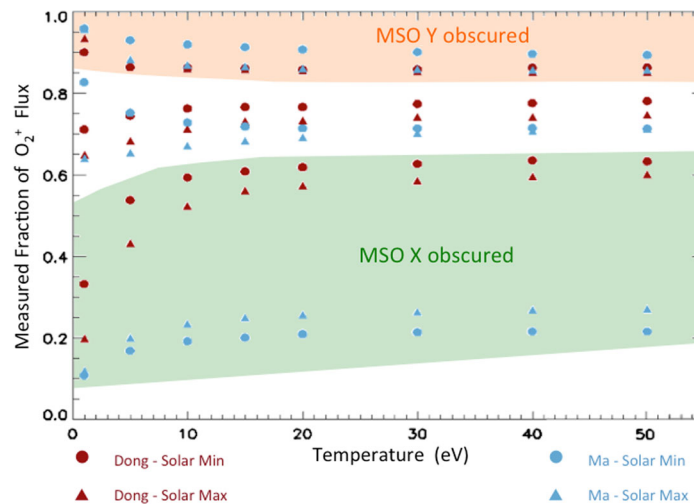


**Fig. 18** Analysis of the influence of STATIC's Field-of-View (FOV) on measurements of ion flux downstream from Mars. Four different simulation results were tested, corresponding to the Multi-fluid MHD simulation by Dong et al. for both solar minimum and solar maximum conditions, and corresponding single fluid MHD simulations by Ma et al. Both models are discussed in the text. For each set of model results, we took the modeled ion flux in the plane 1.4 Mars radii behind the planet, and assumed a Maxwellian distribution with different values of the downstream ion temperature (*horizontal axis*). We convolved the distributions in our 'escape plane' from Fig. 14 with STATIC's FOV for three different instrument orientations. The orientations consider that the hole in the FOV is centered along the MSO x-axis (shaded in *green* in the figure), along the MSO y-axis (shaded in *orange*), and centered at 45° to the x-, y-, and z-axes simultaneously (*not shaded*). For each orientation we computed the fraction of the ambient ion flux that STATIC would measure, as shown in the figure

of escaping ions without mass discrimination. SWIA is mounted to the MAVEN spacecraft body, and will often be oriented so that its FOV is different from the STATIC FOV. It may be possible to use SWIA measurements to independently assess the fraction of escaping ions not measured by STATIC.

Here we examined ion loss through a planar surface downstream from Mars, and demonstrated that MAVEN will not adequately cover this entire surface. This necessitates either the use of correction factors for the data (which in turn necessitates comparison of the data with multiple models to determine which best matches the observations), or the use of a different surface through which to evaluate loss. Referring to Fig. 14, we are exploring the use of a non-planar surface (such as a hemisphere) when constructing loss rate estimates. A hemispheric surface, appropriately placed, may take better advantage of MAVEN's orbit to cover the measured ion loss.

The analysis presented here relies on several simplifying assumptions that the MAVEN team will continue to explore during the lead-up to on-orbit observations. First, for much of the analysis, we have assumed that the STATIC field-of-view will allow a complete measurement of the planetary ion distributions. We demonstrated above that it is likely that FOV effects can be accounted for in estimates of escape.

Next, in our initial analysis, we have assumed that a single set of solar and solar wind conditions will be applicable for all MAVEN measurements. In reality MAVEN will make measurements during a variety of external conditions, and we will separate the measurements according to the different drivers to form estimates of escape rates under different conditions. The figure suggests that MAVEN's orbit and mission duration will allow us to

do this. We can form an estimate of the steady-state ion loss rate that becomes reliable using 6 weeks to 6 months of observations, implying that the nominal 1-year MAVEN mission will allow characterization of the variability of ion loss. There are two approaches to accounting for this variability. Ideally, the escape measurements would be used to populate a multi-dimensional distribution function, with dimensions for each of the controlling drivers of escape. In this approach, we could use all of the MAVEN data to fit a multi-dimensional polynomial function for escape flux. In reality, after a single year the parameter space is not likely to be sufficiently populated for this approach to yield a robust result. Instead, MAVEN observations in the primary mission can be used to investigate the influence of each driver individually, similar to the approach for single drivers employed by (Edberg et al. 2010; Lundin et al. 2008; Nilsson et al. 2010).

Third, our analysis assumes that solar wind conditions are steady during an entire MAVEN orbit. MAVEN's measurement of the solar wind drivers will not be contemporaneous with measurements of escaping ion fluxes downstream from Mars, and it is possible that solar wind conditions can change over the hour or more between measurements of drivers and escape. Additionally, MAVEN's precessing orbit will not always allow it to measure the solar wind. It is during these time periods (when MAVEN is close to Mars on the day side) that the spacecraft will reach its most distant night side locations. Both issues can be mitigated in two ways. First, MAVEN's observations inside the interaction region can be used to derive proxies for the solar wind and IMF. Such approaches have been taken with previous missions (e.g. Brain 2005; Brain et al. 2006; Crider et al. 2003; Fedorov et al. 2006; Ramstad et al. 2013), but they add uncertainty to the estimate of upstream drivers. Second, if the Mars Express spacecraft is operational when MAVEN arrives at Mars, it should be possible to use Mars Express measurements of the solar wind density and velocity to help organize the MAVEN measurements of escaping ions. We note that the solar EUV flux will be measured by MAVEN through nearly the entire orbit, even during times when MAVEN doesn't visit the solar wind.

Finally, the analysis relies on the assumption that the MSE coordinate system is adequate for evaluating ion escape. However, the Martian crustal fields add additional variability to the system (Brain et al. 2003; Lundin et al. 2011; Nilsson et al. 2006), including variability associated with the Mars rotation period (e.g. Ma et al. 2014), and hemispheric variability not tied to the solar wind electric field (e.g. Dubinin 2012). The MAVEN measurements must thus also be examined in this context in order to determine the influence that crustal fields have on global escape rates.

### 5.5.3 Isolating Individual Processes Using MAVEN Measurements

The preceding section demonstrates that MAVEN will be able to measure the total ion escape rate from Mars under present conditions, and its variability. These measurements can be coupled with assumptions about the history of the Sun and solar wind to extrapolate the ion escape rate back in time over solar system history. However, a number of physical processes lead to ion escape, and it is likely that the relative importance of the individual processes may have changed with time. Thus, it is desirable to be able to attribute measurements of escaping ions to the mechanism responsible for their escape. Here we discuss how MAVEN will identify signatures of each of the three main processes responsible for ion escape from Mars. The processes are further discussed in the paper by Jakosky et al. (2015, [this issue](#)), and in a recent review by (Brain et al. 2015). We note that it can be difficult to unambiguously classify the many different mechanisms for accelerating and removing ions from a planet's atmosphere. Other reasonable classification schemes for ion loss are possible (e.g. Dubinin

et al. 2011). The classification scheme presented here distinguishes escape via ionization in flowing plasma, escape via terrestrial-like outflow, and escape via shear-related processes at the solar wind-atmosphere interface.

**Ion Pickup Escape** Ion pickup occurs when an atmospheric neutral is ionized above the collisional region of the atmosphere, and a motional ( $v \times B$ ) electric field accelerates the newly created ion away from the planet. Ion production is highest on the dayside of the planet via photoionization and at lower altitudes (where neutral densities are highest). Since the motional electric field points in approximately the same direction throughout the planetary plasma interaction region, pickup ions are expected to primarily leave the planet in the same direction, along the magnetic ‘pole’ direction defined by the upstream electric field direction. Ions produced in the northern MSE hemisphere can gyrate away from the planet unimpeded, while ions produced in the southern hemisphere have some chance of being accelerated back into the atmosphere, causing sputtering (see Sect. 5.4). This asymmetry is evident in Fig. 16, as is a narrow pickup ion ‘plume’ centered in the MSE x-z plane. This plume is reproduced by most global plasma models of the Martian solar wind interaction region (Brain et al. 2010a).

MAVEN will measure the spatial distribution of escaping ions, including their fluxes, masses, and velocities. Additionally, MAVEN will measure the background vector magnetic field and the conditions for which escaping ions were measured. This information can then be compared with models to determine the source of the ions, and whether their observed location is compatible with an acceleration dominated by  $v \times B$ . One productive modeling approach for the study of pickup ions has been the use of Monte Carlo simulations in which the trajectories of test particles are integrated in background electric and magnetic fields (Curry et al. 2011, 2013a; Fang et al. 2008). The background fields often come from self-consistent simulations of the Mars environment.

**Ionospheric Outflow** The term ‘ionospheric outflow’ has its origin in the study of ions escaping from Earth’s atmosphere, in the presence of a global magnetic field. There, ions are energized and escape in cusp regions at high latitudes, via a number of mechanisms. The ions tend to be relatively cold before they are accelerated. As applied to the Martian situation, ‘ionospheric outflow’ is most often used to refer to the acceleration of cold ionospheric plasma via the same mechanisms considered in Earth’s cusp regions—even if these mechanisms occur far from Martian crustal magnetic fields (Andersson et al. 2010). These mechanisms all involve a net electric field pointed outward from the planet, and include wave heating (time-dependent electric fields perpendicular to the ambient field direction), quasi-static auroral acceleration (localized parallel electric fields in cusps), polar wind (outward electric fields created by charge imbalance), and pressure gradient acceleration (outward electric fields created by vertical density and/or temperature gradients).

In order to assess ion outflow processes, MAVEN’s orbit will take it to and below the exobase region in the ionosphere, where cold ionospheric ions are initially accelerated. MAVEN’s instruments will measure the ion flows, their composition, the electron populations and the thermal state of the ions and electrons as well as the magnetic field that orders the geometry of ionized particle trajectories. No previous Mars mission has simultaneously measured all of these vital parameters in all the relevant regions of the atmosphere and plasma environment to enable understanding of the ionospheric acceleration processes. Critical to these cold plasma measurements will be the LPW measurement of the spacecraft potential, to correct for its effect on measured ion energies. MAG and SWEA observations will provide information about the magnetic topology in which ion measurements are made.

Topology and magnetic field orientation is critical to determining when polar wind, auroral, and pressure gradient processes can result in escape and when vertical ion motion will be inhibited. Wave heating will be assessed using this same information, coupled with both electric and magnetic field wave measurements by MAG and LPW. Similar to other escape processes, the efficiency of the different acceleration processes will be correlated with external drivers to understand the potential variation of ion outflow over solar system history.

**Bulk Plasma Escape** Bulk plasma escape involves the transport of coherent portions of the ionosphere into the planet's wake, resulting in escape. 'Clouds' of ionospheric plasma have been reported based on spacecraft observations made at Venus, and are common features of global plasma simulations for Mars (Terada et al. 2009). Observations of possible cloud structures have been made at Mars (Cloutier et al. 1999; Nairn et al. 1991), though it is difficult to distinguish between a detached cloud and irregularities in the ionospheric boundary. Mechanisms that result in bulk escape include instabilities (such as Kelvin-Helmholtz) at the ionopause boundary, release of magnetic tension in the IMF draped in the ionosphere (e.g. the Hall JxB term), and reconnection of the draped solar wind magnetic field with crustal fields. By its nature, bulk escape should result in a non-steady escape of atmospheric ions.

MAVEN has appropriate instrumentation and orbit to assess the importance of bulk escape as an ion loss process for Mars. The spacecraft will make measurements near the interface between the ionosphere (and/or crustal fields) and the shocked solar wind plasma. Included in these measurements will be magnetic field and ion velocity and composition data to determine whether the spacecraft is in vortex-like Kelvin-Helmholtz structures. This information can also be used to determine whether the locally sampled ionosphere is unstable to the Kelvin-Helmholtz instability. Magnetic reconnection exhaust regions can be identified from a combination of magnetic field, ion, and electron measurements. The velocity of large scale flux-rope like structures previously identified downstream from strong crustal fields at Mars (Brain et al. 2010a) can be measured to determine whether they are stationary features (not resulting in escape) or whether they are propagating away from the planet. Finally, ion fluxes in the Martian wake will be measured, and can be compared with a more detailed plasma context to 'bursty' escape fluxes previously identified using Mars Express and Venus Express (Dubinin et al. 2012). Evaluating the escape rates due to bulk processes is complicated by their non-steady nature, and the difficulty in determining when plasma structures are detached from the ionosphere using a single spacecraft. Previous studies have used either steady-state assumptions (Nairn et al. 1991) or estimated the size and frequency of bulk escape events (Brain et al. 2010b; Hara et al. 2014). The MAVEN team is likely to take the latter approach. Regardless, it is clear that MAVEN will significantly advance our understanding of bulk escape processes.

## 5.6 Interconnectedness of Atmospheric Escape Processes

The previous sections have described how MAVEN data will be used to constrain atmospheric escape from Mars in the form of neutral and ion loss, via six identified escape mechanisms. However, we must recognize that there are non-negligible overlaps between neutral and ion escape and difficulties assigning a given energization mechanism to a given escaping particle. The MAVEN science closure strategy requires a reasonable approach to correct for possible double counting in atmospheric escape estimates. Here we discuss a few issues of ambiguity and interconnectedness to be kept in mind.

First, a planetary ion in the Martian magnetotail detected traveling away from Mars may be difficult to assign to one of the escape mechanisms. Both the ion outflow and bulk ion

escape processes produce cold escaping ions at low altitudes, but these ions are accelerated just like any others and mix with ions picked up after being ionized in the exosphere. However patterns of ion escape in the tail may provide clues as to the ion origins. For example, escape measured 2.5 Mars radii away from the center of the tail is more likely to be pickup escape, while closer to the planet near the terminator may well be cross-terminator ion outflow. Disentangling the sources of detected ion escape in the tale will require careful analysis of these patterns as well as comparison with global plasma models.

Second, our estimates of neutral escape via photochemical, Jeans and sputtering processes are subject to the assumption that these particles remain neutral from their initial energization near the exobase until they fully escape the Mars system. However these escaping particles form part of the Martian exosphere and are subject to electron impact ionization with solar wind electrons, charge exchange with solar wind protons and photoionization by solar EUV photons, whereupon they are accelerated by the solar wind convection electric field and either lost via the pickup process or re-impact the atmosphere to cause sputtering. Therefore, estimates must be kept of (a) the fraction of pickup ion loss and (b) the fraction of the flux of sputtering agents (i.e. accelerated O ion) attributable to the ionization of already-escaping neutrals.

Lastly, we must be aware of feedback loops in escape processes. For example, related to the previous point, an increase in solar EUV flux leads to increased photoionization in the atmosphere and hence an increase in photochemical energization of atoms (both bound and escaping), resulting in higher exospheric densities. These higher densities will lead to an increase in the production of pickup ions and hence to an increase in pickup ion escape, but also to an increase in sputtering of hot atoms out of the atmosphere, which will in turn increase exospheric densities and further increase sputtering. Such nonlinear and overlapping behavior amongst escape processes is bound to occur, but will complicate our attempts to neatly characterize and compartmentalize atmospheric escape.

## 5.7 Path to Global Estimates of Escape Rates

In this section we have described the primary atmospheric escape processes we anticipate to observe at Mars and the MAVEN strategy for determining global escape rates via each of these processes at the present epoch and how those rates vary with external drivers. However, it is useful to examine a high-level representation of the set of paths we will follow from MAVEN measurements to global escape rates, as shown in the flowcharts in Figs. 19, 20 and 21. At the left side of each of these charts are the data from the relevant MAVEN instruments and on the right side are the global escape rates divided up into the 3 neutral escape channels (Jeans', photochemical and sputtering) and a single escape ion channel (comprising pickup escape, ion outflow and bulk escape). Arrows represent the flow of information or logic. Rounded boxes represent models, which can be simple (e.g. straightforward interpolation between data) or complex (e.g. global physics-based models). Rectangular boxes represent any kind of data, either directly-measured or derived from measurements using some kind of model. Boxes or arrows colored black represent MAVEN data. Blue represents models or data derived from models that could be described as 'simple': usually one-dimensional or spherically symmetric with straightforward inputs and outputs. Examples include the sputtering yield model of Wang et al. (2014) (Sect. 5.4.2) and photochemical escape model of Fox and Hać (2009) (Sect. 5.3.3). Red represents models or data derived from models that globally simulate the Martian upper atmosphere and/or near space environment, e.g. the M-GITM model discussed in Sect. 4.3.1. Each instance of a path from left to right

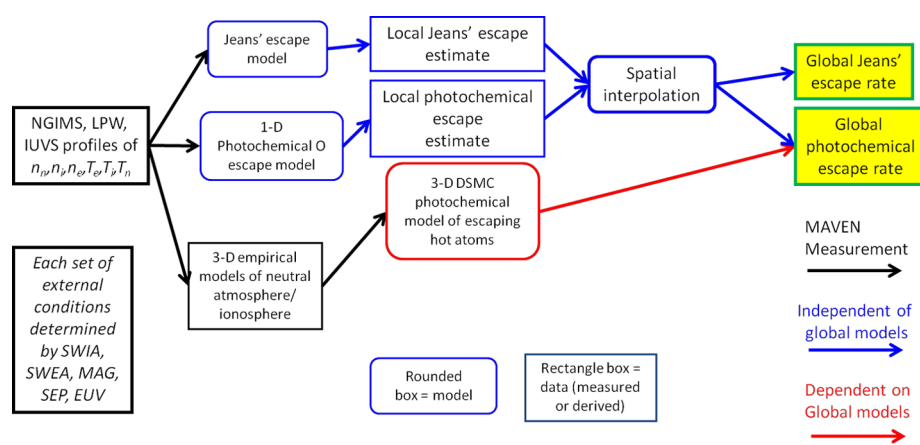


**Fig. 19** Flowchart showing paths from MAVEN data to global Jeans' and photochemical escape rates for each set of external conditions (e.g. IMF direction, solar wind pressure, solar EUV flux, SEP flux etc.). See text above for explanation of boxes, arrows and colors

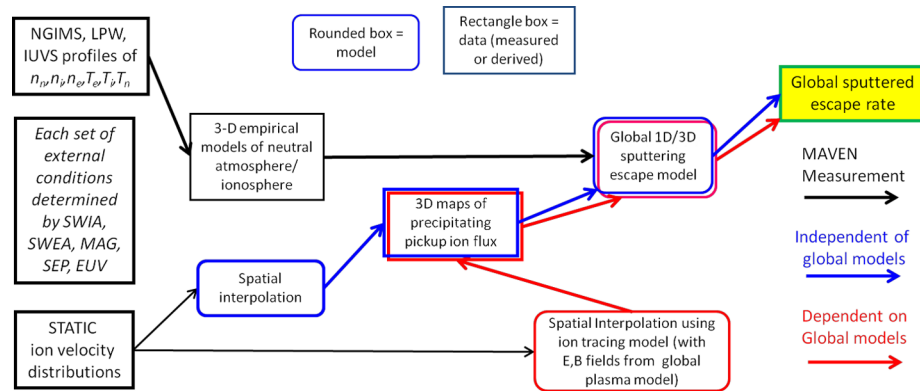


**Fig. 20** Flowchart showing paths from MAVEN data to global sputtering escape rates for each set of external conditions (e.g. IMF direction, solar wind pressure, solar EUV flux, SEP flux etc.). See text above for explanation of boxes, arrows and colors

is assumed to be for a single set of external conditions (e.g. IMF direction, solar wind pressure, solar EUV flux, SEP flux etc.). Even with 3 separate charts, much detail (contained in Sect. 5) is necessarily omitted for the sake of readability and brevity.

Black or blue paths are those which can be followed in a fairly straightforward manner early in the mission and will be the primary path for first results, whereas red paths will require care to ensure that a given global simulation run is appropriate and that the method of model ‘matching’ described in Sect. 4.2 has been validated and gives sensible results.

Figure 19 shows the paths to Jeans' and photochemical escape rates. Jeans' escape of H will be calculated using an appropriate model (see Sect. 5.2) from IUVS limb and coronal scans on each orbit to build up a data set of local escape estimates. For each set of external conditions, these can be spatially interpolated to derive global Jeans' escape rate. The same kind of path will be followed for photochemical escape and will be compared with

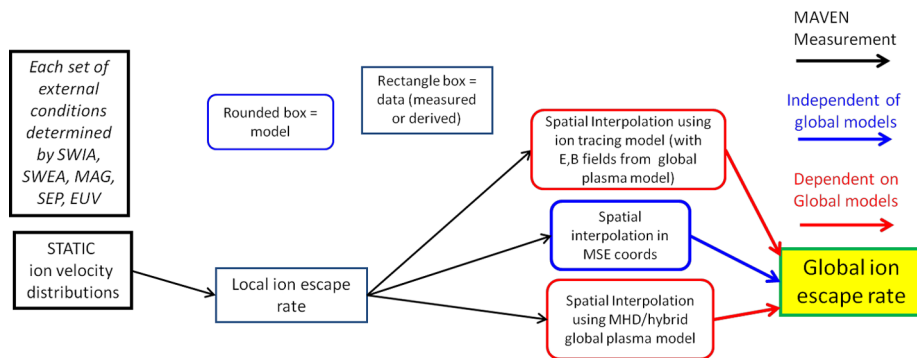


**Fig. 21** Flowchart showing paths from MAVEN data to global ion escape rates for each set of external conditions (e.g. IMF direction, solar wind pressure, solar EUV flux, SEP flux etc.). See text above for explanation of boxes, arrows and colors

an additional set of escape rates derived from 3D global DSMC models, as discussed in Sect. 5.3.

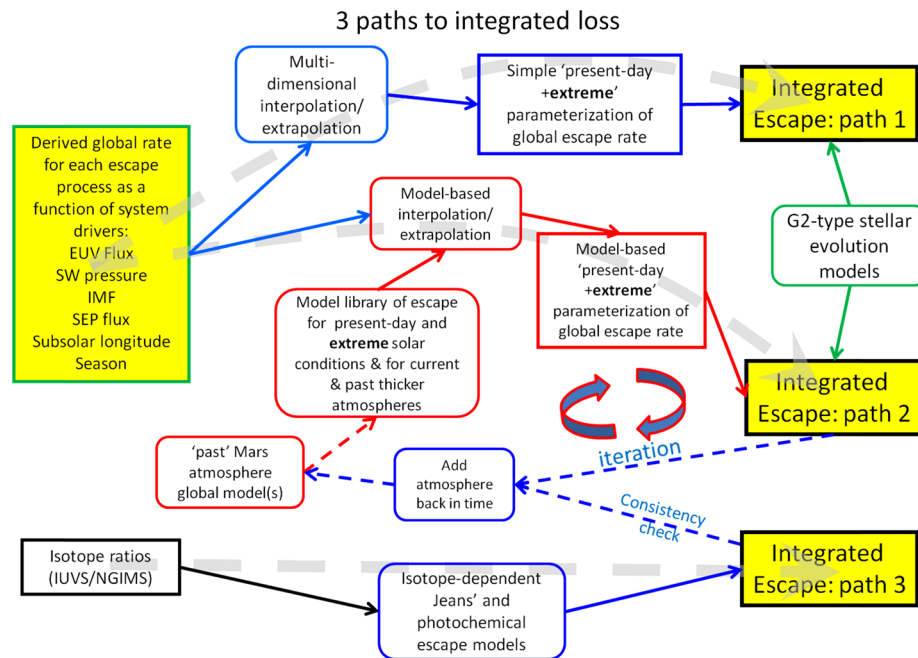
Figure 20 shows the paths to sputtered escape rates. As discussed in Sect. 5.4, three-dimensional maps of precipitating ion flux for a given set of external conditions will be calculated through either spatial interpolation or through assimilation with an ion tracing model. Global sputtered escape rates can then either be calculated by applying these precipitating flux maps to a 1D sputtering yield model separately all over the planet (runs quickly) or a comprehensive 3-D sputtering model. Both models will require global models of the lower atmosphere, most likely empirical models derived from in situ and IUVS data.

Figure 21 shows the paths to ion escape rates. As discussed in Sect. 5.5, local escape rates will be measured directly by STATIC. All these data for a given set of external conditions will then be interpolated using 3 different paths. The simplest path is spatial interpolation in Mars-solar-electric field coordinates and can be done straightforwardly. Two more complex paths would instead use global plasma model results (see Sects. 4.3.3 and 5.5) and to fill in the gaps in a coverage map that may miss important ion loss regions.

The above text and charts represent our pre-mission intentions for calculating global escape rates for a range of solar and solar wind input conditions. The reality will undoubtedly be more complicated. In particular, the response of escape rates to extreme solar wind conditions will be less wellsampled than the quiet-time response due to the relative rarity of those events. Therefore, the aforementioned extrapolations will need to be conducted very carefully.

## 6 Science Question 3: What Has the Integrated Martian Atmospheric Loss Been Through Time?

Answering MAVEN's 3rd major science question is a primary goal of the NASA Mars exploration program. Placing meaningful constraints on the total quantity of atmospheric loss to space from Mars over time is a crucial piece of the puzzle of early Martian climate and hence of habitability. Estimating integrated atmospheric loss requires that science question 2 has been satisfactorily answered, i.e. we must have a reliable picture of the current atmospheric loss rates from Mars via each of the escape channels and understand the physics of how those loss rates depend on the controlling solar and planetary factors. Sections 3, 4



**Fig. 22** Flowchart showing the 3 complementary paths from MAVEN data to estimates of the total amount of integrated escape from Mars, using the same color scheme as Figs. 19, 20 and 21. Curved boxes represent models while rectangles represent data or derived data. Black represents MAVEN data, blue represents models or data derived from models which are either one-dimensional or spherically symmetric and have straightforward inputs and outputs and red represents models or model-derived data which are global in nature and simulate global dynamics. The green box and arrows represent our estimates of the temporal history of solar activity. Light gray arrows represent the 3 paths

and 5 laid out a strategy for determining escape rates at the current epoch. In this section we (more briefly) discuss our strategy for calculating integrated loss over the history of the solar system.

We plan to determine integrated loss via 3 complementary paths. The first path is to take our answers to science question 2, i.e. escape rates determined as a function of controlling drivers, and extrapolate to values of those drivers that prevailed in the early solar system (e.g. higher EUV flux). The 2nd path is more involved and utilizes detailed global simulations of the Mars upper atmosphere and near-space environment, informed by MAVEN data and run with more extreme early solar system input conditions, in order to more intelligently determine escape rates for prior epochs and adding atmosphere back through time in an iterative fashion. The third path will utilize measurements of relative concentrations of isotopes and models of isotope-specific escape rates to estimate what fraction of the various gases has escaped over Martian history.

The first path will be relatively straightforward given the data MAVEN will collect over the primary mission. Whereas the 2nd and 3rd paths, requiring the deepest understanding of escape processes, many global simulations and several iterations back through time, is far more time-consuming and will likely not be complete by the end of the primary mission, although preliminary answers will be available after a few months of data.

These approaches are shown on a single flowchart in Fig. 22. As can be seen, paths 1 and 2 rely on estimates of solar drivers over the last  $\sim 4$  billion years while path 2 also relies

on estimates of planetary properties over the same time to allow global simulations of past conditions. Therefore, before describing each of these approaches, we shall review what is known about the likely history of the solar and planetary drivers of atmospheric escape.

## 6.1 The History of Solar and Planetary Drivers of Atmospheric Escape

MAVEN will be measuring the current variability of global escape rates with respect to internal and external drivers. In order to use this information to infer the historical loss of atmosphere, we require knowledge or confident estimates of how these drivers have varied over solar system history. This has challenges of its own because our knowledge of solar evolution is limited, and we must rely on Sun-like star and stellar wind observations that are also limited. Nevertheless we can make some educated assumptions that provide some constraints on the answers.

### 6.1.1 History of Solar EUV Flux

Solar EUV flux has the best-constrained history of all the solar drivers. Extreme ultraviolet measurements of nearby G-type main sequence stars (the spectral family to which our sun belongs) have been made for several decades. These measurements, combined with a substantial amount of theoretical work on stellar structure and evolution, have led to a reasonably realistic history of solar ultraviolet flux valid for the sun's main sequence phase (i.e. > 50 million years after accretion), as summarized by (Zahnle and Walker 1982). In this history, the 'quiet time' solar spectrum has not varied in time uniformly over wavelength. In longer, near-UV wavelengths like 200 nm, luminosity has not varied substantially since the main sequence began. Whereas in the shorter UV wavelengths more relevant for planetary upper atmospheres, luminosity has varied substantially: for  $\lambda < 30$  nm, luminosities were  $\sim 20$ , 6 and 3 times higher at 4, 3.5 and 2.0 billion years ago. We will use this kind of solar EUV evolution information in extending the global escape rates' variability with EUV today into the past.

An additional aspect of solar EUV that is important to our extrapolations concerns magnetic activity-related variations and extreme enhancements. Activity cycles on Sun-like stars have been inferred and monitored, often using the Calcium K line (Baliunas et al. 1997). These show modulations of the average fluxes in this line that on the Sun originate mainly in the so-called 'plage' areas around active regions. In particular, the younger stars, having ages inferred from both their luminosity and rotation rates, generally appear to be most active. Cyclic activity thus underlies the average trends in EUV flux with stellar age described above. However it likely includes short-lived outbursts or flares that can involve orders of magnitude enhancements. The early Sun was rotating faster and probably generating more or larger active regions. Thus it likely had more frequent flares. Significant x-ray emissions often accompany these flare-enhanced EUV fluxes. Whether flares have observable Martian atmosphere escape consequences has yet to be determined. However if they do, an estimation of early solar flare rates will need to be a part of the MAVEN results application to the past.

### 6.1.2 History of Solar Wind and Its Variations

As mentioned in Sects. 3.1.2, 3.1.3, 5.4.1 and 5.5.3, solar wind parameters have major influences on a number of escape processes. Unfortunately solar wind-like stellar winds around other stars are generally too weak to directly observe. Instead, the existing evidence for them

comes mainly from the disturbances they produce in the interstellar medium around the star (e.g. Woods 2004). These observations confirm the presence of stellar winds but provide only limited insights as to their detailed properties. As a result the extrapolations we make will rely mainly on models of the early solar wind parameters inferred from young Sun-like star properties such as rotation rates. A particular model due to Newkirk et al. (1981) has been used in previous extrapolation studies (e.g. Luhmann and Kozyra 1991) to describe the last  $\sim 3.5$  billion years. This model suggests increasing average velocity, density, and field magnitude trends going back on time that involve values within the ranges of current solar wind parameter variations. Thus a determination of current solar wind parameter dependence of escape rates on MAVEN can be convolved with such a model. But this average condition extrapolation is not sufficient. The most recent review of the state of knowledge of stellar winds and their influence on planetary environments can be found in Lammer (2013).

As is the case for the solar EUV flux, the solar wind parameters include periods of particularly large enhancements. The largest are related to Coronal Mass Ejections (CMEs). Like flares, these sporadic eruptions of coronal plasma and magnetic field are more frequent and often more extreme during the active phases of the solar cycle. Their effects on the solar wind at a particular site depends on how the observer crosses the resulting outward propagating, evolving structure that is known as the ICME (I for interplanetary). For a direct hit, the variation of local solar wind parameters for major events generally includes a leading shock at which density, velocity, magnetic field, and plasma temperatures increase and may stay elevated for many hours. This is the plowed-up solar wind 'sheath' that may by itself have the most significant impacts on the escape rates. The sheath is followed by a period of normal density but still enhanced velocity and magnetic field—the latter of which is now field that has been ejected with the coronal material into the ambient solar wind. MAVEN observations are designed to detect all aspects of the ICME and the Mars upper atmosphere responses to it. Then if we assume that like flares, CMEs were increasingly frequent as we go back in time, we can estimate their particular contributions to the historical escape. It is expected that in parallel with the MAVEN mission, more will be learned about CMEs on other stars that can be brought to bear on this aspect of the extrapolated MAVEN results.

### 6.1.3 History of Solar Energetic Particles (SEPs)

Evidence of energetic particle radiation damage in lunar samples indicates higher average fluxes of these in the past (Walker 1975), consistent with the aforementioned stellar EUV and Calcium-K results suggesting an early, more active Sun. Solar energetic particles (SEPs), protons in the MeV-GeV energy range are of special interest, come from flare sources—but the largest fluxes and energies are related to coronal mass ejection-driven shocks (e.g. Makela et al. 2011). These have been detected at Mars on many spacecraft as instrument backgrounds (e.g. Delory et al. 2012), but also directly by the MARIE instrument on Odyssey (Atwell et al. 2004) et al. Protons of this energy are not much affected by the perturbation Mars makes to the interplanetary medium, and so quite freely rain into its atmosphere. Many even penetrate the atmosphere to the surface where they generate secondary fluxes of neutrons (Gurtner et al. 2005).

As mentioned elsewhere (Bougher et al. 2014), solar particle responses of the Martian atmosphere and ionosphere have been investigated with radio occultation methods with puzzling results (Ulusen et al. 2012). The consequences of this deposition, as well as the lower atmosphere and surface effects of SEPs, is at least partly addressable with MAVEN measurements—perhaps together with measurements from the RAD (Radiation Assessment Detector) (Hassler et al. 2012) on the Curiosity Rover. Whether escape rates such as sputtering losses are significantly affected by this particular element of the space environment

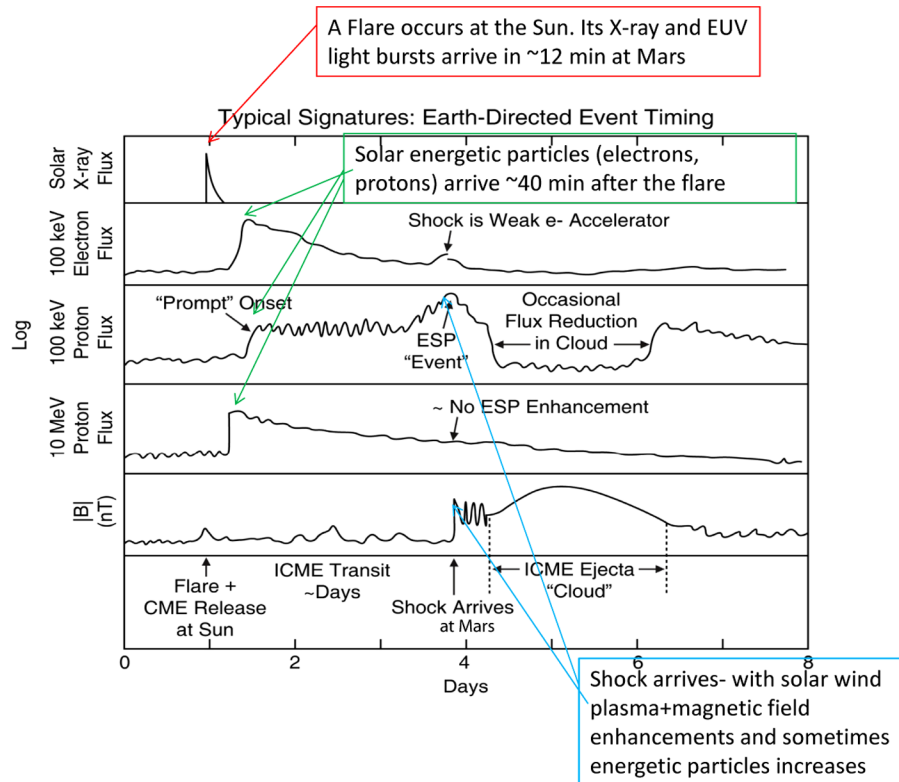


**Fig. 23** Schematic timeline of the effects at Mars of a solar flare and coronal mass ejection event. The panels from top to bottom are: solar x-ray flux, 100 keV electron flux, 100 keV proton flux, 10 MeV proton flux and magnetic field magnitude

storm is an open question at this time. MAVEN studies need to separate the responses to the various influences associated with the flares and CMEs, which often occur together in major events. To this end the timing of the different ICME and SEP event effects, shown in Fig. 23 for a full head-on impact, are important. In particular the flare is relatively brief and usually occurs first, followed by SEPs that arrive before the ICME—although often continue through its passage. This should allow distinction of the flare (only) and SEP (only) responses of the Mars atmosphere. The ICME effect onset should be the last. If SEPs are found to significantly add to the escape rates, their influence can be folded into the historical reconstruction as part of the increased ICME rate-related enhancements.

#### 6.1.4 History of Planetary Obliquity

As mentioned in Sect. 3.2.1, Mars' obliquity is important because it determines the range of angles between the solar wind velocity vector and the strongest crustal fields in the southern hemisphere. In simulations of solar system orbital and rotational dynamics, Mars' obliquity is strongly chaotic and solutions are not possible for its evolution over more than a few million years. However, statistical studies by Laskar et al. (2004) have shown that, though it likely ranged from  $0^\circ$  to  $82^\circ$  over the last 4 Gyr, the average obliquity has been  $38^\circ$  with a standard deviation of  $14^\circ$ , substantially more than the current  $25.2^\circ$ . Global simulations

will be performed over a range of relevant obliquity angles to ascertain its importance for atmospheric escape.

### 6.1.5 History of the Martian Global Magnetic Field

The presence or absence of a global, dynamo-driven planetary magnetic field is a major factor in the solar wind's interaction with a planet's upper atmosphere and therefore the character and magnitude of escape to space. With a global field, most of the atmosphere is shielded from direct interaction with solar wind plasma (the magnetic poles being the exception). Photochemical escape, driven by EUV and in the form of neutral atoms, is largely unaffected by a global field. However, bulk plasma escape, sputtering escape, pickup ion escape and escape driven by lower energy solar energetic particles should be greatly retarded because ion trajectories in near-planet space are dominated by the dipole field. On the other hand, ion outflow in the form of polar wind and auroral processes are likely to be stronger due to the concentrating effects of the polar cusp region (Chassefière and Leblanc 2004). The combined result of these effects have not been thoroughly studied for Mars; though it is generally assumed that loss rates were higher without a dynamo present (Chassefière et al. 2007), other work suggests that a weak dipolar field ( $\sim 10$  nT at the surface) may cause maximal atmospheric loss (Kallio and Barabash 2012; Kallio et al. 2008). In any case, it is clear that the history of the Mars dynamo is inextricably linked to the history of atmospheric loss.

The time during which the Martian dynamo was active was also characterized by extensive volcanism (McEwen et al. 1999), outgassing from which would have continually fed the atmosphere, as well as impacts by large asteroids which contributed to atmospheric erosion (Brain and Jakosky 1998; Melosh and Vickery 1989). Therefore, it is important to determine when the Mars dynamo cessation occurred. Estimates range from model ages of  $\sim 3.7$ – $3.8$  Ga (Milbury et al. 2012) to  $\sim 300$  Myr earlier (Lillis et al. 2008a, 2008b, 2013; Robbins et al. 2013).

## 6.2 Path 1: Extrapolation of Escape Rates

If we measure atmospheric escape rates today over a sufficiently broad range of solar input conditions (EUV flux, solar wind pressure, IMF strength and SEP flux), we can use the results to extrapolate directly to the more active solar conditions prevalent in early Martian history. The variability of these properties through time is known based on telescopic observations of solar-type stars. If we observe sufficiently large excursions from average behavior, and the upper-atmospheric response to them, we can use this to inform extrapolations to early conditions. This path is shown by the path across the top of Fig. 22. It involves a multidimensional extrapolation to reach a 'present-day + extreme conditions' parameterization of global escape rates as a function of solar drivers, which then must be convolved with a range of estimates of the history of those drivers. This extrapolation, while straightforward and achievable, will gloss over significant issues such as the varying obliquity and atmospheric thickness and composition over time. In addition, the extrapolation will be mathematical, not physics-based and will therefore not adequately capture nonlinear effects or couplings between the drivers. However, this approach will still allow a first-order estimate of loss rates under different conditions.

### 6.3 Path 2: Extrapolation of Escape Processes Iteratively Backward in Time

Although path 1 will provide an answer relatively quickly, a robust estimate of total integrated atmospheric loss will ultimately require a confident understanding of the physical processes responsible for atmospheric escape at the present epoch. Only then can we apply these principles to both the extreme solar conditions and different atmospheric densities and compositions of the past to arrive at a more reliable and physically defensible parameterization of global escape rates as a function of solar drivers that covers present day and early solar system conditions. The middle curved light gray arrow in Fig. 22 summarizes this path.

We start with global escape rates through different channels (i.e. sputtering, Jeans' etc.) in multidimensional bins of solar wind pressure, season, EUV flux, SEP flux etc. This parameter space will progressively fill up with statistically more significant values as more data is collected, but gaps or areas of poor sampling are inevitable. We will compare these escape rates to those calculated for the same conditions from our ever-expanding global model library (see Sect. 4.4) and calculate a multidimensional data-to-model 'scale function', i.e. a function of dimensionless numbers which are greater (less) than unity for points in the parameter space where the model under(over)-estimates the escape rates. In other words, at locations where data-derived escape rates exist, the modeled rate multiplied by the scale function gives the data-derived rate. There will be a separate scale function for each of the escape processes and a separate scale function for each of the 2 model frameworks mentioned in Sect. 4. As the models are improved over time, the values of the scale function in the regions of parameter space sampled by MAVEN should move towards unity.

The scale function itself can be interpolated to reach regions of parameter space that are not well covered by the data, resulting in a model-informed parameterization of global escape rates appropriate for present day conditions. With this we can directly calculate the integrated loss over the most recent, say, 500 million years, when average quiet-time solar conditions were much as they are today. This lost atmosphere can then be 'added back' as we go back in time and a set of new global models can be run for this thicker atmosphere and for the average solar conditions that persisted between 500 Myr and 1 Gyr ago. This process will then be repeated as we travel further back in time, being updated at each step with atmospheric models of solar conditions appropriate for that stretch of time. The time interval is completely adjustable and we will use an interval that is both computationally feasible in terms of running models yet has enough resolution to adequately represent the process of atmospheric loss over time on Mars. This iterative process is represented by the dashed arrows leading from the middle box marked 'Total Integrated Escape' back to the blue and then red boxes marked 'Add atmosphere back in time' and 'past Mars atmosphere global models' and back into the large red model library box in the center of Fig. 22. This process can also be checked for consistency by making sure that the atmosphere models for the earliest times are consistent with the isotope-derived atmospheric total integrated loss (described next), as represented by the arrow labeled 'consistency check' on the bottom right of Fig. 22.

### 6.4 Path 3: Isotopic Analysis

Rates of removal from the top of the atmosphere depend on atomic or molecular mass, so the removal rates differ for the different isotopes of the light stable gases. Escape to space preferentially removes the lighter isotopes, so that a greater degree of loss results in the remaining gas having a higher ratio between the heavier and the lighter isotopes.

By simultaneously measuring and separating the Lyman alpha hydrogen (121.567 nm) and deuterium (121.533 nm) coronal emissions using an Echelle grating (McClintock et al.

2014), IUVS will measure the D/H ratio in the Mars upper atmosphere. In addition, the NGIMS instrument (Mahaffy et al. 2014) will measure the ratios of  $^{13}\text{C}/^{12}\text{C}$ ,  $^{18}\text{O}/^{16}\text{O}$ ,  $^{15}\text{N}/^{14}\text{N}$ ,  $^{22}\text{Ne}/^{20}\text{Ne}$ ,  $^{38}\text{Ar}/^{36}\text{Ar}$  and  $^{40}\text{Ar}/^{36}\text{Ar}$  in the atmosphere. By measuring these ratios at the top of the well-mixed lower atmosphere, the top of the thermosphere and by comparing these values with analogous measurements on the Martian surface by the SAM instrument (Mahaffy et al. 2012), we can use straightforward models of isotope fractionation in Jeans', sputtering and photochemical escape (e.g. Fox and Hać 2010) to derive a robust relationship between the measured isotope ratio and the fraction of that gas that has been lost to space over time. As most of these atoms come from the climate-related gases, and the argon isotopes are an excellent indicator of loss by physical (i.e., not chemical or photochemical) processes, we can derive the net loss of each species to space over solar system history. More detail can be found in the MAVEN mission overview paper (Jakosky et al. 2015, [this issue](#)) and references therein. As mentioned above, this net loss can also be used as a consistency check on the latter stages of the iterative process in Path 2.

## 7 Conclusion

In this paper we have laid out our strategy for achieving science closure for the MAVEN mission, i.e. achievable paths from MAVEN measurements to defensible answers to our top-level science goals. It is said that no battle plan survives first contact with the enemy. It is similarly true that our strategy will have to be adjusted as telemetry comes down from Mars and we begin to understand the nuances and limitations of the instruments and their datasets. In addition, many details of our strategy are necessarily still to be determined as model development efforts continue and as we wait to see how the data and models compare and interact (i.e. using data as model input).

The carefully chosen, rigorously tested and tightly focused suite of MAVEN instruments will result in an unprecedented breadth and volume of data concerning the aeronomy and plasma physics of Mars and its interaction with the solar wind. Along with a group of models simulating all aspects of this system in varying degrees of detail and the scientific acumen of a world-class team of coinvestigators and the wider planetary aeronomy and space physics community, we anticipate that MAVEN will fully fulfill its mandate. That is, it will enable the emergence of a clearer picture of the structure and dynamics of the Mars upper atmosphere, a much better understanding of atmospheric escape rates and how they vary with solar and planetary drivers, and ultimately a definitive determination of the total integrated loss of atmosphere to space over Martian history and hence the role this loss has played in the history of Martian climate and habitability.

## References

- E. Alge, N.G. Adams, D. Smith, Measurements of the dissociative recombination coefficients of  $\text{O}^{+2}$ ,  $\text{No}^{+}$  and  $\text{Nh}^{+4}$  in the temperature-range 200–600 K. *J. Phys. B, At. Mol. Opt. Phys.* **16**, 1433–1444 (1983)
- D.E. Anderson, Mariner 6, 7, and 9 ultraviolet spectrometer experiment—analysis of hydrogen Lyman-Alpha data. *J. Geophys. Res.* **79**, 1513–1518 (1974)
- L. Andersson, R.E. Ergun, A.I.F. Stewart, The combined atmospheric photochemistry and ion tracing code: reproducing the Viking Lander results and initial outflow results. *Icarus* **206**, 120–129 (2010)
- L. Andersson, R.E. Ergun, G. Delory, The Langmuir probe and waves experiment for MAVEN. *Space Sci. Rev.* (2014, submitted)
- M. Angelats i Coll, The first Mars thermospheric general circulation model: the Martian atmosphere from the ground to 240 km. *Geophys. Res. Lett.* **32**, L04201 (2005)

- W. Atwell, P. Saganti, F.A. Cucinotta, C.J. Zeitlin, A space radiation shielding model of the Martian radiation environment experiment (MARIE). *Adv. Space Res.* **33**, 2219–2221 (2004)
- S.L. Baliunas, G.W. Henry, R.A. Donahue, F.C. Fekel, W.H. Soon, Properties of Sun-like stars with planets: rho(1) Cancri, tau Bootis, and nu Andromedae. *Astrophys. J.* **474**, L119–L122 (1997)
- S. Barabash, A. Fedorov, R. Lundin, J.A. Sauvaud, Martian atmospheric erosion rates. *Science* **315**, 501–503 (2007a)
- S. Barabash, R. Lundin, H. Andersson, K. Brinkfeldt, A. Grigoriev, H. Gunell, M. Holmström, M. Yamauchi, K. Asamura, P. Bochsler, P. Wurz, R. Cerulli-Irelli, A. Mura, A. Milillo, M. Maggi, S. Orsini, A.J. Coates, D.R. Linder, D.O. Kataria, C.C. Curtis, K.C. Hsieh, B.R. Sandel, R.A. Frahm, J.R. Sharber, J.D. Winningham, M. Grande, E. Kallio, H. Koskinen, P. Riihelä, W. Schmidt, T. Säles, J.U. Kozyra, N. Krupp, J. Woch, S. Livi, J.G. Luhmann, S. McKenna-Lawlor, E.C. Roelof, D.J. Williams, J.A. Sauvaud, A. Fedorov, J.J. Thocaven, The Analyzer of Space Plasmas and Energetic Atoms (ASPERA-3) for the Mars Express mission. *Space Sci. Rev.* **126**, 113–164 (2007b)
- G.A. Bird, New chemical-reaction model for direct simulation Monte-Carlo studies. *Prog. Astronaut. Aeronaut.* **159**, 185–196 (1994)
- S.W. Bougher, H. Shinagawa, The Mars thermosphere-ionosphere: predictions for the arrival of Planet-B. *Earth Planets Space* **50**, 247–257 (1998)
- S.W. Bougher, R.G. Roble, E.C. Ridley, R.E. Dickinson, The Mars thermosphere. 2. General-circulation with coupled dynamics and composition. *J. Geophys. Res., Solid Earth* **95**, 14811–14827 (1990)
- S. Bougher, G. Keating, R. Zurek, J. Murphy, R. Haberle, J. Hollingsworth, R.T. Clancy, Mars global surveyor aerobraking: atmospheric trends and model interpretation. *Adv. Space Res.* **23**, 1887–1897 (1999)
- S.W. Bougher, S. Engel, D.P. Hinson, J.R. Murphy, MGS radio science electron density profiles: interannual variability and implications for the Martian neutral atmosphere. *J. Geophys. Res., Planets* **109**, E03010 (2004)
- S.W. Bougher, J.M. Bell, J.R. Murphy, M.A. Lopez-Valverde, P.G. Withers, Polar warming in the Mars thermosphere: seasonal variations owing to changing insolation and dust distributions. *Geophys. Res. Lett.* **33**, L02203 (2006)
- S.W. Bougher, P.L. Blelly, M. Combi, J.L. Fox, I. Mueller-Wodarg, A. Ridley, R.G. Roble, Neutral upper atmosphere and ionosphere modeling. *Space Sci. Rev.* **139**, 107–141 (2008)
- S.W. Bougher, T.E. Cravens, J. Grebowsky, J. Luhmann, The aeronomy of Mars: characterization by MAVEN of the upper atmospheric reservoir that regulates volatile escape. *Space Sci. Rev.* (2014). doi:[10.1007/s11214-014-0053-7](https://doi.org/10.1007/s11214-014-0053-7)
- S.W. Bougher, D. Pawlowski, J.M. Bell, S. Nelli, T. McDunn, J.R. Murphy, M. Chizek, A. Ridley, Mars global ionosphere-thermosphere model: solar cycle, seasonal, and diurnal variations of the Mars upper atmosphere. *J. Geophys. Res., Planets* **120**, 311–342 (2015)
- D.A. Brain, Variability of the altitude of the Martian sheath. *Geophys. Res. Lett.* **32**, L18203 (2005)
- D.A. Brain, Mars global surveyor measurements of the Martian solar wind interaction. *Space Sci. Rev.* **126**, 77–112 (2006)
- D.A. Brain, B.M. Jakosky, Atmospheric loss since the onset of the Martian geologic record: combined role of impact erosion and sputtering. *J. Geophys. Res., Planets* **103**, 22689–22694 (1998)
- D.A. Brain, F. Bagenal, M.H. Acuña, J.E.P. Connerney, Martian magnetic morphology: contributions from the solar wind and crust. *J. Geophys. Res.* **108**, 1424 (2003). doi:[10.1029/2002JA009482](https://doi.org/10.1029/2002JA009482)
- D.A. Brain, D.L. Mitchell, J.S. Halekas, The magnetic field draping direction at Mars from April 1999 through August 2004. *Icarus* **182**, 464–473 (2006)
- D. Brain, S. Barabash, A. Boesswetter, S. Bougher, S. Brecht, G. Chanteur, D. Hurley, E. Dubinin, X. Fang, M. Fraenz, J. Halekas, E. Harnett, M. Holmstrom, E. Kallio, H. Lammer, S. Ledvina, M. Liemohn, K. Liu, J. Luhmann, Y. Ma, R. Modolo, A. Nagy, U. Motschmann, H. Nilsson, H. Shinagawa, S. Simon, N. Terada, A comparison of global models for the solar wind interaction with Mars. *Icarus* **206**, 139–151 (2010a)
- D.A. Brain, D. Hurley, M.R. Combi, The solar wind interaction with Mars: recent progress and future directions. *Icarus* **206**, 1–4 (2010b)
- D.A. Brain, S.W. Bougher, S.H. Brecht, G.M. Chanteur, S. Curry, C. Dong, E. Dubinin, F. Duru, X. Fang, A. Fedorov, M. Fraenz, J.S. Halekas, E.M. Harnett, S. Hess, M. Holmstrom, R. Jarvinen, E.J. Kallio, A. Kidder, S.A. Ledvina, M.W. Liemohn, J.G. Luhmann, Y. Ma, R. Modolo, A.F. Nagy, D. Najib, H. Nilsson, C.S. Paty, D. Ulusen, Comparison of global models for the escape of Martian atmospheric plasma. Publication: American Geophysical Union, Fall Meeting 2012, abstract #P13C-1969
- D.A. Brain, S. Barabash, S.W. Bougher, F. Duru, B.M. Jakosky, R. Modolo, Solar wind interaction and atmospheric escape, in *Mars Book II* (2015)
- R. Bruno, V. Carbone, The solar wind as a turbulence laboratory. *Living Rev. Sol. Phys.* **10**, 2 (2013)
- M. Chaffin, J.-Y. Chaufray, I. Stewart, M. Montmessin, N. Schneider, Unexpected variability of martian hydrogen escape. *Geophys. Res. Lett.* **41**, 2 (2014). doi:[10.1002/2013GL058578](https://doi.org/10.1002/2013GL058578)

- J.W. Chamberlain, Planetary coronae and atmospheric evaporation. *Planet. Space Sci.* **11**, 901–960 (1963)
- J.W. Chamberlain, Charge-exchange in a planetary corona—its effect on distribution and escape of hydrogen. *J. Geophys. Res. Space Phys.* **82**, 1–9 (1977)
- G.M. Chanteur, E. Dubinin, R. Modolo, M. Fraenz, Capture of solar wind alpha-particles by the Martian atmosphere. *Geophys. Res. Lett.* **36**, L23105 (2009)
- E. Chassefière, F. Leblanc, Mars atmospheric escape and evolution; interaction with the solar wind. *Planet. Space Sci.* **52**, 1039–1058 (2004)
- E. Chassefière, F. Leblanc, B. Langlais, The combined effects of escape and magnetic field histories at Mars. *Planet. Space Sci.* **55**, 343–357 (2007)
- B.K. Chatterjee, R. Johnsen, Clustering reactions of  $\text{H}_2\text{CN}^+$  ions with HCN. *J. Chem. Phys.* **87**, 2399 (1987)
- J.Y. Chaufray, R. Modolo, F. Leblanc, G. Chanteur, R.E. Johnson, J.G. Luhmann, Mars solar wind interaction: formation of the Martian corona and atmospheric loss to space. *J. Geophys. Res.* **112**, E09009 (2007)
- J.Y. Chaufray, J.L. Bertaux, F. Leblanc, E. Quémerais, Observation of the hydrogen corona with SPICAM on Mars express. *Icarus* **195**, 598–613 (2008)
- P.R. Christensen, B. Jakosky, H.H. Kieffer, M.C. Malin, H.Y. McSween, K. Nealon, G.L. Mehall, S.H. Silverman, S. Ferry, M. Caplinger, M. Ravine, The Thermal Emission Imaging System (THEMIS) for the Mars 2001 Odyssey mission. *Space Sci. Rev.* **110**, 85–130 (2004)
- F. Cipriani, F. Leblanc, J.J. Berthelier, Martian corona: nonthermal sources of hot heavy species. *J. Geophys. Res.* **112**, E07001 (2007). doi:[10.1029/2006JE002818](https://doi.org/10.1029/2006JE002818)
- J.T. Clarke, J.-L. Bertaux, J.-Y. Chaufray, G.R. Gladstone, E. Quémérais, J.K. Wilson, D. Bhattacharyya, A rapid decrease of the hydrogen corona of Mars. *Geophys. Res. Lett.* **41**, 8013–8020 (2014). doi:[10.1002/2014GL061803](https://doi.org/10.1002/2014GL061803)
- P.A. Cloutier, C.C. Law, D.H. Crider, P.W. Walker, Y. Chen, M.H. Acuna, J.E.P. Connerney, R.P. Lin, K.A. Anderson, D.L. Mitchell, C.W. Carlson, J. McFadden, D.A. Brain, H. Rème, C. Mazelle, J.A. Sauvaud, C. d’Uston, D. Vignes, S.J. Bauer, N.F. Ness, Venus-like interaction of the solar wind with Mars. *Geophys. Res. Lett.* **26**, 2685–2688 (1999)
- J.E.P. Connerney, M.H. Acuña, P.J. Wasilewski, N.F. Ness, H. Rème, C. Mazelle, D. Vignes, R.P. Lin, D.L. Mitchell, P.A. Cloutier, Response to “Questions about Magnetic Lineations in the Ancient Crust of Mars” (2000) by C.G.A. Harrison. *Science* **287**, 547a (2000)
- J. Connerney, J. Espley, P. Lawton, S. Murphy, J. Odom, R. Oliverson, D. Shepperd, The MAVEN magnetic field investigation. *Space Sci. Rev.* (2015). doi:[10.1007/s11214-015-0169-4](https://doi.org/10.1007/s11214-015-0169-4)
- D.H. Crider, D. Vignes, A.M. Krymskii, T.K. Breus, N.F. Ness, D.L. Mitchell, J.A. Slavin, M. Acuña, A proxy for determining solar wind dynamic pressure at Mars using Mars Global Surveyor data. *J. Geophys. Res.* **108**(A12), 1461 (2003). doi:[10.1029/2003JA009875](https://doi.org/10.1029/2003JA009875)
- S. Curry, M.W. Liemohn, X. Fang, Y. Ma, D. Najib, D. Brain, Model comparison of oxygen ion loss at Mars. Publication: American Geophysical Union, Fall Meeting 2011, abstract #SA13A-1872
- S.M. Curry, M. Liemohn, X. Fang, D. Brain, Y. Ma, Simulated kinetic effects of the corona and solar cycle on high altitude ion transport at Mars. *J. Geophys. Res. Space Phys.* **118**, 3700–3711 (2013a)
- S.M. Curry, M. Liemohn, X. Fang, Y. Ma, J. Espley, The influence of production mechanisms on pick-up ion loss at Mars. *J. Geophys. Res. Space Phys.* **118**, 554–569 (2013b)
- G.T. Delory, J.G. Luhmann, D. Brain, R.J. Lillis, D.L. Mitchell, R.A. Mewaldt, T.V. Falkenberg, Energetic particles detected by the electron reflectometer instrument on the Mars Global Surveyor, 1999–2006. *Space Weather* **10**, S06003 (2012)
- Y. Deng, A.D. Richmond, A.J. Ridley, H.L. Liu, Assessment of the non-hydrostatic effect on the upper atmosphere using a general circulation model (GCM). *Geophys. Res. Lett.* **35**, L01104 (2008)
- C. Diéval, G. Stenberg, H. Nilsson, S. Barabash, A statistical study of proton precipitation onto the Martian upper atmosphere: Mars Express observations. *J. Geophys. Res. Space Phys.* **118**, 1972–1983 (2013)
- C. Dong, S.W. Bougher, Y. Ma, G. Toth, A. Nagy, D. Najib, Solar wind interaction with Mars upper atmosphere: results from the one-way coupling between the multi-fluid MHD model and the MTGCM model. *Geophys. Res. Lett.* **41**, 2708–2715 (2014). doi:[10.1002/2014GL059515](https://doi.org/10.1002/2014GL059515)
- E. Dubinin, Upper ionosphere of Mars is not axially symmetrical. *Earth Planets Space* **64**, 113–120 (2012)
- E. Dubinin, M. Fraenz, A. Fedorov, R. Lundin, N. Edberg, F. Duru, O. Vaisberg, Ion energization and escape on Mars and Venus. *Space Sci. Rev.* **162**, 173–211 (2011)
- E. Dubinin, M. Fraenz, J. Woch, T.L. Zhang, J. Wei, A. Fedorov, S. Barabash, R. Lundin, Bursty escape fluxes in plasma sheets of Mars and Venus. *Geophys. Res. Lett.* **39**, L01104 (2012)
- D.J. Dunlop, J. Arkani-Hamed, Magnetic minerals in the Martian crust. *J. Geophys. Res.* **110**, E12S04 (2005). doi:[10.1029/2005JE002404](https://doi.org/10.1029/2005JE002404)
- N.J.T. Edberg, H. Nilsson, A.O. Williams, M. Lester, S.E. Milan, S.W.H. Cowley, M. Fränz, S. Barabash, Y. Futaana, Pumping out the atmosphere of Mars through solar wind pressure pulses. *Geophys. Res. Lett.* **37**, L03107 (2010)

- F. Eparvier, P.C. Chamberlin, T.N. Woods, E.M.B. Thiemann, The solar extreme ultraviolet monitor for MAVEN. *Space Sci. Rev.* (2014)
- J.R. Espley, G.T. Delory, P.A. Cloutier, Initial observations of low-frequency magnetic fluctuations in the Martian ionosphere. *J. Geophys. Res.* **111**, E06S22 (2006)
- X. Fang, M.W. Liemohn, A.F. Nagy, Y. Ma, D.L. De Zeeuw, J.U. Kozyra, T.H. Zurbuchen, Pickup oxygen ion velocity space and spatial distribution around Mars. *J. Geophys. Res.* **113**, A02210 (2008)
- X. Fang, M.W. Liemohn, A.F. Nagy, J.G. Luhmann, Y. Ma, On the effect of the Martian crustal magnetic field on atmospheric erosion. *Icarus* **206**, 130–138 (2010)
- X.H. Fang, S.W. Bougher, R.E. Johnson, J.G. Luhmann, Y.J. Ma, Y.C. Wang, M.W. Liemohn, The importance of pickup oxygen ion precipitation to the Mars upper atmosphere under extreme solar wind conditions. *Geophys. Res. Lett.* **40**, 1922–1927 (2013)
- A. Fedorov, E. Budnik, J.A. Sauvaud, C. Mazelle, S. Barabash, R. Lundin, M. Acuna, M. Holmstrom, A. Grigoriev, M. Yamauchi, H. Andersson, J.J. Thocaven, D. Winningham, R. Frahm, J.R. Sharber, J. Scherrer, A.J. Coates, D.R. Linder, D.O. Kataria, E. Kallio, H. Koskinen, T. Sales, P. Riihela, W. Schmidt, J. Kozyra, J. Luhmann, E. Roelof, D. Williams, S. Livi, C.C. Curtis, K.C. Hsieh, B.R. Sandel, M. Grande, M. Carter, S. McKenna-Lawler, S. Orsini, R. Cerulli-Irelli, M. Maggi, P. Wurz, P. Bochsler, N. Krupp, J. Woch, M. Franz, K. Asamura, C. Dierker, Structure of the Martian wake. *Icarus* **182**, 329–336 (2006)
- P.D. Feldman, A.J. Steffl, J.W. Parker, M.F. A'Hearn, J.L. Bertaux, S.A. Stern, H.A. Weaver, D.C. Slater, M. Versteeg, H.B. Throop, N.J. Cunningham, L.M. Feaga, Rosetta-Alice observations of exospheric hydrogen and oxygen on Mars. *Icarus* **214**, 394–399 (2011)
- F. Forget, F. Hourdin, R. Fournier, C. Hourdin, O. Talagrand, M. Collins, S.R. Lewis, P.L. Read, J.-P. Huot, Improved general circulation models of the Martian atmosphere from the surface to above 80 km. *J. Geophys. Res.* **104**, 24155 (1999)
- J.L. Fox, A. Hać, Spectrum of hot O at the exobases of the terrestrial planets. *J. Geophys. Res.* **1022**, 24005–24012 (1997)
- J.L. Fox, A.B. Hać, Photochemical escape of oxygen from Mars: a comparison of the exobase approximation to a Monte Carlo method. *Icarus* **204**, 527–544 (2009)
- J.L. Fox, A. Hać, Isotope fractionation in the photochemical escape of O from Mars. *Icarus* **208**, 176–191 (2010)
- J.L. Fox, A.B. Hać, The escape of O from Mars: Sensitivity to the elastic cross sections. *Icarus* **228**, 375–385 (2014)
- Y. Futaana, S. Barabash, M. Yamauchi, S. McKenna-Lawlor, R. Lundin, J.G. Luhmann, D. Brain, E. Carlsson, J.A. Sauvaud, J.D. Winningham, R.A. Frahm, P. Wurz, M. Holmström, H. Gunell, E. Kallio, W. Baumjohann, H. Lammer, J.R. Sharber, K.C. Hsieh, H. Andersson, A. Grigoriev, K. Brinkfeldt, H. Nilsson, K. Asamura, T.L. Zhang, A.J. Coates, D.R. Linder, D.O. Kataria, C.C. Curtis, B.R. Sandel, A. Fedorov, C. Mazelle, J.J. Thocaven, M. Grande, H.E.J. Koskinen, T. Sales, W. Schmidt, P. Riihela, J. Kozyra, N. Krupp, J. Woch, M. Fränz, E. Dubinin, S. Orsini, R. Cerulli-Irelli, A. Mura, A. Milillo, M. Maggi, E. Roelof, P. Brandt, K. Szego, J. Scherrer, P. Bochsler, Mars express and Venus Express multi-point observations of geoeffective solar flare events in December 2006. *Planet. Space Sci.* **56**, 873–880 (2008)
- F. González-Galindo, F. Forget, M.A. López-Valverde, M. Angelats i Coll, E. Millour, A ground-to-exosphere Martian general circulation model: 1. Seasonal, diurnal, and solar cycle variation of thermospheric temperatures. *J. Geophys. Res.* **114**, E04001 (2009)
- F. González-Galindo, J.Y. Chaufray, M.A. Lopez-Valverde, G. Gilli, F. Forget, F. Leblanc, R. Modolo, S. Hess, M. Yagi, Three-dimensional Martian ionosphere model: I. The photochemical ionosphere below 180 km. *J. Geophys. Res., Planets* **118**, 2105–2123 (2013)
- J.T. Gosling, S.J. Bame, W.C. Feldman, D.J. McComas, J.L. Phillips, B. Goldstein, M. Neugebauer, J. Burkepile, A.J. Hundhausen, L. Acton, The band of solar-wind variability at low heliographic latitudes near solar-activity minimum—plasma results from the Ulysses rapid latitude scan. *Geophys. Res. Lett.* **22**, 3329–3332 (1995)
- M. Gurtner, L. Desorgher, E.O. Fluckiger, M.R. Moser, Advances in Space Research Simulation of the interaction of space radiation with the Martian atmosphere and surface. *Adv. Space Res.* **36**, 2176–2181 (2005)
- J.S. Halekas, E.R. Taylor, G. Dalton, G. Johnson, D.W. Curtis, J.P. McFadden, D.L. Mitchell, R.P. Lin, B.M. Jakosky, The MAVEN solar wind ion analyzer. *Space Sci. Rev.* (2013). doi:[10.1007/s11214-013-0029-z](https://doi.org/10.1007/s11214-013-0029-z)
- W.B. Hanson, S. Sanatani, D. Zuccaro, Retarding potential analyzer measurements from Viking Landers. *Trans. Am. Geophys. Union* **57**, 966 (1976)
- T. Hara, K. Seki, Y. Futaana, M. Yamauchi, M. Yagi, Y. Matsumoto, M. Tokumaru, A. Fedorov, S. Barabash, Heavy-ion flux enhancement in the vicinity of the Martian ionosphere during CIR passage: Mars Express ASPERA-3 observations. *J. Geophys. Res.* **116**, A09222 (2011)

- T. Hara, K. Seki, H. Hasegawa, D.A. Brain, K. Matsunaga, M.H. Saito, D. Shiota, Formation processes of flux ropes downstream from Martian crustal magnetic fields inferred from Grad-Shafranov reconstruction. *J. Geophys. Res. Space Phys.* **119**, 1262–1271 (2014)
- P. Hartogh, A.S. Medvedev, T. Kuroda, R. Saito, G. Villanueva, A.G. Feofilov, A.A. Kutepov, U. Berger, Description and climatology of a new general circulation model of the Martian atmosphere. *J. Geophys. Res.* **110**(E11), E11008 (2005)
- D.M. Hassler, C. Zeitlin, R.F. Wimmer-Schweingruber, S. Böttcher, C. Martin, J. Andrews, E. Böhm, D.E. Brinza, M.A. Bullock, S. Burmeister, B. Ehresmann, M. Epperly, D. Grinspoon, J. Köhler, O. Kortmann, K. Neal, J. Peterson, A. Posner, S. Rafkin, L. Seimetz, K.D. Smith, Y. Tyler, G. Weigle, G. Reitz, F.A. Cucinotta, The Radiation Assessment Detector (RAD) investigation. *Space Sci. Rev.* **170**, 503–558 (2012)
- N.G. Heavens, M.I. Richardson, A. Kleinbohl, D.M. Kass, D.J. McCleese, W. Abdou, J.L. Benson, J.T. Schofield, J.H. Shirley, P.M. Wolkenberg, The vertical distribution of dust in the Martian atmosphere during northern spring and summer: observations by the Mars Climate Sounder and analysis of zonal average vertical dust profiles. *J. Geophys. Res., Planets* **116**, E04003 (2011)
- M. Izakov, O. Krasicki, Effect of nonthermal escape of atoms on Martian atmosphere composition. *Trans. Am. Geophys. Union* **58**, 749 (1977)
- B.M. Jakosky, R.P. Lin, J.M. Grebowsky, J.G. Luhmann, D.F. Mitchell, o. Beutelschies G., The Mars Atmosphere and Volatile Evolution (MAVEN) mission. *Space Sci. Rev.* (2015, this issue). doi:10.1007/s11214-015-0139-x
- R.E. Johnson, Plasma-induced sputtering of an atmosphere. *Space Sci. Rev.* **69**, 215–253 (1994)
- R.E. Johnson, J.G. Luhmann, Sputter contribution to the atmospheric corona on Mars. *J. Geophys. Res.* **103**, 3649–3653 (1998)
- R.E. Johnson, D. Schnellenberger, M.C. Wong, The sputtering of an oxygen thermosphere by energetic  $O^+$ . *J. Geophys. Res., Planets* **105**, 1659–1670 (2000)
- M.A. Kahre, J.R. Murphy, R.M. Haberle, Modeling the Martian dust cycle and surface dust reservoirs with the NASA Ames general circulation model. *J. Geophys. Res.* **111**, E06008 (2006)
- E. Kallio, S. Barabash, Magnetized Mars: spatial distribution of oxygen ions. *Earth Planets Space* **64**, 149–156 (2012)
- E. Kallio, S. Barabash, P. Janhunen, R. Jarvinen, Magnetized Mars: transformation of Earth-like magnetosphere to Venus-like induced magnetosphere. *Planet. Space Sci.* **56**, 823–827 (2008)
- E. Kallio, J.-Y. Chaufray, R. Modolo, D. Snowden, R. Winglee, Modeling of Venus, Mars, and Titan. *Space Sci. Rev.* **162**, 267–307 (2011)
- V. Kharchenko, A. Dalgarno, B. Zygelman, J.H. Yee, Energy transfer in collisions of oxygen atoms in the terrestrial atmosphere. *J. Geophys. Res.* **105**, 24899 (2000)
- J. Kim, A.F. Nagy, J.L. Fox, T.E. Cravens, Solar cycle variability of hot oxygen atoms at Mars. *J. Geophys. Res.* **103**, 339–342 (1998)
- D. Koutroumpa, R. Modolo, G. Chanteur, J.Y. Chaufray, V. Kharchenko, R. Lallement, Solar wind charge exchange X-ray emission from Mars. *Astron. Astrophys.* **545**, A153 (2012)
- V.A. Krasnopolsky, Mars' upper atmosphere and ionosphere at low, medium, and high solar activities: implications for evolution of water. *J. Geophys. Res.* **107**, 5128 (2002)
- H. Lammer, *Origin and Evolution of Planetary Atmospheres* (Springer, Berlin, 2013)
- D.E. Larson, R.J. Lillis, K. Hatch, M. Robinson, D. Glaser, J. Chen, D.W. Curtis, C. Tiu, R.P. Lin, J.G. Luhmann, B.M. Jakosky, The MAVEN solar energetic particle investigation. *Space Sci. Rev.* (2015, this issue)
- J. Laskar, A.C.M. Correia, M. Gastineau, F. Joutel, B. Levrard, P. Robutel, Long term evolution and chaotic diffusion of the insolation quantities of Mars. *Icarus* **170**, 343–364 (2004)
- F. Leblanc, R.E. Johnson, Sputtering of the Martian atmosphere by solar wind pick-up ions. *Planet. Space Sci.* **49**, 645–656 (2001)
- F. Leblanc, R.E. Johnson, Role of molecular species in pickup ion sputtering of the Martian atmosphere. *J. Geophys. Res.* **107**, 5010 (2002)
- F. Leblanc, J. Luhmann, R.E. Johnson, E. Chassefiere, Some expected impacts of a solar energetic particle event at Mars. *J. Geophys. Res.* **107**, 1058 (2002)
- S.A. Ledvina, Y.J. Ma, E. Kallio, Modeling and simulating flowing plasmas and related phenomena. *Space Sci. Rev.* **139**, 143–189 (2008)
- F. Lefèvre, Three-dimensional modeling of ozone on Mars. *J. Geophys. Res.* **109**, E07004 (2004)
- C.B. Leovy, Control of the homopause level. *Icarus* **50**, 311–321 (1982)
- R.J. Lillis, D.A. Brain, Nightside electron precipitation at Mars: geographic variability and dependence on solar wind conditions. *J. Geophys. Res. Space Phys.* **118**, 3546–3556 (2013)
- R.J. Lillis, H.V. Frey, M. Manga, Rapid decrease in Martian crustal magnetization in the Noachian era: implications for the dynamo and climate of early Mars. *Geophys. Res. Lett.* **35**, L14203 (2008a)

- R.J. Lillis, H.V. Frey, M. Manga, D.L. Mitchell, R.P. Lin, M.H. Acuña, S.W. Bougher, An improved crustal magnetic field map of Mars from electron reflectometry: highland volcano magmatic history and the end of the Martian dynamo. *Icarus* **194**, 575–596 (2008b)
- R.J. Lillis, D.A. Brain, G.T. Delory, D.L. Mitchell, J.G. Luhmann, R.P. Lin, Evidence for superthermal secondary electrons produced by SEP ionization in the Martian atmosphere. *J. Geophys. Res., Planets* **117**, E03004 (2012)
- R.J. Lillis, S. Robbins, M. Manga, J.S. Halekas, H.V. Frey, Time history of the Martian dynamo from crater magnetic field analysis. *J. Geophys. Res., Planets* **118**, 1488–1511 (2013)
- J. Luhmann, L.H. Brace, Near-Mars space. *Rev. Geophys.* **29**, 121–140 (1991)
- J.G. Luhmann, J.U. Kozyra, Dayside pickup oxygen ion precipitation at Venus and Mars spatial distributions energy deposition and consequences. *J. Geophys. Res.* **96**, 5457–5467 (1991)
- J.G. Luhmann, R.E. Johnson, M.H.G. Zhang, Evolutionary impact of sputtering of the Martian atmosphere by O(+) pickup ions. *Geophys. Res. Lett.* **19**(21), 2151–2154 (1992)
- R. Lundin, A. Zakharov, R. Pellinen, S.W. Barabash, H. Borg, E.M. Dubinin, B. Hultqvist, H. Koskinen, I. Liede, N. Pissarenko, Aspera phobos measurements of the ion outflow from the Martian ionosphere. *Geophys. Res. Lett.* **17**, 873–876 (1990)
- R. Lundin, S. Barabash, A. Fedorov, M. Holmström, H. Nilsson, J.A. Sauvaud, M. Yamauchi, Solar forcing and planetary ion escape from Mars. *Geophys. Res. Lett.* **35**, L09203 (2008)
- R. Lundin, S. Barabash, M. Yamauchi, H. Nilsson, D. Brain, On the relation between plasma escape and the Martian crustal magnetic field. *Geophys. Res. Lett.* **38**, L02102 (2011)
- Y. Ma, Three-dimensional, multispecies, high spatial resolution MHD studies of the solar wind interaction with Mars. *J. Geophys. Res.* **109**, A07211 (2004)
- Y.-J. Ma, A.F. Nagy, Ion escape fluxes from Mars. *Geophys. Res. Lett.* **34**, L08201 (2007)
- Y. Ma, A.F. Nagy, K.C. Hansen, D. De Zeeuw, T. Gombosi, K. Powell, Three-dimensional multispecies MHD studies of the solar wind interaction with Mars in the presence of crustal fields. *J. Geophys. Res.* **107**, 1282 (2002)
- Y. Ma, A.F. Nagy, I.V. Sokolov, K.C. Hansen, Three-dimensional, multispecies, high spatial resolution MHD studies of the solar wind interaction with Mars. *J. Geophys. Res.* **109**, A07211 (2004)
- Y. Ma, X.H. Fang, C.T. Russell, A.F. Nagy, G. Toth, J.G. Luhmann, D.A. Brain, C.F. Dong, Effects of crustal field rotation on the solar wind plasma interaction with Mars. *Geophys. Res. Lett.* **41**, 6563–6569 (2014)
- J.B. Madeleine, F. Forget, E. Millour, L. Montabone, M.J. Wolff, Revisiting the radiative impact of dust on Mars using the LMD Global Climate Model. *J. Geophys. Res., Planets* **116**, E11010 (2011)
- P.R. Mahaffy, C.R. Webster, M. Cabane, The sample analysis at Mars investigation and instrument suite. *Space Sci. Rev.* **170**, 401–478 (2012)
- P.R. Mahaffy, M. Benna, T. King, D.N. Harpold, R. Arvey, M. Barciniak, M. Bendt, D. Carrigan, T. Errigo, V. Holmes, C.S. Johnson, J. Kellogg, P. Kimvilakani, M. Lefavor, J. Hengemihle, F. Jaeger, E. Lyness, J. Maurer, A. Melak, F. Noreiga, M. Noriega, K. Patel, B. Prats, E. Raaen, F. Tan, E. Weidner, C. Gundersen, S. Battel, B.P. Block, K. Arnett, R. Miller, C. Cooper, C. Edmonson, J.T. Nolan, The neutral gas and ion mass spectrometer on the Mars atmosphere and volatile evolution mission. *Space Sci. Rev.* (2014). doi:10.1007/s11214-014-0091-1
- P. Makela, N. Gopalswamy, S. Akiyama, H. Xie, S. Yashiro, Energetic storm particle events in coronal mass ejection-driven shocks. *J. Geophys. Res. Space Phys.* **116**, A08101 (2011)
- L. Maltagliati, F. Montmessin, A. Fedorova, O. Korabev, F. Forget, J.L. Bertaux, Evidence of water vapor in excess of saturation in the atmosphere of Mars. *Science* **333**, 1868–1871 (2011)
- D.J. McCleese, J.T. Schofield, F.W. Taylor, S.B. Calcutt, M.C. Foote, D.M. Kass, C.B. Leovy, D.A. Paige, P.L. Read, R.W. Zurek, Mars climate sounder: an investigation of thermal and water vapor structure, dust and condensate distributions in the atmosphere, and energy balance of the polar regions. *J. Geophys. Res., Planets* **112**, E05S06 (2007)
- W. McClintock, N.M. Schneider, G.M. Holsclaw, J. Clarke, A. Hoskins, I. Stewart, F. Montmessin, R. Yelle, The Imaging Ultraviolet Spectrograph (IUVS) for the MAVEN mission. *Space Sci. Rev.* (2014). doi:10.1007/s11214-014-0098-7
- A.S. McEwen, M.C. Malin, M.H. Carr, W.K. Hartmann, Voluminous volcanism on early Mars revealed in Valles Marineris. *Nature* **397**, 584–586 (1999)
- J. McFadden, O. Kortmann, G. Dalton G. J. R. Abiad, D. Curtis, R. Sterling, K. Hatch, P. Berg, C. Tiu, M. Marckwordt, R. Lin, B. Jakosky, The MAVEN Suprathermal and Thermal Ion Composition (STATIC) instrument. *Space Sci. Rev.* (2014, this issue)
- H.J. Melosh, A.M. Vickery, Impact erosion of the primordial atmosphere of Mars. *Nature* **338**, 487–489 (1989)
- C. Milbury, G. Schubert, C.A. Raymond, S.E. Smrekar, B. Langlais, The history of Mars' dynamo as revealed by modeling magnetic anomalies near Tyrrhenus Mons and Syrtis Major. *J. Geophys. Res.* **117**, 10007 (2012)

- D.L. Mitchell, R. Lin, C. Mazelle, H. Reme, P.A. Cloutier, J. Connerney, M.H. Acuna, N. Ness, Probing Mars' crustal magnetic field and ionosphere with the MGS Electron Reflectometer. *J. Geophys. Res.* **106**, 419–427 (2001)
- D.L. Mitchell, C. Mazelle, D.W. Curtis, The MAVEN solar wind electron analyzer. *Space Sci. Rev.* (2014, submitted)
- R. Modolo, G.M. Chanteur, E. Dubinin, A.P. Matthews, Influence of the solar EUV flux on the Martian plasma environment. *Ann. Geophys.* **23**, 433–444 (2005)
- R. Modolo, G.M. Chanteur, E. Dubinin, A.P. Matthews, Simulated solar wind plasma interaction with the Martian exosphere: influence of the solar EUV flux on the bow shock and the magnetic pile-up boundary. *Ann. Geophys.* **24**, 3403–3410 (2006)
- R. Modolo, G.M. Chanteur, E. Dubinin, Dynamic Martian magnetosphere: transient twist induced by a rotation of the IMF. *Geophys. Res. Lett.* **39**, L01106 (2012)
- F. Montmessin, Origin and role of water ice clouds in the Martian water cycle as inferred from a general circulation model. *J. Geophys. Res.* **109**, E10004 (2004)
- D.D. Morgan, D.A. Gurnett, D.L. Kirchner, R.L. Huff, D.A. Brain, W.V. Boynton, M.H. Acuña, J.J. Plaut, G. Picardi, Solar control of radar wave absorption by the Martian ionosphere. *Geophys. Res. Lett.* **33**, L13202 (2006)
- A.F. Nagy, D. Winterhalter, K. Sauer, T.E. Cravens, S. Brecht, C. Mazelle, D. Crider, E. Kallio, A. Zakharov, E. Dubinin, M. Verigin, G. Kotova, W.I. Axford, C. Bertucci, J.G. Trotignon, The plasma environment of Mars. *Space Sci. Rev.* **111**, 33–114 (2004)
- C.M.C. Nairn, R. Grard, A. Skalsky, J.G. Trotignon, Plasma and wave observations in the night sector of Mars. *J. Geophys. Res. Space Phys.* **96**, 11227–11233 (1991)
- D. Najib, A.F. Nagy, G. Tóth, Y. Ma, Three-dimensional, multifluid, high spatial resolution MHD model studies of the solar wind interaction with Mars. *J. Geophys. Res.* **116**, A05204 (2011)
- F. Nemeč, D.D. Morgan, C. Di'eval, D.A. Gurnett, Y. Futaana, Enhanced ionization of the Martian nightside ionosphere during solar energetic particle events. *Geophys. Res. Lett.* **41**(3), 793–798 (2014)
- G. Newkirk, A.J. Hundhausen, V. Pizzo, Solar cycle modulation of galactic cosmic rays: speculation on the role of coronal transients. *J. Geophys. Res.* **86**, 5387 (1981)
- A.O. Nier, M.B. McElroy, Composition and structure of Mars' upper atmosphere: results from the neutral mass spectrometers on Viking 1 and 2. *J. Geophys. Res.* **82**, 4341–4349 (1977)
- H. Nilsson, E. Carlsson, H. Gunell, Y. Futaana, S. Barabash, R. Lundin, A. Fedorov, Y. Soobiah, A. Coates, M. Franz, E. Roussos, Investigation of the influence of magnetic anomalies on ion distributions at Mars. *Space Sci. Rev.* **126**, 355–372 (2006)
- H. Nilsson, E. Carlsson, D.A. Brain, M. Yamauchi, M. Holmström, S. Barabash, R. Lundin, Y. Futaana, Ion escape from Mars as a function of solar wind conditions: a statistical study. *Icarus* **206**, 40–49 (2010)
- H. Nilsson, N.J.T. Edberg, G. Stenbergh, S. Barabash, M. Holmstrom, Y. Futaana, R. Lundin, A. Fedorov, Heavy ion escape from Mars, influence from solar wind conditions and crustal magnetic fields. *Icarus* **215**, 475–484 (2011)
- D.J. Pawlowski, A.J. Ridley, Modeling the thermospheric response to solar flares. *J. Geophys. Res. Space Phys.* **113**, A10309 (2008)
- D.J. Pawlowski, A.J. Ridley, Modeling the ionospheric response to the 28 October 2003 solar flare due to coupling with the thermosphere. *Radio Sci.* **44**, RS0A23 (2009a)
- D.J. Pawlowski, A.J. Ridley, Quantifying the effect of thermospheric parameterization in a global model. *J. Atmos. Sol.-Terr. Phys.* **71**, 2017–2026 (2009b)
- D.J. Pawlowski, S.W. Bougher, A.J. Ridley, J.R. Murphy, Modeling the Martian upper atmosphere using the Mars global ionosphere-thermosphere model. Publication: American Geophysical Union, Fall Meeting 2012, abstract #SA44A-01
- K. Powell, P. Roe, T. Linde, T. Gombosi, D. De Zeeuw, A solution-adaptive upwind scheme for ideal magnetohydrodynamics. *J. Comput. Phys.* **154**, 284–309 (1999)
- R. Ramstad, Y. Futaana, S. Barabash, H. Nilsson, S.M. del Campo, R. Lundin, K. Schwingenschuh, Phobos 2/ASPERA data revisited: planetary ion escape rate from Mars near the 1989 solar maximum. *Geophys. Res. Lett.* **40**, 477–481 (2013)
- E. Richer, G.M. Chanteur, R. Modolo, E. Dubinin, Reflection of solar wind protons on the Martian bow shock: investigations by means of 3-dimensional simulations. *Geophys. Res. Lett.* **39**, 17 (2012)
- A.J. Ridley, Y. Deng, G. Tóth, The global ionosphere–thermosphere model. *J. Atmos. Sol.-Terr. Phys.* **68**, 839–864 (2006)
- S. Robbins, B. Hynek, R. Lillis, W. Bottke, Large impact crater histories of Mars: the effect of different model crater age techniques. *Icarus* **225**, 173–184 (2013)
- R. Schunk, A. Nagy, *Ionospheres* (Cambridge University Press, Cambridge, 2000)
- V. Sheel, S.A. Haider, P. Withers, K. Kozarev, I. Jun, S. Kang, G. Gronoff, C. Simon Wedlund, Numerical simulation of the effects of a solar energetic particle event on the ionosphere of Mars. *J. Geophys. Res.* **117**, A05312 (2012)

- M. Smith, Thermal emission spectrometer observations of Martian planet-encircling dust storm 2001A. *Icarus* **157**, 259–263 (2002)
- M.D. Smith, THEMIS observations of Mars aerosol optical depth from 2002–2008. *Icarus* **202**, 444–452 (2009)
- M.D. Smith, S.W. Bougher, T. Encrenaz, F. Forget, A. Kleinbohl, Thermal structure and composition of the Mars atmosphere, in *Mars Book II* (2014)
- A. Spiga, F. Forget, A new model to simulate the Martian mesoscale and microscale atmospheric circulation: validation and first results. *J. Geophys. Res., Planets* **114**, E02009 (2009)
- V.A. Tennishev, M.R. Combi, DSMC simulation of the cometary coma. *AIP Conf. Proc.* **663**, 696–703 (2003)
- N. Terada, Y.N. Kulikov, H. Lammer, H.I. Lichtenegger, T. Tanaka, H. Shinagawa, T. Zhang, Atmosphere and water loss from early Mars under extreme solar wind and extreme ultraviolet conditions. *Astrobiology* **9**, 55–70 (2009)
- G. Tóth, I.V. Sokolov, T.I. Gombosi, D.R. Chesney, C.R. Clauer, D.L. De Zeeuw, K.C. Hansen, K.J. Kane, W.B. Manchester, R.C. Oehmke, K.G. Powell, A.J. Ridley, I.I. Roussev, Q.F. Stout, O. Volberg, R.A. Wolf, S. Sazykin, A. Chan, B. Yu, J. Kóta, Space Weather Modeling Framework: a new tool for the space science community. *J. Geophys. Res.* **110**, A12226 (2005)
- D. Tyler, J.R. Barnes, R.M. Haberle, Simulation of surface meteorology at the Pathfinder and VL1 sites using a Mars mesoscale model. *J. Geophys. Res.* **107**, 5018 (2002)
- A.J. Tylka, New insights on solar energetic particles from Wind and ACE. *J. Geophys. Res.* **106**, 25333 (2001)
- D. Ulusen, D.A. Brain, J.G. Luhmann, D.L. Mitchell, Investigation of Mars' ionospheric response to solar energetic particle events. *J. Geophys. Res. Space Phys.* **117**, A5 (2012)
- A. Valeille, M.R. Combi, S.W. Bougher, V. Tennishev, A.F. Nagy, Three-dimensional study of Mars upper thermosphere/ionosphere and hot oxygen corona: 2. Solar cycle, seasonal variations, and evolution over history. *J. Geophys. Res., Planets* **114**, 11005 (2009a)
- A. Valeille, V. Tennishev, S.W. Bougher, M.R. Combi, A.F. Nagy, Three-dimensional study of Mars upper thermosphere/ionosphere and hot oxygen corona: 1. General description and results at equinox for solar low conditions. *J. Geophys. Res.* **114**, E12005 (2009b)
- A. Valeille, M.R. Combi, V. Tennishev, S.W. Bougher, A.F. Nagy, A study of suprathermal oxygen atoms in Mars upper thermosphere and exosphere over the range of limiting conditions. *Icarus* **206**, 18–27 (2010)
- M.I. Verigin, K.I. Gringauz, G.A. Kotova, A.P. Remizov, N.M. Shutte, H. Rosenbauer, S. Livi, A. Richter, W. Riedler, K. Schwingenschuh, K. Szegő, I. Apáthy, M. Tátrallyay, The dependence of the Martian magnetopause and bow shock on solar wind ram pressure according to Phobos 2 TAUS ion spectrometer measurements. *J. Geophys. Res.* **98**, 1303 (1993)
- R.M. Walker, Interaction of energetic nuclear particles in space with the Lunar surface. *Annu. Rev. Earth Planet. Sci.* **3**, 99–128 (1975)
- Y.-C. Wang, J.G. Luhmann, F. Leblanc, X. Fang, R.E. Johnson, Y. Ma, W.-H. Ip, L. Li, Modeling of the  $O^+$  pickup ion sputtering efficiency dependence on solar wind conditions for the Martian atmosphere. *J. Geophys. Res.* **119**(1), 93–108 (2014). doi:[10.1002/2013JE004413](https://doi.org/10.1002/2013JE004413)
- D.F. Webb, Understanding CMEs and their source regions. *J. Atmos. Sol.-Terr. Phys.* **62**, 1415–1426 (2000)
- T.N. Woods, Solar irradiance variability during the October 2003 solar storm period. *Geophys. Res. Lett.* **31**, L10802 (2004)
- M. Yagi, F. Leblanc, J.Y. Chaufray, F. Gonzalez-Galindo, S. Hess, R. Modolo, Mars exospheric thermal and non-thermal components: seasonal and local variations. *Icarus* **221**, 682–693 (2012)
- K. Zahnle, J. Walker, The evolution of solar ultraviolet luminosity. *Rev. Geophys.* **20**, 280–292 (1982)